Monthly Scientific-Technical and Production Journal

The Paton WELDING JOURNAL

October
2002
10

English translation of the monthly «Avtomaticheskaya Svarka» journal published in Russian since 1948

Founders: *The National Academy of Sciences of Ukraine, The E.O. Paton Electric Welding Institute of the NAS of Ukraine, International Association «Welding»*
Publisher: *International Association «Welding»*

Editorial and advertising offices:
E.O. Paton Electric Welding Institute,
International Association «Welding»,
11, Bozhenko str., 03680, Kyiv, Ukraine
Tel.: (38044) 227 67 57
Fax: (38044) 268 04 86
E-mail: journal@paton.kiev.ua
http://www.nas.gov.ua/pwj

State Registration Certificate
KV 4790 of 09.01.2001

Subscriptions:
$460, 12 issues per year,
postage and packaging included.
Back issues available

CONTENTS

SCIENTIFIC AND TECHNICAL

INDUSTRIAL

BRIEF INFORMATION

MATHEMATICAL MODELLING OF HEAT PROCESSES IN WELDING FOAM MATERIALS

V.I. MAKHNENKO[1], **E.A. VELIKOIVANENKO**[1], **G.F. ROZYNKA**[1], **N.I. PIVTORAK**[1], **P. SEYFFARTH**[2] and **U. JASNAU**[2]
[1]The E.O. Paton Electric Welding Institute, NASU, Kyiv, Ukraine
[2]Welding and Training Institute, Mecklenburg, Germany

Algorithm of numerical estimation of temperature fields in a welded joint (penetration zone) in butt welding of elements with a foam macrostructure is suggested. This algorithm is based on corresponding modelling of the foam macrostructure using statistical data on pore parameters. It is shown that welding conditions at a high porosity should substantially differ from those for a solid material.

Key words: *mathematical modelling, foam (porous) macrostructure, stochastic characteristics of macrostructure, welding processes, super-light structural materials, permanent joints, molten pool, fusion welding, material porosity, temperature fields*

Dramatic growth of interest is seen currently in super-light structural materials based on foam (porous) macrostructure for engineering applications. This fact demonstratively follows from the contents of book [1], papers [2, 3], etc. Intensive studies of properties of such materials are conducted both by experimental and computation [4] methods.

Joining structural members of such materials is an important task [5, etc.]. Of high interest are permanent joints produced by traditional methods of fusion welding. However, as proved by the available experience, the use of welding for producing sound welded joints involves much difficulties. Special methods employed for formation of a foam structure of the molten metal pool present a problem. In this connection, of special interest are the fusion welding methods which provide minimum melting of the base material. In particular, welded joints of a sufficient quality can be provided by the methods of beam welding which involve a continuous melted interlayer (Figure 1). However, the choice of rational energy parameters of welding and interlayer thickness b to ensure a minimum penetration of the base material requires detailed studies. Methods of mathematical modelling based on description of the process of heating a specific joint with a welding heat source, allowing for peculiarities of macrostructure of a material, may be helpful in this case. Macrostructure has a considerable effect on heat transfer, as voids (pores) serve as a substantial barrier for the heat, compared with the metal base.

Macrostructure of a foam (porous) material is usually described using the statistical pore size distribution law. To illustrate, Figure 2 shows macrosections of a foam aluminium [2], and Figure 3 shows statistical data on density (frequency) of distribution $P(S)$ of size S of individual cells (pores). As seen from Figure 2, some pores have a very irregular shape, and their characteristic size S can vary in a random manner over wide ranges. If the statistical pore size distribution law is known, i.e. $P(S)$, like in Figure 3, and the mean density of a porous material is designated as γ, then, by assigning a certain shape of an elementary cell, it is possible to calculate mean wall thickness δ of such cells.

For example, if we assume that the elementary cell has a shape of cube with side S, then δ can be determined from the following equation:

$$\gamma = \gamma_0 \frac{\sum_{i}^{N} [S_i^3 - (S_i - \delta)^3] P(S_i)}{\sum_{i}^{N} S_i^3 P_i}, \qquad (1)$$

where γ_0 is the base material density and N is the number of cells in a major volume of the material.

The following cubic equation results from simple transformations of (1) to determine δ:

$$\delta^3 - A\delta^2 + B\delta = F, \qquad (2)$$

where

$$A = \frac{\sum_{i=1}^{N} 3S_i P(S_i)}{\sum_{i=1}^{N} P(S_i)}; \qquad B = \frac{\sum_{i=1}^{N} 3S_i^2 P(S_i)}{\sum_{i=1}^{N} P(S_i)};$$

$$F = \frac{\gamma}{\gamma_0} \frac{\sum_{i=1}^{N} 3S_i^3 P(S_i)}{\sum_{i=1}^{N} P(S_i)}. \qquad (3)$$

Accordingly, the sufficiently large sampling of N the sum of $\sum_{i=1}^{N} P(S_i) = 1$ yields

$$A = 3\bar{S}_i; \quad B = 3 < \bar{S}_i^2 > ; \quad F = \frac{\gamma}{\gamma_0} < \bar{S}_i^3 > , \qquad (4)$$

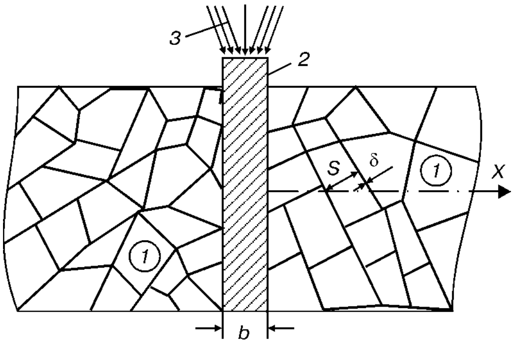

Figure 1. Schematic of fusion butt welding of a porous material through a continuous melted interlayer: *1* — base material; *2* — interlayer; *3* — heat flow

where $\bar{S}_i$ is the mathematical expectation of a random quantity of S_i, and $<\overline{S_i^2}>$ and $<\overline{S_i^3}>$ are, respectively, the mathematical expectations of random quantities of S_i^2 and S_i^3.

Figure 4 shows results of calculation of the δ values for two variants of size distribution $P(S_i)$ for the elementary cells according to Figure 3, depending upon the integrity coefficient (accordingly, the porosity coefficient is $1 - \gamma/\gamma_0$). It is seen from Figure 4 that the δ values increase monotonously from zero (at $\gamma/\gamma_0 = 0$) to some limiting value $\delta_l(P) \approx \bar{S}_i$ (at $\gamma/\gamma_0 \to$ $\to 1$). In particular, for the variant of Figure 3, *a*, in a case of $\delta = 0.1$ mm and $\gamma/\gamma_0 = 0.065$, $\bar{S}_i = 3.33$ mm.

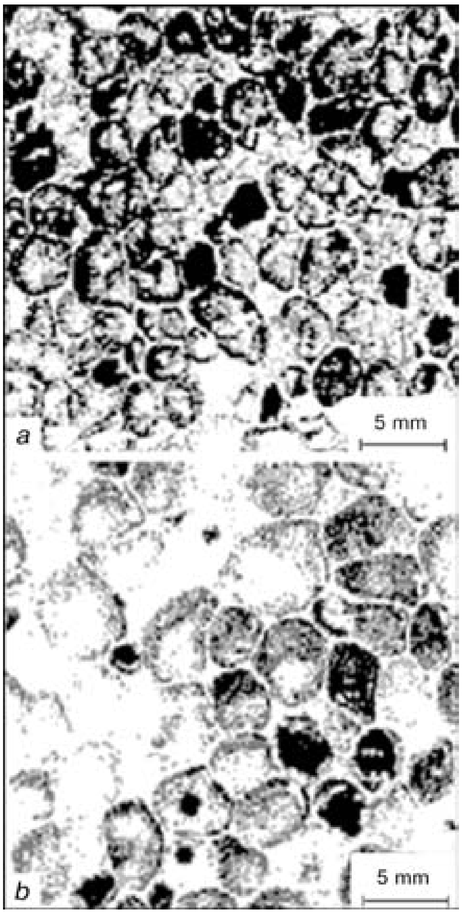

Figure 2. Macrosections of two materials of foam aluminium with fine (*a*) and coarser (*b*) pores [2]

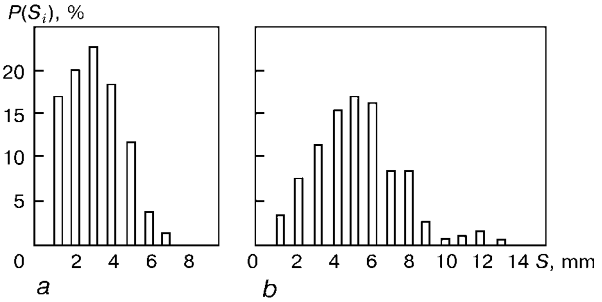

Figure 3. Statistical data on relative density of size distribution of individual cells, $P(S_i)$, for materials with structures shown in Figure 2, respectively

For the same variant, at $\delta = 0.5$ mm and $\gamma/\gamma_0 = 0.30$, $\bar{S}_i$ does not change its value.

The above modelling of a macrostructure of the foam material can be regarded as the simplest and rather rough approximation. There are other, more sophisticated variants of schematisation of geometry of the elementary cells and thickness of the interlayers [4], which provide a more exact description of the reality. However, in this case characteristic parameters of a macrostructure greatly increase in number, as well as labour consumed for numerical description and sophistication of reproduction of the process allowing for a stochastic character of the macrostructure grow.

It should be noted that representation of the process of heating of the foam macrostructure during welding at assigned characteristics of its stochastic description requires that special approaches be employed. The use of the diagram of a high-power fast-moving heat source [6] makes it possible to independently consider individual cross sections of a material welded, having a corresponding random morphology of the foam macrostructure. Numerical solution of the problem of estimation of the penetration zone for each of such sections under specific welding conditions presents an individual random result for a given material. In the case of a sufficiently large sampling of the results, it is possible to derive statistical characteristics of the penetration zone of a given material under given welding conditions. It follows from the above-said that obtaining the appropriate set of random foam macrostructures for the material considered, having assigned statistical characteristics deter-

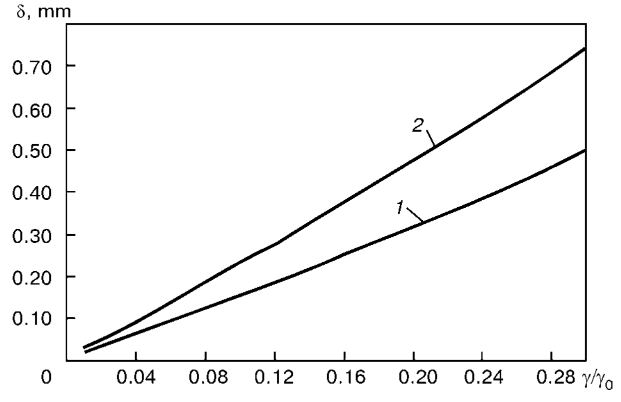

Figure 4. Dependence of mean wall thickness δ upon γ/γ_0 for characteristic $P(S_i)$ obtained from Figure 3, *a* (*1*) and 3, *b* (*2*)

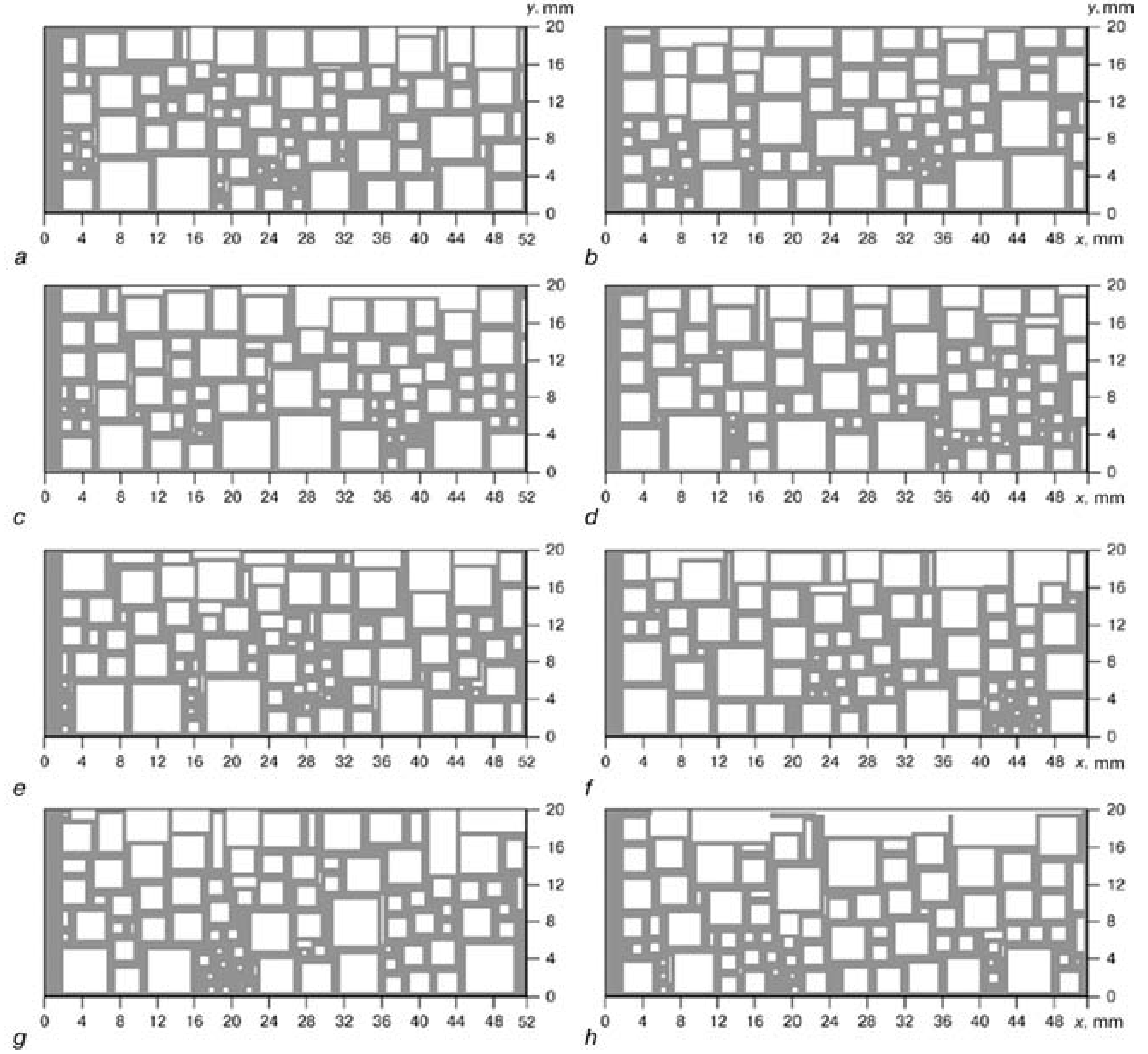

Figure 5. Modelled macrostructures (a–h) of random sections of the material with characteristics $P(S_i)$ from Figure 3, a, at γ/γ_0 = = 0.30, δ = 1 mm and S = 3.33 mm

mined by the size distribution density $P(S_i)$ of the cells at a corresponding idealisation of their shape and a mean value of δ, is a premise of numerical modelling of the problem under consideration. For this purpose the generator of a series of random quantities was used in the study, and this generator was employed to successively select the cells to fill up the region considered at a given value of $P(S_i)$ (Figure 5).

Each random section was estimated by the initial number of the given series. This number was fixed for a repeated representation, but was chosen in a random way. It can be seen from Figure 5 that foam

Table 1. Effect of temperature (°C) on thermal-physical properties of aluminium alloy AMg6 [7] and dry air [8]*

Investigation object	*20*	*100*	*200*	*300*	*400*	*500*	*600*	*700*	*800*	*1000*
Thermal conductivity λ, W/cm·°C										
Air	$2.6\cdot10^{-6}$	$3.49\cdot10^{-6}$	$3.93\cdot10^{-6}$	$4.6\cdot10^{-6}$	$5.21\cdot10^{-6}$	$5.74\cdot10^{-6}$	$6.2\cdot10^{-6}$	$6.71\cdot10^{-6}$	$7.18\cdot10^{-6}$	$8.07\cdot10^{-6}$
AMg6	1.1	1.2	1.4	1.5	1.6	1.8	2.0	–	–	–
Heat capacity per unit volume cγ, J/cm³·°C										
Air	$1.2\cdot10^{-3}$	$0.95\cdot10^{-3}$	$0.76\cdot10^{-3}$	$0.64\cdot10^{-3}$	$0.56\cdot10^{-3}$	$0.5\cdot10^{-3}$	$0.45\cdot10^{-3}$	$0.41\cdot10^{-3}$	$0.38\cdot10^{-3}$	$0.33\cdot10^{-3}$
AMg6	2.5	2.6	2.7	2.8	2.9	2.95	3.0	–	–	–

Notes: 1. For alloy AMg6 (Al-6.2Mg) solidus and liquidus temperatures $T_S \approx 560$ °C and $T_L \approx 640$ °C, respectively. 2. Latent melting heat g_{lat} = = 1050 J/cm³.

macrostructures, having the same values of $P(S_i)$, differ markedly from each other. Naturally, this should affect results of numerical modelling of size and shape of the penetration zone at a corresponding welding heating.

The conventional approach for solving the 2*D* heat problem within the limits of a diagram of a fast-moving heat source for the region with variable properties (Table 1) was employed to generate data on the penetration zone of a specific macrostructure. Sizes of finite elements were selected on the basis of thickness δ of the pore walls.

Heat input q_i of the welding heat source was distributed following the normal law in width and through depth of the solid interlayer of an aluminium alloy. Here it is represented by the following function:

$$g(x,y) = g_0 e^{-K_x x^2 - K_y y^2}, \qquad (5)$$

where $g_0 = \dfrac{\pi q_i}{\sqrt{K_x K_y}}$, and K_x and K_y are the coefficients of concentration of the heat flow along axes x and y, respectively.

As the beam welding methods offer the possibility of regulating the heat flow distribution, it was assumed in the study that

$$K_x = \frac{4a_x}{b^2}; \quad K_y = \frac{4a_y}{H^2}, \qquad (6)$$

where a_x and a_y are the process parameters which, along with q_i, are determined by calculation of size of the penetration zone for the corresponding macrostructures of sections, and H is the desirable depth of penetration of the interlayer.

Figures 5 and 6 give examples of calculations which can be used to demonstrate procedure of the approach described for two-sided butt welding of the 20 mm thick plate of a material with a porous macrostructure, having the $P(S_i)$ characteristic according to Figure 3.

Figure 5 shows macrostructures of the modelled random sections with characteristics $P(S_i)$ from Figure 3, *a*. Temperature fields and size of the penetration zone were calculated proceeding from different values of the process parameters q_i, K_y and K_x. Figure 6 shows results of calculations of distribution of maximum temperatures in random sections (see Figure 5) at $q_i = 21.8$ cal/mm, $K_x = 0.43$ 1/mm^2, $K_y = 0.03$ 1/mm^2, $b = 3$ mm and $H = 5$ mm. These process parameters were determined as a result of numerical experiments and are close to the optimal ones, providing that the penetration zone is such that a porous structure is not destroyed. The penetration zone is determined by maximum temperatures equal to 600–660 °C.

The same approach was used also with other variants of the γ/γ_0 and $\overline{S}_i$ values. The recommended values of q_i are given in Table 2.

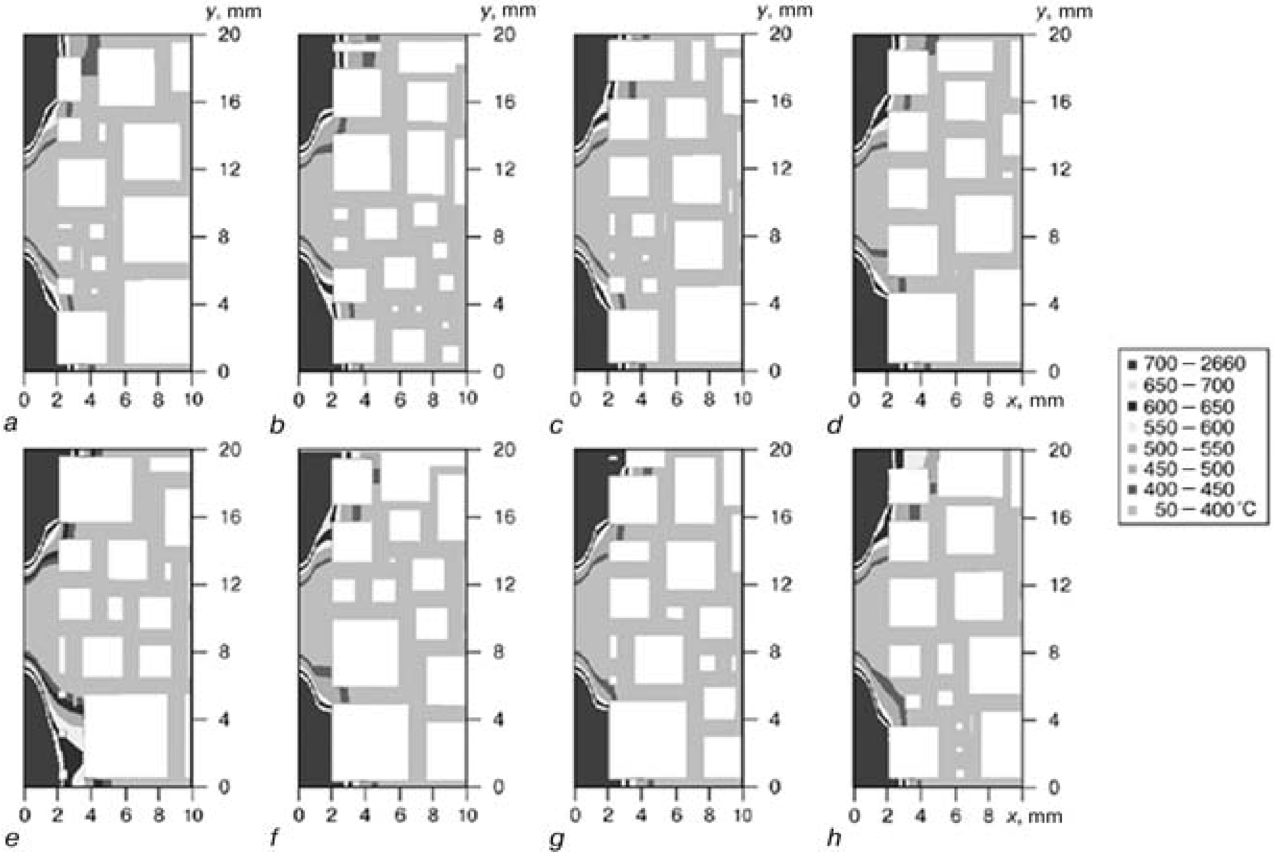

Figure 6. Distribution of maximum temperatures in random sections (*a*–*h*) from Figure 5 in welding the material with $P(S_i)$ according to Figure 3, *a*

Table 2. Recommended heat input for welding aluminium plates with foam macrostructure 20 mm thick using a continuous interlayer (see Figure 1)*

Variant No.	γ/γ_0	$P(S_i)$	$\bar{S}_i$	δ, *mm*	q_i, *cal/mm*
1	0.065	Figure 3, *a*	3.33	0.2	17.46
2	0.085	Figure 3, *b*	4.85	0.4	14.30
3	0.300	Figure 3, *a*	3.33	1.0	21.80
4	0.600	Same	3.33	2.4	40.00

*At $K_x = 0.43$ 1/mm^2, $K_y = 0.03$ 1/mm^2, $b = 3$ mm and $H = 5$ mm.

It was found that lower heat inputs are required to increase porosity, i.e. the $1 - \gamma/\gamma_0$ values, based on a condition of retaining a porous macrostructure of the base material in the joining zone. As follows from Table 2, the lower heat inputs are required also in the case of the same values of γ/γ_0, but higher values of $\bar{S}_i$ (see variants No.1 and 2 in Table 2).

CONCLUSIONS

1. In welding a foam aluminium, the rational welding conditions depend upon the degree of porosity of the material and, to a certain extent, upon the statistical characteristics of sizes of the elementary cells.

2. Numerical methods based on knowledge of stochastic characteristics of a macrostructure of the foam material enable the rational welding conditions to be estimated. However, reliability of this estimation greatly depends upon the adequacy of mathematical description of the said macrostructure.

1. (1999) *Proceedings of Int. MetFoam'99 Conference on Metal Foams and Porous Metal Structures*, Bremen, Germany, June 14–16, 1999.
2. Miyoshi, T., Itoh, M., Akiyama, S. et al. (2000) Alporas aluminium foam: production process, properties and applications. *Advanced Engineering Materials*, **4**, 179–183.
3. Bram, M., Stiller, C., Buchkremer, H.P. et al. (2000) High porosity titanium, stainless steel and supper alloy parts. *Ibid*., 196–199.
4. Raabe, D. (1998) Computational materials science. In: *Simulation of materials microstructures and properties*. Willy-VCH.
5. Olurin, O.B., Fleck, N.A., Ashby, M.F. (2000) Joining of metal foams with fosterer. *Advanced Engineering Materials*, **8**, 521–525.
6. Rykalin, N.N. (1951) *Calculation of thermal processes occurring in welding*. Moscow: Mashgiz.
7. Lifshits, B.G., Kraposhin, V.S., Lipetsky, Ya.L. (1980) *Physical properties of metals and alloys*. Moscow: Metallurgiya.
8. Isachenko, V.P., Osipova, V.A., Sukomel, A.S. (1975) *Heat transfer*. Moscow: Energiya.

AUTOMATIC COMPUTER ANALYSIS OF HOLOGRAPHIC INTERFEROGRAMS IN NON-DESTRUCTIVE QUALITY CONTROL OF MATERIALS AND ELEMENTS OF STRUCTURES

L.M. LOBANOV, V.A. PIVTORAK, V.V. SAVITSKY and **E.M. OLEJNIK**
The E.O. Paton Electric Welding Institute, NASU, Kyiv, Ukraine

A system of computer analysis of holographic interferograms, based on numbering of holographic image of the object examined and use of a method of carrier fringes is presented. Effective method of their producing and a simple algorithm of processing interferograms are suggested. The method of carrier fringes makes it possible to solve the problem of indeterminacy of sign, which is usually available in interference fringe patterns. Examples of application of the developed method for control of defectness of elements of the honey-comb structure and flat samples are given.

Key words: *holographic interferometry, Fourier-transfom, quality control, brazed-welded honey-comb structure*

Creation of new materials and structures is indispensably connected with the improvement and development of methods of their diagnostics. The known methods of quality control (ultrasonic, X-ray, magnetic, etc.) have a number of limitations in testing thin-walled welded structures, and also structures made from composite and polymeric materials. In this connection, the development of new high-efficient and reliable methods of diagnostics of structures made from metallic and non-metallic materials is actual.

Over the recent decade a method of holographic interferometry has been intensively progressed. It is characterized by a high precision and visual representation of information obtained in testing structures. The method is no-contact as it allows information about the deformation of the object examined to be obtained without a special preparation of its surface, etc. [1–3].

The holographic interferometry is one of the most remarkable applications of the holography, in particular in the non-destructive quality control of elements and sub-assemblies of structures [1]. However, its use as a versatile measuring instrument encounters some difficulties, especially in a quantitative analysis of the interference fringe patterns [3]. The problem consists in the fact that the interferograms obtained in practice and characterizing the stress-strain state of the object examined, are rather complicated and their quantitative analysis is time-consuming. In addition, the interferogram does not contain a sufficient amount of information to define a sign of a surface displacement of points of the object examined, i.e. whether the surface was displaced under the action of service loads in the direction to or from the observer. To solve this problem the complex optical interferometers are used which make it possible to realize the multihologram method which is feasible to determine three components of a space vector of displacements [3]. To determine the sign of displacements, special methods for observation of object examined and fulfillment of experiment are used [3, 4]. The rapid progress of computer technologies, software and algorithms of processing of optical information provided the creation of effective methods of analysis of the holographic interferograms.

The present article presents the developed system of the computer analysis of the interferograms on the basis of numbering a holographic image of the object examined and use of the carrier fringe. The method of carrier fringes and its application in interferometry are known [5–9]. We have suggested an effective method of their producing and a simple algorithm for processing interferograms.

The basic its advantage consists in the solution of the problem of sign indeterminacy, usually available in the interference fringe patterns. Moreover, the method of carrier fringes provides the monotony in change of a phase over the object surface and this allows us to use the automatic system for fringe pattern analysis and to increase the sensitivity in determination of displacements by the phase measuring which is determined at a higher sensitivity ($\lambda/20$ as compared with determination of fringe order $\lambda/2$). The created computer system can (if the interferogram of carrier fringes is known) analyze automatically the interference fringes occurring at the surface of the object examined during its deformation and plot a three-dimensional (3D) diagram of displacements of the surface examined.

To optimize the procedures connected with use of the carrier fringes in the computer analysis of the interferograms, the problem was solving about the displacements of surface points of a metal disc under the action of bending loads applied in its center, for which the analytical solution is known. For these purposes, an aluminium disc was manufactured (167 mm diameter, 6 mm thickness) which was rigidly fixed around the contour with a special mechanical device (Figure 1). Using this device a preset load was applied to the center of the fixed disc.

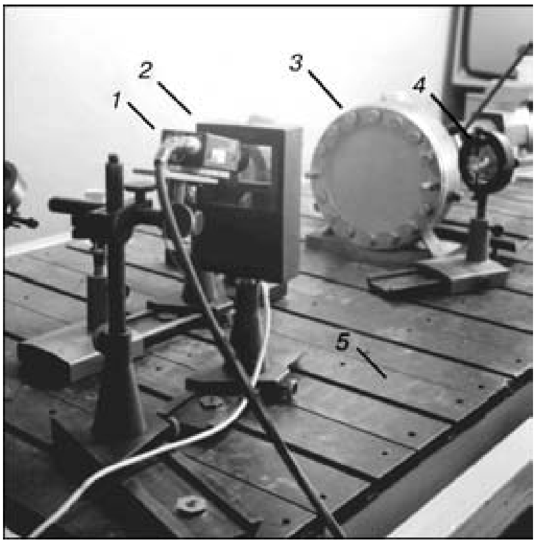

Figure 1. General view of experimental equipment: *1* — CCD-camera; *2* — thermoplastic camera; *3* — sample; *4* — optical element; *5* — vibroisolation table

A dinamometer was mounted on the disc rear side which could control the value of applied load in the disc center. Figure 2 shows an optical scheme of the interferometer which was used in the experiment fulfillment. The photo of the interferogram obtained in a real time during the disc loading with an axial load is shown in Figure 3, *a*. The interference fringes occurring in loading represent concentric circumferences. It should be noted that it is impossible to determine the direction of displacement (distortion) of the surface examined by analyzing only one interference fringe pattern. Disc can be bent outside or inside, but the fringe appearance is not changed. Moreover, using an automatic analysis, it is difficult to interpret the fringe distortion due to the difficulty to program computer so that it can detect in case when fringe of

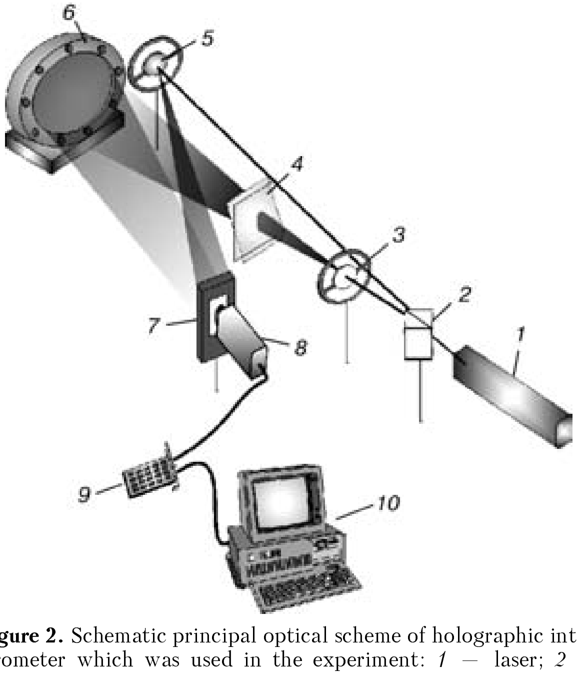

Figure 2. Schematic principal optical scheme of holographic interferometer which was used in the experiment: *1* — laser; *2* — divider; *3* — lens; *4* — phase plate; *5* — dissipating mirror; *6* — sample examined; *7* — recording medium; *8* — CCD-camera; *9* — controller; *10* — computer

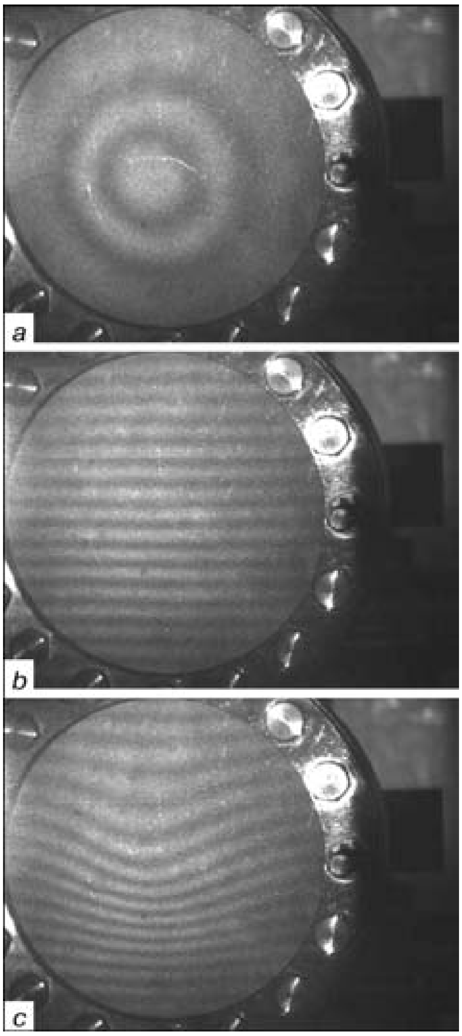

Figure 3. Interferogram obtained in a real time, respectively: *a* — in disc loading with an axial loading; *b* — non-loaded disc with a system of carrier fringes; *c* — total deformation-modulated pattern

the same order is observed in different positions on the disc surface.

One of the methods of the solution of this problem (without the operator's help) is to obtain the initial interferogram of carrier fringes at a high space frequency and to combine it with the interference fringe pattern obtained in loading the object examined. It is known [6] that the distribution of light intensity on the interferogram of carrier fringes is written in the form

$$I_0(x, y) = A_0(x, y) + B_0(x, y) \cos [\varphi_0(x, y)] = = A_0(x, y) + B_0(x, y) \cos [2\pi f_0 y], \quad (1)$$

where x, y are the coordinates of surface of the object examined; $A_0(x, y)$ is the background illumination; $B_0(x, y)$ is the luminosity of fringes; $\varphi_0(x, y)$ is the phase distribution over the surface of the object examined, caused by carrier fringes; f_0 is the frequency of carrier fringes in y-direction.

After loading of the element examined the distribution of intensity on the interferogram (with allowance for modulation with carrier fringes) has a following form:

$$I_m(x, y) = A_m(x, y) + B_m(x, y) \cos [\varphi_m(x, y)] = = A_m(x, y) + B_m(x, y) \cos [\varphi_0(x, y) + \Delta\varphi(x, y)], \quad (2)$$

where $\Delta\varphi(x, y)$ is the distribution of phase over the object surface (caused by its distortion) which is to be determined.

Frequency of carrier fringes (for example, formed by inclination of a phase plate *4* (see Figure 2) which is arranged in the optical scheme of the interferometer in an objective beam) should be several times higher than the maximum frequency of fringes occurring in a deformed disc. Maximum frequency of interference fringes caused by the deformation of the disc examined is determined automatically by a computer using a fast Fourier-transfom. Here, it is necessary to take in account that the maximum frequency of generated carrier fringes is limited by a resolution of the CCD-camera used. Figure 3, *b* shows the appearance of a non-loaded disc with a system of carrier fringes. In this case the fringes were formed by inclination of the phase plate of thickness δ = 2 mm. By varying the angle of inclination it is possible to adjust the space frequency of carrier fringes which cover the surface of the non-loaded disc. The interference fringe pattern can be also created by inclination of the disc examined, change in orientation of a support beam or the hologram itself. As the direction of inclination of the phase plate is known, then the sign of orders of fringes can be adequately established. Figure 3, *c* presents a total fringe pattern when the interferogram of disc was recorded in presence of carrier fringes and fringes caused by a disc loading in its center. Here, none of the interference fringes occurs twice at their calculation along the vertical straight line from the lower part of the disc in the direction to the upper part in any place of the disc. The formation of interference fringes caused by the disc deformation at interaction with carrier fringes only increases or decreases the frequency of carrier fringes (widens or narrows the distance between fringes) that makes it possible to determine easily whether the fringe order was increased or decreased. The presence of CCD-camera in the scheme of the interferometer allows the interference fringe patterns obtained to be numbered and processed using the developed programs, thus providing automatically the 3D image of the disc surface examined.

Experimental data necessary for analyzing the fringe patterns using a method of carrier fringes include the numbered images of the sample examined: a non-loaded disc with an interference pattern of carrier fringes; image of a loaded disc with an interference pattern of carrier fringes modulated with interference patterns of fringes caused by the disc loading; information about direction of inclination of a phase plate in the formation of the pattern of carrier fringes. The sequence of operations in application of the computer analysis of holographic interferograms with use of the carrier fringes consists in the following.

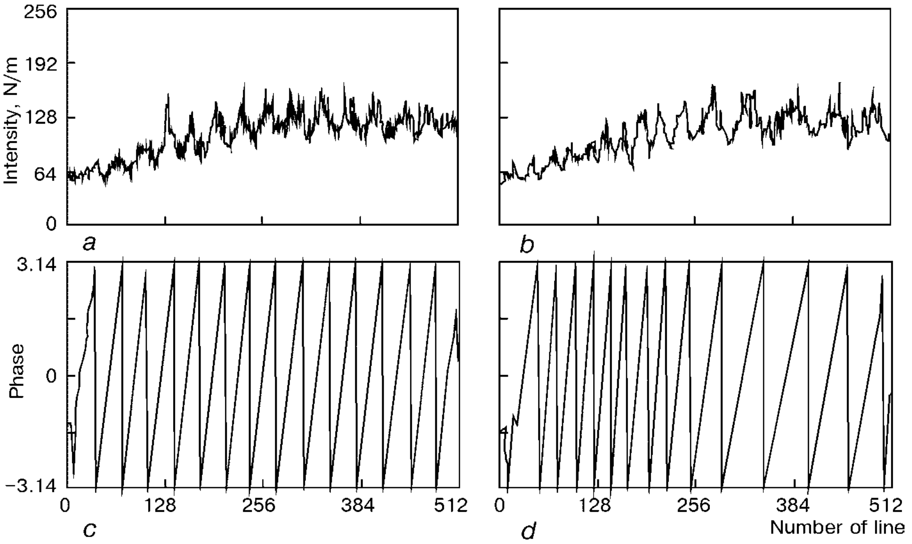

Figure 4. Graphs of dependence of intensity and phase along section (along axis 0*y*) of disc on number of line for interferogram of carrier (*a, c*) and deformation-modulated fringes (*b, d*)

Using the thermoplastic holographic camera, a hologram of the non-loaded disc is recorded. Then, the phase plate is inclined, for example, at angle about 20° as regards to initial position in the direction from an observer. The pattern of parallel carrier fringes covering the surface of the non-loaded disc is observed in a real time. Under the action of the applied force in the disc center, its center is displaced by 0.72 μm in the direction to the observer and one more interference fringe pattern at the disc surface is recorded (see Figure 3, *c*). Taking into account that the direction of the phase plate inclination is known, all the information required for the analysis of the interference pattern and plotting of a 3D image of the deformed surface is consisted in these two photos of the fringe patterns (see Figure 3, *b*, *c*).

To fulfil the automatic computer analysis the images obtained were numbered using CCD-camera in accordance with the above-described method. To demonstrate the procedure of processing the interference fringe patterns a vertical axial section (along axis 0*y*) was selected in a disc.

Diagram of light intensity along this line (section), which is scanned upwards, is shown in Figure 4, *a, b* for each of two images (see Figure 3, *b, c*). Figure 4, *a* shows the change in an initial intensity over the surface of a non-loaded, non-deformed disc with a carrier fringe pattern, and Figure 4, *b* shows the change in initial intensity over the surface of a loaded, deformed disc. In Figure 4, *a* the homogeneous sinusoidal distribution of intensity over the disc surface is mainly observed. In addition to the sinusoidal pattern of carrier fringes a low-frequency constituent of intensity owing to Gaussian nature of a laser illumination is also seen. The result of Fourier-transfom of diagrams of intensities, shown in Figure 4, is given in Figure 5, *b, c*.

The solution of equation (2) with use of a classical Fourier-method encounters often a number of difficulties, as it is necessary to know a precise value of frequency f_0 of the carrier fringes, and also to fulfil the condition providing the similar distance between the carrier fringes that is not always realizable in practice [8]. Therefore, the Fourier-method used in processing of fringes was updated in this article.

Using an integrated representation of a cosine function, the equation (2) is rewritten into the form

$$I_m(x, y) = A_m(x, y) + C_m(x, y) + C^*_m(x, y), \qquad (3)$$

where

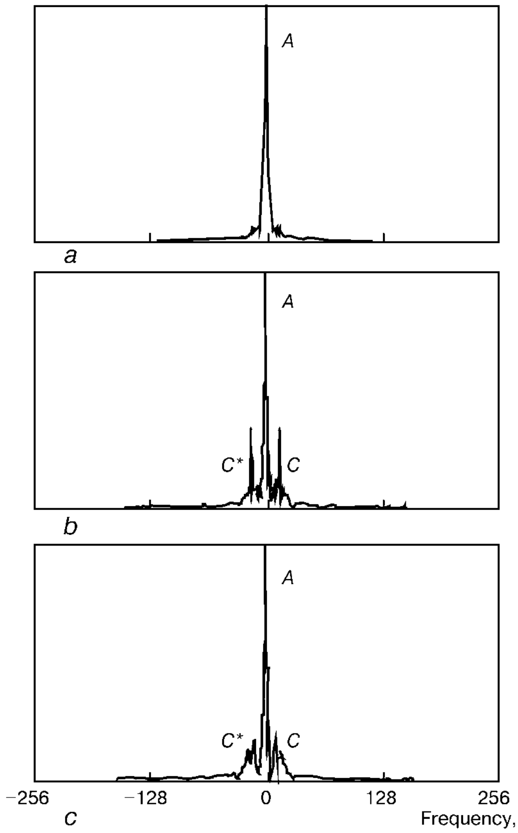

Figure 5. Result of Fourier-transform of diagrams of intensities along the disc ventral section: *a* — in loading disc with axial load; *b* — non-loaded disc with a system of carrier fringes; *c* — loaded disc with a system of carrier fringes

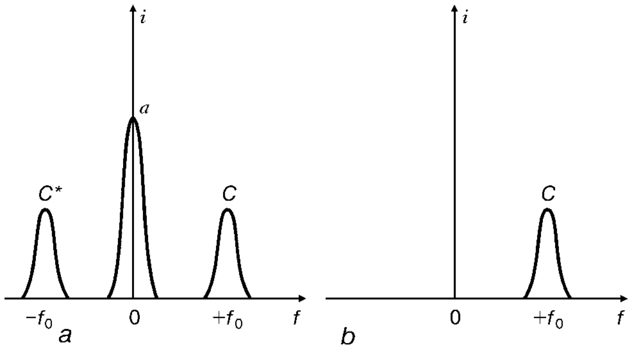

Figure 6. Fourier-spectrum before (*a*) and after (*b*) band-filtering

$$C_m(x, y) = \frac{1}{2}B_m(x, y) \exp\,[j(2\pi f_0 y + \Delta\varphi(x, y))], \tag{4}$$

and $C^*_m(x, y)$ is the integrally mated to $C_m(x, y)$.

Using the Fourier-transfom, relative to y, to equation (3) we shall obtain

$$i_m(x, f) = a_m(x, f) + c_m(x, f) + c^*_m(x, f), \tag{5}$$

where f are the space frequency coordinates.

As $\Delta\varphi(x, y)$, $A_m(x, y)$ and $B_m(x, y)$ are changed slowly as compared with a carrier frequency f_0, the function $i_m(x, f)$ will have three clearly expressed peaks at frequencies $+f_0$, 0, $-f_0$ (Figure 6, *a*). Function $c_m(x, f)$ will be isolated using a filter, aligned around f_0 (Figure 6, *b*). Using the reverse Fourier-transform to $c_m(x, f)$ we shall obtain the function $C_m(x, y)$, determined by equation (4), taking the logarithm of which we shall obtain

$$\log\,[C_m(x, y)] = \\ = \log\left[\frac{1}{2}B_m(x, y)\right] + j[2\pi f_0 y + \Delta\varphi(x, y)]. \tag{6}$$

By separating an integral part from the equation (6) we shall find the distribution of phase $\varphi_m(x, y)$ over the entire surface of the object examined:

$$\varphi_m(x, y) = 2\pi f_0 y = \Delta\varphi(x, y) = \varphi_0(x, y) + \Delta\varphi(x, y). \tag{7}$$

Thus, to find the distribution of phase $\Delta\varphi(x, y)$ it is necessary to know exactly the frequency of carrier fringes f_0 or distribution of $\varphi_0(x, y)$ which can be found from equation (1). By its solution with respect to $\varphi_0(x, y)$ similarly to (3), we shall obtain after Fourier-transform of equation

$$i_0(x, f) = a_0(x, f) + b_0(x, f - f_0) + b^*_0(x, f + f_0). \tag{8}$$

Separating function $b_0(x, f - f_0)$ using a filter, aligned around f_0 a reverse Fourier-tranform was applied to it, then the logarithm was taken, and by separating an integrated part, the unknown addend $\varphi_0(x, y)$ and the phase $\Delta\varphi(x, y)$ distribution corresponding to the interferogram of the object examined were found:

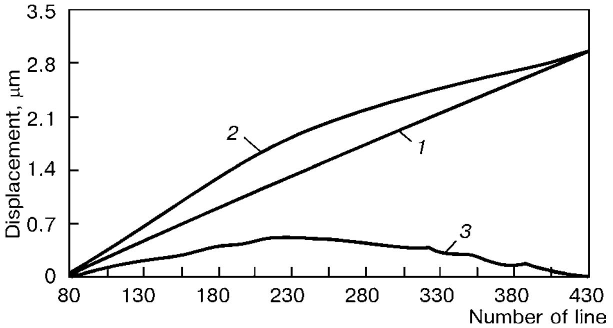

Figure 7. Diagram of dependence of displacements of surface point on number of line along the central line: *1* — displacements corresponding to carrier fringe pattern; *2* — displacements corresponding to deformation-modulated fringes; *3* — real displacements corresponding to the object deformation

$$\Delta\varphi(x, y) = \varphi_m(x, y) - \varphi_0(x, y). \tag{9}$$

The distribution obtained is indeterminated with an accuracy to a multiplier 2π occurring due to periodicity of a cosine function. Using a simple algorithm the program detects automatically the jumps of the phase and finds the unknown multiplier. The quantitative value of vectors of displacement of points of the object surface examined can be found by knowing distribution of phase $\Delta\varphi(x, y)$ and parameters of the optical scheme

$$\Delta\varphi = \frac{2\pi}{\lambda}\Delta\vec{r}\,(\vec{\rho_0} - \vec{\rho}), \tag{10}$$

where $\Delta\vec{r}$ is the vector of displacement of the object points between exposures; $\vec{\rho_0}$ are the orth-normals to the front of illuminating wave in a point; $\vec{\rho}$ are the orth-directions of observation of point; λ is the length of wave of coherent radiation source; $\Delta\varphi$ is the total shear of phases of waves.

The given algorithm does not require parallelism and straight linearity of carrier fringes in the analysis fulfillment. The only condition of its successful use is the assurance of frequency of the carrier fringes, which should be higher than the maximum frequency of interference fringes caused by the deformation of the object examined. This is determined automatically by the computer using a fast Fourier-transform. This requirement is necessary to separate the peaks of intensity in a Fourier-spectrum (see Figure 6, *a*).

The important features of the frequency spectrum for a non-loaded disc (see Figure 5, *b*) is the presence of two sharp peaks C and C^* at the carrier frequency, low-frequency peak A, representing Gaussian distribution of intensity of illumination with a laser beam, and also a high-frequency noise due to speckles and limitations of an optical scheme (electronic noise, etc.). Figure 5, *c*, which gives similar information for a loaded disc (carrier plus deformation fringes), shows that deformation causes the modulation of the initial pattern frequency of carrier fringes, the necessary information here is presented now as peak C of the frequencies spectrum.

Analyzing the spectrum of a non-distorted image (Figure 5, *b*) the computer program sets a narrow transmission band around peak C. All the frequencies located beyond this band are eliminated. Then, the computer program controls the spectrum of a distorted

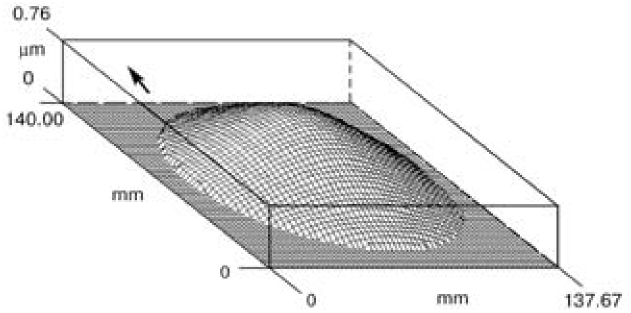

Figure 8. Diagram of a distorted disc surface caused by applied axial force

(carrier + deformation) image (Figure 5, *c*) and cuts the peaks *A* and C^*, and also all the frequencies at which the signal level decreased to the noise level. According to the algorithm and use of the reverse Fourier-transform, a filtered spectrum *C* after taking a logarithm and separation of an integrated part is presented in the form of dependence of a phase on a number of pixel (see Figure 4, *c, d*). Then, the program detects automatically the phase jumps and eliminates them.

Figure 7 presents a diagram of dependence of displacements on a number of line along the a vertical central line both for non-loaded and loaded discs. Curve *1* obtained for the non-loaded disc represents a simple sinusoidal fringe pattern on the disc surface. Curve *2* obtained in the loaded state corresponds to a slow phase transition along the disc lower part where the intensity bands were separated by an interval, and then to a fast phase transition to the disc upper part where the fringes are compressed together. As the curve *1* (see Figure 7) gives the information about distribution of the carrier fringes phase, and curve *2* gives the appropriate information for the deformation-modulation pattern of fringes, the next step consists of subtraction of these two curves. Curve *3* represents a profile of off-plane deformation of the disc surface along the vertical central line made from a lower to an upper part.

The automatic repetition of stages of analysis of interference fringe patterns for each filtered column of section provides a description of the off-plane deformation over the entire disc field. This final result is given in Figure 8 which shows a diagram of the distorted disc surface obtained using a computer graphs.

Experiments on revealing defects in flat metal elements were performed on the basis of the above-mentioned procedure. For this purpose, a round aluminium plate of 167 mm diameter and 6 mm thickness

Parameters of artificial defects induced into aluminium plate

Sample No.	*Defect length, mm*	*Defect width, mm*	*Defect depth, mm*
1	15	0.7	1.5
2	15	1.2	1.5
3	7	0.7	1.7
4	5	0.7	2.0

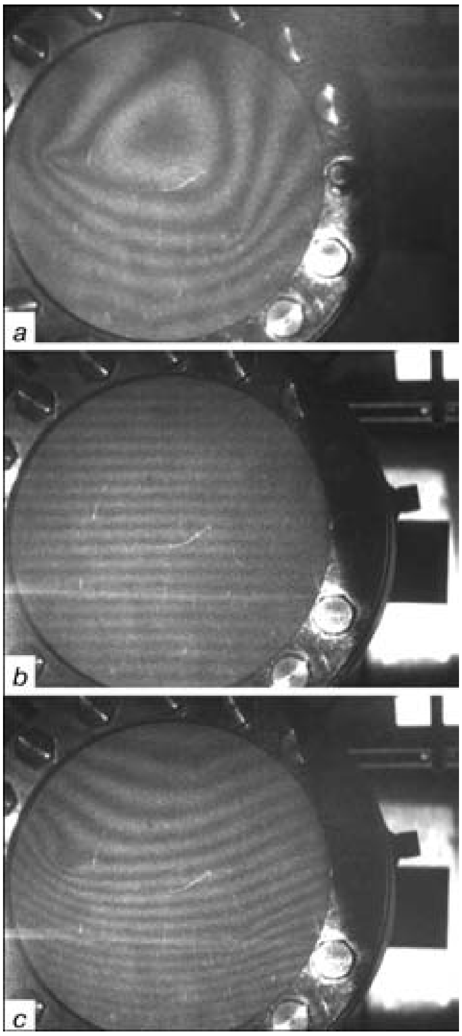

Figure 9. Interferograms of a disc with defects, respectively: *a* — under action of temperature loading; *b* — non-loaded disc with a system of carrier fringes; *c* — total deformation-modulated fringe pattern

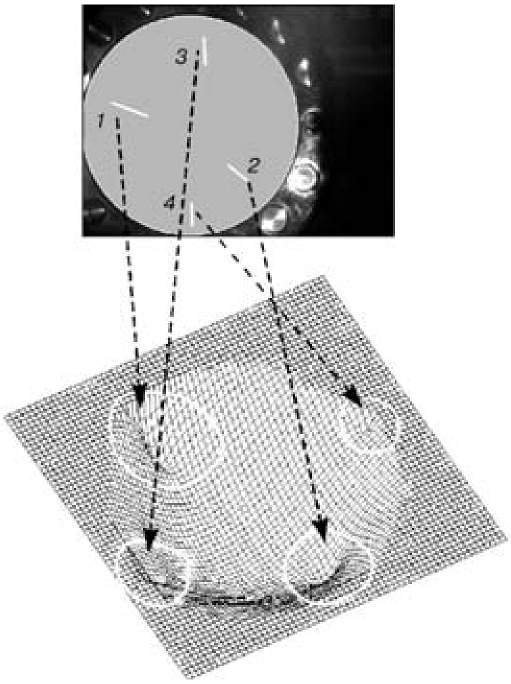

Figure 10. 3D diagram characterizing presence of defects in disc (*1–4* — number of sample, see the Table)

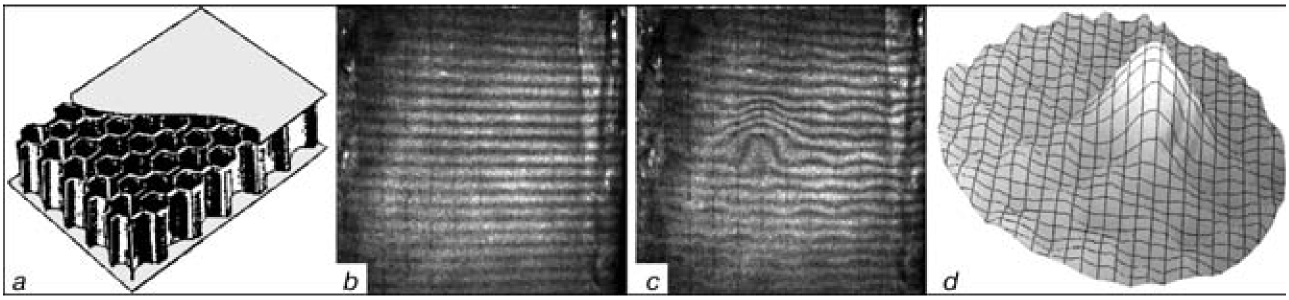

Figure 11. Defectness control in element of honey-comb structure: *a* — sketch of honey-comb panel element; *b* — interferogram of non-loaded element with a system of carrier fringes; *c* — interferogram of a deformed element with a system of carrier fringes; *d* — 3D diagram characterizing the presence of defects in element examined

was used, in which the artificial defects (four slots) of parameters, given in the Table, were made at the reverse side.

The distance between defects was selected so that the neighboring defects did not influence each other. The plate was fixed rigidly around the contour in a mechanical loading device. A thermal blowing of a sample from the distance of about 2 cm at temperature about 50 °C using a special heating device during 30 s was used as loading. Figure 9, *a* shows an interferogram of the distorted disc under the action of the temperature loading. From a local distortion of the fringe patterns only three of four induced defects of the disc are observed visually. Figure 9, *b, c* shows, respectively, the interferogram of carrier fringes and deformation-modulated interferogram. Following the above-described algorithm the interferograms were processed to obtain a 3D diagram (Figure 10), characterizing the displacement of points of disc surface from the plane. Four induced artificial defects are clearly seen. A local concentration of deformations (displacements) characterizing the presence of artificially-induced defects is seen on the background of a uniform deformation caused by loading.

The suggested procedure could also reveal the defectness in an element of a brazed-welded honey-comb structure (Figure 11, *a*) of 150×200×15 mm size, made from stainless steel.

Figure 11, *b* shows a pattern of carrier fringes at the surface of element being examined. The honey-comb element was loaded with an internal pressure using an air. Deformation-modulated interferogram of the sample surface is given in Figure 11, *c*. Local distortion of fringes characterizes the defective region of the honey-comb element (absence of a quality brazing). In Figure 11, *d* a 3D diagram is plotted characterizing the displacement of the surface points under the action of the internal pressure. A defective region caused by a non-quality joining of honey-comb cells with a flat sheet is seen visually on the background of displacements caused by a honey-comb structure of the sample.

CONCLUSION

The improved method of carrier fringes used in analyzing holographic interferograms has been developed, which is used successfully in examination of a center-loaded disc. The creation of carrier fringes made it possible to solve the problem of sign indeterminacy that gives feasibility to perform the automatic processing of the interferograms. The offered mathematical algorithm of the computer processing of the interference patterns on the basis of use of the carrier fringes and Fourier-spectrum analysis can produce the 3D images of surface of the object examined, and determine the regions of concentration of deformations caused by the presence of internal defects.

The computer system developed opens up the new opportunities for the automatic analysis of interference fringe patterns characterizing the quality of objects during their non-destructive examination.

1. Colier, R., Berkhart, C., Lin, L. (1973) *Optical holography*. Moscow: Mir.
2. Rastogi, P.K., Inaudi, D. (2000) *Trends in optical non-destructive testing and inspection*. Oxford: Elsevier Sci.
3. Ostrovsky, Yu.I., Shchepinov, V.P., Yakovlev, V.V. (1988) *Holographic interference methods of measuring of deformations*. Moscow: Nauka.
4. Kasatkin, B.S., Kudrin, A.B., Lobanov, L.M. et al. (1981) *Experimental methods of strain and stress examinations*. Kyiv: Naukova Dumka.
5. Matthys, D.R., Dudderar, T.D., Gilbert, J.A. (1988) Automated analysis of holointerferograms for the determination of surface displacement. *Experimental Mechanics*, **3**, 86–91.
6. Takeda, M., Ina, H., Kobayashi, S. (1982) Fourier-transform method of fringe-pattern analysis for computer-based topography and interferometry. *J. Opt. Soc. Am.*, **72**, 156–160.
7. Kujawinska, M., Osten, W. (1998) Fringe pattern analysis methods: up-to-date review. *Proc. SPIE*, **3407**, 56–66.
8. Kreis, Th., Juptner, W. (1989) Fourier-transform evaluation of interference pattern: the role of filtering in spatial-domain in laser interferometry. Qualitative analysis of interferograms. *Ibid.*, **1162**, 116–125.
9. Huntley, J.M., Coggrave, C.R. (1998) Progress in phase unwrapping. *Ibid.*, **3407**, 86–93.

VACUUM BRAZING OF DISPERSION-STRENGTHENED COPPER ALLOY GLIDCOP AL-25

S.V. MAKSIMOVA, V.F. KHORUNOV, V.A. SHONIN, I.V. ZVOLINSKY, V.V. VORONOV and **V.A. KOSTIN**
The E.O. Paton Electric Welding Institute, NASU, Kyiv, Ukraine

The effect exerted by a composition of brazing filler metals on structure, chemical heterogeneity and mechanical strength of brazed joints in dispersion-strengthened alloy Glidcop Al-25 was investigated. It is shown that along with the composition of a brazing filler metal, the significant role is also played by a pre-brazing heat treatment. Strength of the brazed joints was found to be 380–400 MPa in the case of using a heat-treated base metal and the optimised composition of a brazing filler metal.

Key words: *dispersion-strengthened copper alloy, vacuum brazing, brazing filler metal, brazed joint, microstructure, strength*

Introduction. Dispersion-strengthened copper alloys of the Glidcop Al-25 type are receiving currently much attention [1–4]. They are characterised by high mechanical properties (see, e.g., data on alloy CuAl25 in Table 1), increased thermal stability of structure and good thermal conductivity. Dispersion-strengthened copper alloys are widely applied for the manufacture of electrodes for resistance welding [2], cathodes of plasmatrons, high-power X-ray tubes, power-intensive elements in various power systems, including fusion reactors [5–7], and other items.

Composite material Glidcop Al-25 is a heterogeneous system consisting of a copper matrix with grains 0.5–1.0 μm in size and uniformly distributed thermodynamically stable dispersed particles of the strengthening phase Al_2O_3 (0.5 wt.%), differing from copper in physical and chemical properties. Therefore, in making joints in alloy Glidcop Al-25 by welding, one faces serious, often insoluble problems, associated primarily with coagulation of the strengthening phase. So, the use of brazing shows more promise in this case.

Literature data on investigation of brazed joints in dispersion-strengthened copper are scanty. It is known that vacuum, argon or air brazing of the dispersion-strengthened alloy containing 0.15–0.25 % Al_2O_3 using pure silver or Ag–Cu and Ag–Cu–Ti system filler metals results in embrittlement of the brazed joints, caused by localisation of aluminium particles in the central part of the joint [6, 8]. The authors of [6] suggest using the barrier coatings of copper, nickel or palladium, as well as compression of the mating surfaces [8]. However, these measures failed to provide the joints of a satisfactory strength.

Study [5] considered the possibility of using filler metal BAg-5 of the Ag–Cu–Zn system under the induction heating conditions, which may help to solve only a narrow range of problems.

A positive experience is available in using zirconium as a filler metal for contact-reactive brazing of copper alloy MAGT-0.2 [9]. However, this study unfortunately gives no data on strength of the brazed joints made at room temperature.

It should be noted that selection of brazing filler metals has to be done with allowance for the following factors: these are, firstly, limitations on the brazing temperature (not higher than 1000 °C) to avoid coagulation of the strengthening phase, recrystallisation of matrix and, hence, loss in strength; and, secondly, difficulties arising in wetting the non-metallic component differing from copper in physical and chemical properties with the metal melts.

Large contribution to investigations of the wetting processes, capillary phenomena, adhesion and contact interaction of non-metallic compounds (diamonds, graphites, nitrides, oxides) with the metal melts was made by associates of the Institute for Materials Science Problems of the NAS of Ukraine [10–12]. The efforts headed by Yu.V. Najdich included detailed studies of phenomena occurring at the interface between metal melts and ionic compounds, covalent crystals and materials with metal properties. It was established that elements reactive with respect to a

Table 1. Mechanical properties of alloy CuAl25*

Test temperature, °C	σ_t, *MPa*	$\sigma_{0.2}$, *MPa*	ψ, *%*
20	423	332	69
50	410	326	69
100	386	314	68
150	362	298	66
200	336	279	61
250	308	255	56
300	279	228	48
350	249	197	39
400	218	162	28
450	185	123	16
500	150	80	2

*Averaged values are given.

Table 2. Chemical composition of adhesion-active brazing filler metals

Filler metal No.	*Alloy grade*	*Content of elements, wt.%*				T_s, °C	T_l, °C
		Zr	*Ti*	*Ni*	*Cu*		
1	Stemet 1406	Base	11	14	13	770	857
2	Stemet 1409	Same	11	14	12	685	767
3	Stemet 1201	12	Base	12	23	830	955
4	Stemet 1202	12	Same	12	22	748	857

Note. T_s and T_l are solidus and liquidus temperatures, respectively.

non-metallic component of the base material should be added to the metal melts to increase wettability of non-metallic inclusions, e.g. silicon for wetting SiC, titanium for wetting oxides, carbides and nitrides, and chromium for wetting carbon compounds [10].

The present study considers the possibility of improving mechanical properties of brazed joints in alloy Glidcop Al-25 by using adhesion-active brazing filler metals.

Experimental materials and equipment. Four known brazing filler metals [13] based on the Zr–Ni–Cu–Ti (No.1, 2) and Ti–Cu–Zr–Ni (No.3, 4) systems, the compositions of which are given in Table 2, were selected for the experiments. The brazing filler metals were used in the form of a strip of an amorphous structure with thickness of about 30 μm. It was produced by rapid solidification of the melt on a rotating cooling drum at a rate of approximately $1\cdot10^4$–$1\cdot10^6$ °C/s. The base material was used in the form of rods 16 mm in diameter (in the as-received condition and after annealing at a temperature of 950 °C for 1 h).

Cylindrical samples 75 mm long were made for brazing. They were butt brazed in a vacuum furnace with radiation heating (rarefaction of the working space ranging from 1 to $5\cdot10^{-3}$ MPa) at T_l (in some cases 50 °C higher), then held for 3 min at this temperature and cooled together with the furnace to room temperature.

Specimens 20×15 mm in size were cut for metallographic analysis. Microstructure of the brazed joints was examined using the optical microscope «Neophote», while chemical heterogeneity was studied using the JEOL scanning electron microscope JSM-840 equipped with a system of the «Link-Analytic» and «Optek» microanalysers. The studies were conducted under conditions of the back-scattered electrons (Compo) and secondary electrons (SEI) at an accelerating voltage of 20 kV and current of $1\cdot10^{-10}$–$1\cdot10^{-7}$ A.

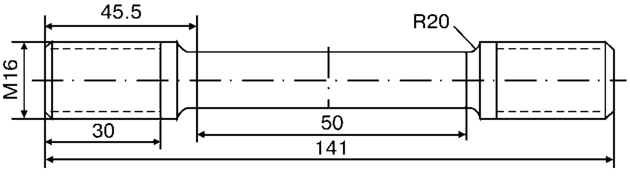

Figure 1. Schematic of a specimen for mechanical tests

Specimens for mechanical tests (Figure 1) were made from the brazed joints. Mechanical tensile tests were conducted using the electromechanical testing machine UM10^{TM} equipped with the required electronic equipment, the strain gauge measuring device with a gauge length of 25 mm and the two-coordinate recording device N307/1. The accuracy of readings in measuring the load was at a level of ± 1 %. During the tests the travel speed of the clamp to a value of proof stress was equal to $8\cdot10^{-3}$ mm/s and with further tension to complete fracture of a specimen it was equal to $8\cdot10^{-2}$ mm/s. The test temperature was 20–24 °C. During the tests the diagrams of straining to a value of residual elongation equal to more than 0.2 % were recorded. Then the load was decreased to zero.

Experimental results and discussion. Brazed joints produced by using filler metal No.1 at T_l (Table 2) were characterised by a poor fillet formation. The brazed joints fractured in manufacture of specimens for metallographic examination, which was probably caused by formation of brittle phases in the seam metal. An increase of 110 °C (to 1000 °C) in the brazing temperature made it possible to produce joints with a good fillet formation on both sides of a sample (the filler metal flew even to the lateral faces), appearance of erosion being detected in the fillet regions.

Results of investigations of chemical composition of metal of the joining zone by scanning electron microscopy showed that metal in the fillet region had a two-phase structure, i.e. eutectic (Figure 2, *a*) containing up to 26 at.% Zr and a Cu-base solid solution containing 0.5 at.% Ti and 0.5 at.% Al (Table 3). In the brazed joint metal the eutectic component was revealed both in the central part of the seam (in the form of a continuous chain) and along the solid solution grain boundaries. Width of the seam was 5–120 μm.

In brazing using filler metal No.2 at temperatures T_l and T_l + 50 °C (see Table 2), the brazed joints, like in the first case, fractured in cutting. Increase in brazing temperature to 1000 °C provided strength sufficient for metallography. High overheating and activity of the filler metal led to erosion of the fillet regions. The seam had a differing thickness, and its metal was heterogeneous in chemical composition. The central part of the seam contained some species in the form of bands and needles (Figure 2, *b*), as well as a Cu-base solid solution alloyed with 0.8 at.% Ti and 1.1 at.% Al. The white phase rich in zirconium (up to 15.7 at.%) adjoined it on both sides. In some cases it penetrated into the base metal to a depth of down to 100 μm (Figure 2, *b*). The data obtained suggest that, according to the constitutional diagram, the white phase Cu–Zr [14] corresponds to a stoichiometric composition of intermetallic Cu_5Zr, or

Table 3. Chemical composition (at.%) of structural components of the seam metal

Filler metal No.	*Structural components*	*Cu*	*Ti*	*Al*	*Zr*	*Ni*	*Nb*	*V*
1	Grain (solid solution)	98.6	0.5	0.5	–	0.4	–	–
	Eutectic	66.7	2.4	2.9	26.00	2.0	–	–
2	White phase	78.4	1.0	0.1	15.70	4.3	0.5	–
	Grey phase	97.1	0.8	1.1	0.30	0.1	0.6	–
3	Grey grain	93.6	5.1	0.4	0.10	0.8	–	–
	Black intermetallic	21.7	62.2	–	1.01	15.0	–	–
	Grey intermetallic	53.0	31.0	1.0	0.30	14.0 7.0	–	–
	White intermetallic	79.3	9.5	0.3	8.80	1.2	–	–
	Grey intermetallic	55.2	30.9	0.2	0.50	13.0 2.0	–	–
4	White intermetallic	77.7	11.2	0.5	9.20	0.7	–	0.7
	Grey matrix	77.5	18.9	0.7	1.00	2.0	–	0.2

possibly and to a more, complex composition of the Cu_5Ni_5Zr type.

In the case of brazing using filler metal No.3 at T_l (see Table 2) microstructure of the brazed joint was found to feature the presence of four components, i.e. a Cu-based solid solution and three intermetallics (Figure 2, *c*). In one of them (black) the content of titanium amounts to 62.2 at.%. It can be assumed, according to the constitutional diagrams, that this is intermetallic $CuTi_2$. In the other intermetallic of a grey colour the content of titanium was about 31 at.%, nickel — about 15 at.% and the balance was copper. It can be assumed that this is phase 52Cu–33Ti–15Ni. In the third intermetallic (white) the content of copper was about 79 at.% and zirconium ≈ 9 at.% (Table 3), which supposedly corresponded to Cu_5Zr. Intermetallics solidified to form continuous chains in the seam centre and along the solid solution grain boundaries (Figure 2, *c*), the seam width in this case amounting to 100 μm. Cracks and lack of penetration were detected not far from the fillets.

Results of investigations of the brazed joints in alloy Glidcop Al-25 made by using filler metal No.4 (at T_l = 860 °C and holding for 3 min) showed that the seam width ranged from 20 to 80 μm. The seam metal has two clearly defined zones. The central zone is composed of coarse (up to 14 μm) dark grains of compound 52Cu–33Ti–15Ni contained in the matrix of intermetallic Cu_4Ti (Figure 2, *d*). The light phase is non-uniformly distributed over the entire surface area of the seam (in the central zone and zone adjoining the base metal) and supposedly corresponds to

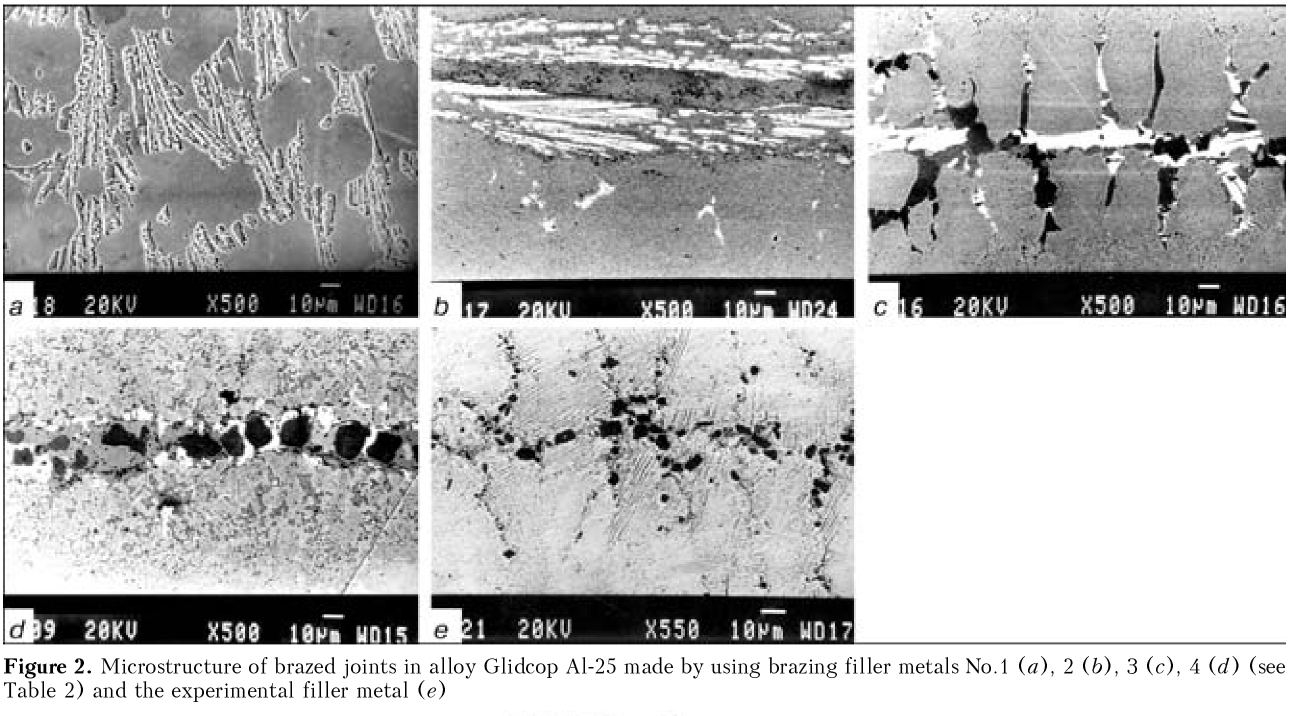

Figure 2. Microstructure of brazed joints in alloy Glidcop Al-25 made by using brazing filler metals No.1 (*a*), 2 (*b*), 3 (*c*), 4 (*d*) (see Table 2) and the experimental filler metal (*e*)

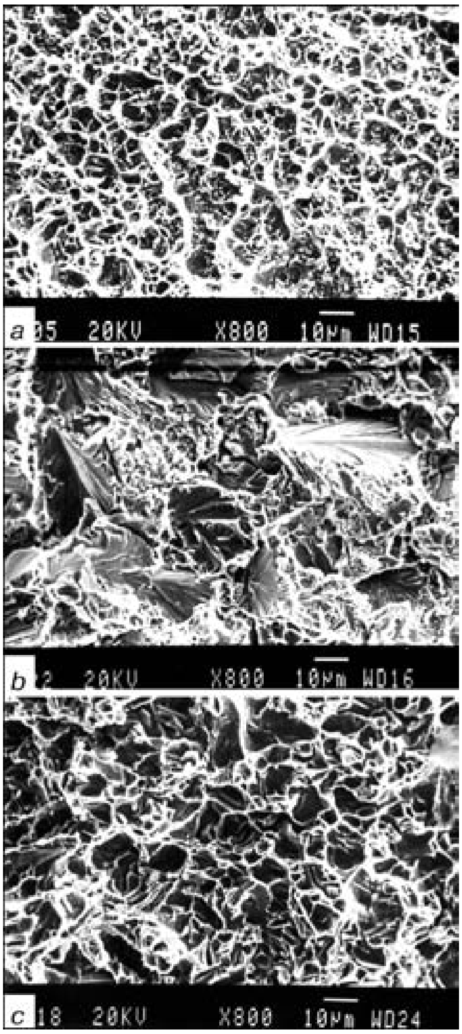

Figure 3. Fractography of fractures of brazed joints in alloy Glidcop Al-25 made by using filler metals No. 3 (*a*), 4 (*b*) (see Table 2) and the experimental filler metal (*c*)

intermetallic Cu_5Zr. The finely dispersed (dark) phase rich in vanadium (up to 14 at.%) is precipitated in both said zones also chaotically.

The butt brazed joints and base metal in the as-received condition and after annealing (T_{an} = 950 °C, 1 h) were subjected to mechanical tests. The base metal in the as-received condition had a substantial strength (σ_t = 491 MPa) and was characterised by a tough pit-type fracture and a homogeneous structure. After heat treatment the strength of alloy Glidcop Al-25 decreased by 60 MPa to correspond to that given in Table 1. Fracture is of a tough character, but pits are wider than in the previous sample, their sizes amounting to 10 µm. This can be explained by partial coarsening of the strengthening phase.

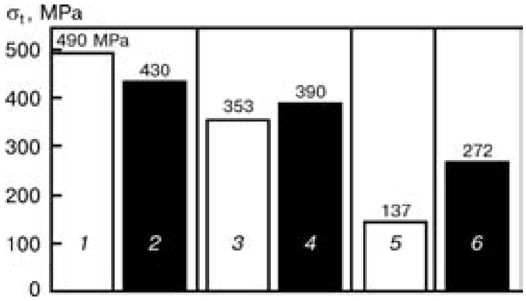

Figure 4. Results of tensile tests of base metal (*1, 2*) and brazed joints (*3–6*) (mean values) in the as-received condition (□) and after annealing (■)

Table 4. Results of mechanical tensile tests of brazed samples in alloy Glidcop Al-25

Sample No.	*Filler metal No.*	σ_t, *MPa*	$\sigma_{0,01}$, *MPa*	T_b, *°C*	τ, *min*
1	3	136.8	N/D	960	15
2	3	–	Fracture in manufacture		
3	4	310.3	245.1	860	15
4	4	234.3	234.3	990	15
5	Experimental	353.2	230.8	990	3
6	Same	353.4	219.5	990	3
7	»	397.2	217.2	990	3
8	»	382.4	218.6	990	3

Notes: 1. In samples No.6 and 8 the initial material prior to brazing was subjected to annealing at T = 950 °C, the time of holding was 1 h. 2. T_b is the brazing temperature and τ is the brazing time.

In tensile tests the brazed samples fractured in the seam with a minimum plastic deformation of the base metal in the near-seam zone. As seen from Table 4, in brazing using filler metals No.3 and 4 the resulting joints are characterised by a low strength. Results of fractographic analysis of failures of these samples exhibited the presence of a large number of regions with brittle fracture (Figure 3, *a, b*). The samples made using filler metals No.1 and 2 failed in the manufacture. So, no data on their strength properties are available.

Therefore, vacuum brazing of alloy Glidcop Al-25 using adhesion-active filler metals of the Ti–Zr–Cu–Ni system failed to provide the required strength of the brazed joints. In this connection, further investigations were conducted on samples of brazed joints made by using the experimental filler metal on a titanium base. Brazing was performed in a vacuum furnace with radiation heating at a temperature of 990 °C. The resulting joints were characterised by a good formation of the seam and fillets, as well as the absence of defects.

It is a known fact that wettability of an oxide increases with increase in affinity of the wetting molten metal to oxygen [12], and interaction of the molten metal with the oxide is determined by interaction of the metal with oxygen of this oxide. Reaction between titanium contained in the filler metal and Al_2O_3 leads to formation of an intermediate oxide TiO [11, 15], which has good electrical conductivity and mostly a metal character of the interatomic bond. This attributes to high adhesion and wetting abilities of filler metals of the Cu–Ti–Al_2O_3 system [11].

Metallography of the brazed joints showed that the seam metal had a three-phase structure. Formation of an insignificant amount of the phase rich in titanium was observed in metal of the central part of the seam. It can be concluded on the basis of the constitutional diagrams that its composition almost exactly corresponds to a stoichiometric composition of intermetallic CuTi, which solidifies along the solid solution grain boundaries in the form of discrete precipitates (see Figure 2, *e*). It is well known that this distribution of phase components is more favourable in terms of properties of the brazed joints, compared with formation of a continuous intermetallic layer. In this case the strength of this joint is determined primarily by properties of the matrix, i.e. properties of the solid solution, which is confirmed by the mechanical test results (see Table 4). The brazed joints produced using the experimental filler metal are characterised by sufficiently high and consistent values of tensile strength.

Pre-brazing heat treatment of the base material allowed an increase from 353 to 397 MPa in tensile strength of the joints, which is 81 % of strength of the base metal (alloy Glidcop Al-25 in the as-received condition) and 92 % of that after pre-brazing heat treatment. This allows a conclusion of the expediency of using the experimental filler metal for brazing the dispersion-strengthened copper alloy Glidcop Al-25. The better visualisation of advantages of this filler metal is provided by a diagram based on mean values of results of tensile tests of the brazed samples and base metal (Figure 4).

Results of fractography of the contact surfaces of fracture of the brazed joints showed the effect on topography of the fracture surface by a composition of the brazed joint metal (microstructure of its components in particular). Thus, topography of fracture of sample No.7 is characterised by a mixed character of fracture with a large number of tear ridges (see Figure 3, *c*). A relatively small size (≈ 10 μm) of the facets is indicative of a fine-grained structure of the brazed seam metal.

CONCLUSIONS

1. As found by investigations, brazing filler metals No.1 and 2 of the Zr–Cu–Ni–Ti system fail to provide sound brazed joints in the dispersion-strengthened copper alloy Glidcop Al-25.

2. Brazed joints made by using filler metals No.3 and 4 of the Ti–Cu–Zr–Ni system have low strength values (137–310 MPa).

3. The experimental filler metal provides consistent strength values of the brazed joints at a level of 350 MPa on a material in the as-received condition. Pre-brazing heat treatment of the base material promotes an increase of 8–13 % in tensile strength of the brazed joints, which in this case is $\sigma_t \cong 400$ MPa.

1. Ivanov, K.V., Grabovetskaya, G.P., Kolobov, Yu.R. (2001) Structure and mechanical properties of composite Cu–0.5 wt.% Al_2O_3 produced under the intensive plastic deformation effect. *Perspektivnye Materialy*, **4**, 78–83.
2. Vityaz, P.A., Lovshenko, F.G., Lovshenko, G.F. (2001) New high-resistant dispersion-strengthened copper materials for resistance welding electrodes. *The Paton Welding J.*, **1**, 16–21.
3. Daneliya, E.P., Rozenberg, V.M. (1978) *Internally oxidized alloys*. Moscow: Metallurgiya.
4. Daneliya, E.P., Rozenberg, V.M., Solopov, V.I. (1977) Internally oxidized copper alloys as a high-temperature conducting material. *Tsvetnye Metally*, **6**, 69–72.
5. Lee, C.K., Chin, B.A., Zinkle, S. et al. (1993) Brazing of copper-alumina alloys. *Nucl. Mater.*, **191–194**, 488–492.
6. Hosking, F.M. (1988) The effect of plating on brazing dispersion strengthened copper to graphite. In: *Abstr. of pap. of 69th AWS Annu. Meet.*, Miami, Apr. 17–22, 1988.
7. Saint-Antonin, F., Bucc, P., Barberi, D. et al. (1998) Development of Be. In: *Proc. of JAERI-Conf. on Glidcop Joint Obtained by Hot Isostatic Pressing Diffusion Bonding for In-Service Temperature*.
8. McFayden, A.A., Kapoor, R.R., Eagar, T.W. (1990) Effect of second phase particles on direct brazing of alumina dispersion hardened copper. *Welding J.*, **11**, 399–407.
9. Kvasnitsky, V.F., Samokhin, S.M., Najdich, Yu.V. et al. (1985) Interaction of filler metals with dispersion-strengthened copper during brazing. *Adgeziya Rasplavov i Pajka Materialov*, **14**, 103–108.
10. Zhuravlyov, V.S., Krasovskaya, N.A., Najdich, Yu.V. (1997) New studies of wetting non-metallic materials with metallic melts of system SiC–(Cu; Au; Al; Sn)–Si; (Al_2O_3; SiO_2; Si_3N_4; SU-200)–(In; Sn; Cu)–Sc. In: *Proc. of Conf. on Brazing in Manufacturing of Up-to-date Engineering Products*. Moscow: Znanie.
11. Najdich, Yu.V., Zhuravlyov, V.S., Chuprina, V.G. et al. Adhesion, wettability and formation of intermediate phases in titanium-containing melt–oxide systems. *Poroshkovaya Metallurgiya*, **11**, 40–45.
12. Eryomenko, V.N., Najdich, Yu.V., Lavrinenko, I.F. (1968) *Sintering in the presence of a liquid metallic phase*. Kyiv: Naukova Dumka.
13. Kalin, B.A., Sevryukov, O.N., Fedotov, V.T. et al. (2001) New amorphous filler metals for brazing titanium and its alloys. *Svarochn. Proizvodstvo*, **3**, 37–39.
14. (1997) *Constitutional diagrams of bimetallic systems*. Refer. Book. Ed. by N.P. Lyakishev. Moscow: Mashinostroenie.
15. Bang, K.S., Liu, S. (1994) Interfacial reaction between alumina and Cu–Ti filler metal during reactive metal brazing. *Welding J.*, **3**, 54–60.

PHASE COMPOSITION OF Fe–C–Cr–Al SYSTEM COATINGS PRODUCED BY THE METHOD OF ELECTRIC ARC METALLIZING

V.I. POKHMURSKY[1], **M.M. STUDENT**[1], **I.I. SIDORAK**[1], **I.A. RYABTSEV**[2] and **Yu.M. KUSKOV**[2]
[1]G.V. Karpenko Physical-Mechanical Institute, NASU, Lviv, Ukraine
[2]The E.O. Paton Electric Welding Institute, NASU, Kyiv, Ukraine

Phase composition and processes of structure formation in coatings produced by the method of electric arc metallizing have been investigated. It was established that structure of coatings of Fe–C–Cr–Al system consists of martensite, troostite and residual austenite with a different content of alloying elements. With increase in aluminium content by more than 2 % in the flux-cored wire charge the adhesion strength of coating with a base metal is increased, and an alloyed ferrite is simultaneously appeared in the coating structure.

Key words: *electric arc metallizing, coatings, phase composition of coatings, microstructure of coatings, flux-cored wires*

Development of optimum compositions of electrode materials and, in particular, flux-cored wires for the electric arc metallizing (EAM) providing the coatings with preset physical-mechanical properties is impossible without information about the phase composition and processes of structure formation in coatings depending on the chemical composition of the electrode material. In most flux-cored wires used for EAM of crankshafts of the internal combustion engines, different axles and others, carbon, chromium and aluminium are the main elements which are responsible for the phase composition of the coatings. The article is devoted to the investigation of a combined effect of carbon and aluminium in the flux-cored wire ferrochromium-based charge on the phase composition of coatings.

Materials and procedure of investigations. To manufacture 1.8 mm diameter flux-cored wires for EAM, a cold-rolled 0.4×10 mm section strip of steel 08 (rimmed) was used. Ferrochromium (FKh-200, FKh-800), ferromolybdenum (FMo-60), ferrosilicium (FS-65), aluminium powder (PA-4), crucible graphite (GT-1), iron powder (PZhO) were used as charge materials. Several flux-cored wires were manufactured for investigations. The chemical composition of charge for these wires is given in Table 1. For comparison, the coatings deposited by wire of U8 grade were also investigated.

Table 1. Composition of flux-cored wires charge, chemical and phase composition of coatings

Conditional description of wire	*Composition of charge flux-cored wires, wt.%*						*Elements, wt.%**		*Phase composition of coating*		
	Ferrochromium	*Ferro-silicium*	*Ferro-molybdenum*	*Graphite*	*Al*	*Fe*	*C*	*Cr*	*α-Fe/γ-Fe ratio*	*Cementite*	*Oxides*
Solid wire U8	–	–	–	–	–	–	0.8/0.18	–	15/1	Up to 5 % of volume	Traces FeO
Flux-cored wire:											
KhSM-1	70 (FKh-200)	10	20	–	–	–	0.4/0.25	10.5/10	8/1	Traces	Traces FeO
KhSM-2	70 (FKh-800)	10	20	–	–	–	1.1/0.6	10.3/10	3/1	Same	Traces Fe_2O_3, Fe_3O_4
KhYu-1	55 (FKh-800)	–	–	5	2	38	1.7/1.1	10/9	1/1	»	Traces FeO, Fe_2O_3, Fe_3O_4
KhYu-2	60 (FKh-200)	–	–	10	2	28	2.5/1.5	9/9	2/3	»	Traces FeO, Fe_2O_3, Fe_3O_4

*In numerator — estimated content, in denominator — actual content.

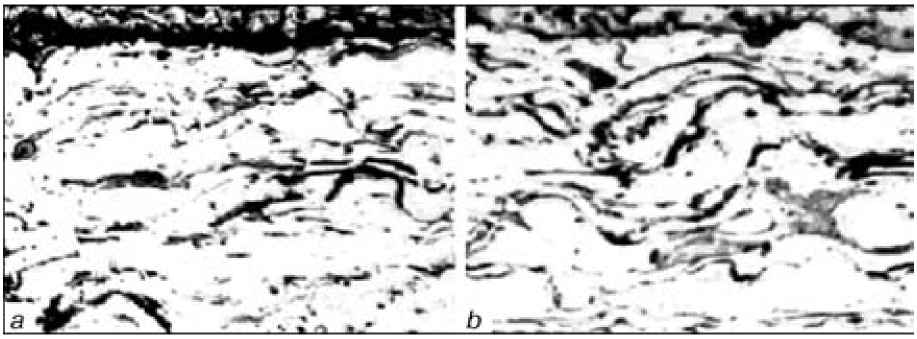

Figure 1. Microstructure of coatings with different content of aluminium in the charge of flux-cored wires: *a* — 2 %; *b* — 15 % (×200)

The coatings were deposited using a metal spraying gun GT-1 designed at the G.V. Karpenko Physical-Mechanical Institute. Conditions of the coating deposition: voltage 32 V, current 140 A, air pressure 0.5 MPa, distance from the gun to the sample 100 mm.

Content of carbon in coatings was determined by a coulometric method, while chromium, aluminium and silicon were determined by a spectral method using the diffraction steeloscope SL-13. Distribution of drops by sizes was determined in spraying flux-cored wires on a pressed snow with a next mesh analysis of solidified drops by fractions.

The phase composition of coatings was examined in DRON-3 diffractometer (U = 32 kV, I = 13 mA) at a 0.05 scanning pitch using computer processing. Identification of phases was made using tables of file JCPDS-ASTM. Volumetric ratio between phases α-Fe and γ-Fe was calculated by integral intensity of diffraction lines. Distribution of elements in coatings was determined in scanning electron microscope.

Experimental results and their discussion. Coatings produced in spraying of flux-cored wires consist of greatly deformed grains-lamellas which are poorly etched in 3 % HNO_3 solution (Figure 1). At the intergrain boundaries the inclusions of oxide films are observed, whose composition corresponds to FeO in use of ferrochromium FKh-200 in the flux-cored wire charge and FeO, Fe_2O_3, Fe_3O_4 in use of FKh-800.

Examinations showed that due to graphite adding to the charge composition it is impossible to increase greatly the carbon content in the coating. Thus, in adding 5 % of graphite to the charge of the ferrochromium FKh-800-based flux-cored wire 0.85 % C is contained in the coating, while at 15 % of graphite — 1.32 % C. This is connected with the fact that carbon in the form of a free graphite is burnt out greatly during the EAM process.

It was established that the structure of coating produced in use of U8 steel solid wire consists of products of martensite decomposition, such as troostite, sorbite and cementite. Inclusions FeO were revealed in the coating. The presence of a small amount of austenite is explained by the fact that carbon in separate large drops burns out to a smaller degree than in small drops, and its high concentration increases the stability of austenite at fast solidification of the largest drops.

With carbon content increase in the coating its phase composition is changed and the content of a residual austenite is increased. Thus, when flux-cored wire of ferrochromium FKh-200 is used as a charge base the carbon content in the coating is 0.18 %, and the amount of residual austenite in structure is negligible at ratio of phases α-Fe/γ-Fe = 8/1. Amount of cementite is small. It proves that a part of α-Fe is available in the form of martensite, alloyed with chromium, while its negligible part is in the form of martensite decomposition products, such as troostite. When ferrochromium FKh-800 is used as a base of the flux-cored wire charge the content of carbon in the coating is increased and amounts to 0.66 %. The amount of residual austenite in the coating structure is also increased at ratio of phases α-Fe/γ-Fe = 3/1 and approximately the same composition of α-phase.

At additional graphite adding to the composition of the flux-cored wire charge the amount of residual austenite is increased in the coating structure and its content reaches maximum at 10 % of graphite at ratio of phases α-Fe/γ-Fe = 2.3. From data of [1] this structure possesses good tribological characteristics. Probably, carbon which is added to the flux-cored wire charge in the form of graphite is not transferred completely to the solid solution of the coating, but remains in a free state (possibly, at the boundaries of lamellas from which the coating is composed). This is confirmed by the traces of a free graphite in X-ray

Table 2. Size of electrode metal drops and content of carbon and chromium in them

Size of drops, μm	*Wire U8*	*Flux-cored wire KhSM-2*		*Flux-cored wire KhYu-2*	
	C, wt.%	*C, wt.%*	*Cr, wt.%*	*C, wt.%*	*Cr, wt.%*
10–50	0.22	1.2	7.0	0.60	9.0
50–150	0.26	1.5	8.5	0.68	9.5
160–200	0.30	2.3	10.0	0.83	11.5

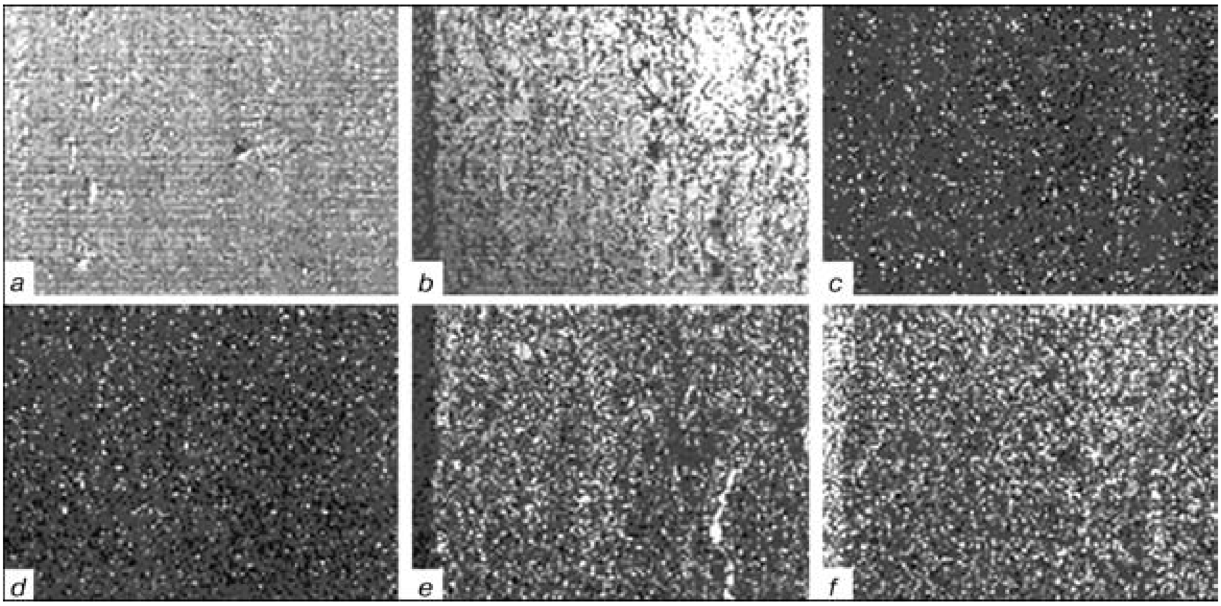

Figure 2. Distribution of alloying elements in coating, deposited using flux-cored wire of FeCr + Al + C type, obtained in electron scanning microscope: *a* — in primary electrons; *b* — in secondary electrons; *c* — Al; *d* — Si; *e* — Cr; *f* — Fe (white points — place of a given element location)

photographs and also by the fact that with increase in graphite content in charge the tensile strength and adhesion strength are decreased by 30 and 40 %, respectively. A free graphite plays a role of a lubricant thus improving the tribological characteristics of the coating.

The mesh analysis of a fractional composition of coatings from the flux-cored wire with and without graphite shows that the size of drops in EAM is varied within 10–200 μm and, here, the mass share of drops of 10–50 μm is ≈ 60 %. Small drops contain lower amounts of carbon and chromium. Moreover, the concentration of carbon is larger both in small and large drops for flux-cored wires which contain graphite (Table 2). It is evident that during EAM the saturation of coating with carbon takes place due to high-carbon ferrochromium and graphite. In structure of all the coating with a ferrochromium FKh-800-based charge there are traces of all three oxides of iron: FeO, Fe_2O_3, Fe_3O_4.

As was stated in [2], a high adhesion of coatings with microhardness of more than 5000 MPa is provided owing to aluminium contained in the flux-cored wire charge. Aluminium interacts with iron in the drop melt at exothermal reactions evolving a large amount of heat:

$3Fe + Al = Fe_3Al + 0.75$ kJ/g of flux-cored wire charge;

$2/3Fe_2O_3 + 2Al = 4/3Fe + Al_2O_3 + 3.5$ kJ/g of flux-cored wire charge;

$2/3Cr_2O_3 + 2Al = 4/3Cr + Al_2O_3 + 2.7$ kJ/g of flux-cored wire charge.

Temperature of drops which contain aluminium is by 200–400 °C higher than that of drops which do not contain it. In addition, in contact with surface on which the coating is deposited the aluminium in a molten drop reacts with oxide film on it during exothermal reaction. Moreover, the temperature in the place of contact is increased that provides the better adhesion of the coating sprayed with a base.

Table 3. Composition of flux-cored wire charges, chemical and phase composition of coating at different content of aluminium and carbon in it

Conditional description of wire	*Composition of charge of flux-cored wires, wt.%*				*Elements in coating, wt.%*[*]			*Phase composition of coating*		
	Ferrochromium FKh-800	Graphite	Al	Fe	C	Cr	Al	α-Fe/γ-Fe	Cementite	Oxides
KhYu-3	70	–	2	28	1.02/0.6	10.3/10	0.4/0.4	3/1	Traces	Traces Fe_2O_3 and Fe_3O_4
KhYu-4	70	5	2	23	1.6/1	11/10.5	0.4/0.4	1.4/1	Same	Traces FeO, Fe_2O_3, Fe_3O_4
KhYu-5	60	5	10	25	1.5/0.9	10.5/9.8	2.2/2	1.4/1	»	Same
KhYu-6	60	5	15	20	1.5/0.95	10.5/10.2	3.2/3	2.2/1	»	»
KhYu-7	60	5	20	15	1.5/0.9	10/9.7	4.3/4.1	9/1	»	»

[*] In numerator — estimated content, in denominator — actual content.

Coming from these considerations the effect of aluminium on structure and properties of the coating produced by EAM method was examined (Table 3). X-ray diffraction analysis of coatings which contain up to 3 % of aluminium shows that their structure consists of α-Fe and γ-Fe. At 4.1 % Al content, the austenite in coating structure almost disappears. Distribution of chromium and aluminium in the coating is sufficiently uniform and narrow areas enriched with aluminium and chromium are observed only at the lamellas boundaries. These areas are, probably, oxide films consisting of oxides of aluminium and chromium: Al_2O_3 and Cr_2O_3 (Figure 2).

Microhardness of coatings containing 3 % Al is 4000–6000 MPa. Minimum values correspond to microhardness of austenite, while maximum values correspond to microhardness of martensite. At 4.1 % Al content the microhardness of coatings drops abruptly to 2000–3000 MPa. This is due to the fact that martensite and austenite are disappeared in the coating structure and δ-ferrite is appeared, being alloyed with aluminium and chromium. This change in the phase composition was caused by a combined effect of aluminium and chromium as the strongest ferrite-forming elements. The almost absence of carbides in the coating structure proves that aluminium forces out carbon from a crystalline lattice of iron. Carbon, being in a free state, is in a very fine-dispersed form and not revealed during metallographic examination.

CONCLUSION

Coatings of Fe–C–Cr–Al system, produced from flux-cored wires by the EAM method are formed from molten drops with a different content of alloying elements. Fine drops as compared to coarse drops have a lower content of carbon and chromium. Coating structure — martensite, troostite and residual austenite with a different content of alloying elements.

Increase in aluminium content in the flux-cored wire charge leads to the increase in adhesion strength of coating with a base, thus causing a simultaneous appearance of alloyed ferrite in the coating structure. At 4.1 % Al content the coating structure becomes completely almost ferritic.

1. Pokhmursky, V.I., Shirokov, V.V., Student, M.M. et al. (1997) Wear-resistant thermal coatings from flux-cored wires of Fe–Cr–C system. *Problemy Trybologii*, **3**, 48–56.
2. Student, M.M. (1998) *Development of protective and restored electrometallised coatings using flux-cored wires.* Syn. of Thesis for Cand. Techn. Sci. Degree. Lviv.

SELECTION OF THE COMPOSITION OF WELDING FLUXES, ALLOWING FOR THE STRUCTURAL CHARACTERISTICS OF THEIR MELTS

V.G. KUZMENKO[1], **V.S. TOKAREV**[1], **V.I. GALINICH**[1], **V.E. SOKOLSKY**[2] and **V.P. KAZIMIROV**[2]
[1]The E.O. Paton Electric Welding Institute, NASU, Kyiv, Ukraine
[2]Taras Shevchenko Kyiv State University, Kyiv, Ukraine

Investigation of the structure of slag melts and development of the concept of their structural bacisity formed the basis for suggesting the principle of preparing flux compositions with the basicity, varying under the impact of the thermal cycle of welding.

Key words: *electric arc welding, welding fluxes, slags, selection of flux composition, structure of slag melts, bacisity*

A number of often incompatible requirements of technological, metallurgical, sanitary-hygienic and economic nature [1, 2] are made of fluxes for electric arc welding, each of which in the assumption of its independent fulfilment may be satisfied by applying types (compositions) of fluxes, which differ significantly from each other [3, 4]. Just as contradictory are the requirements to flux properties, which are responsible for the nature of running of physico-chemical processes in the functional zones of the weld pool, which determine the quality characteristics of the weld [3–5].

This creates a problem of selection of the composition of welding fluxes, capable of providing both the required technological characteristics of the welding process (arcing stability, absence of porosity, good formation of welds), and a sufficient level of strength properties of the weld. In particular, it is known from practical work that in order to produce well-formed welds without pores, preference should be given to manganese-silicate (acid) and fluorine-containing fluxes. On the other hand, in order to produce a less oxidised weld metal, purer in terms of non-metallic inclusion (NMI) content, with high strength properties, it is rational to use fluxes of basic type, consisting of chemically and thermally stable oxides.

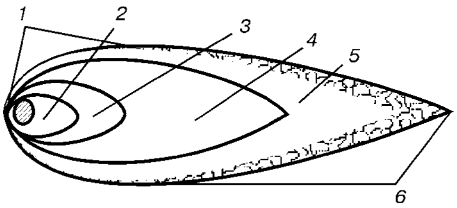

Figure 1. Zones of weld pool and their functions (optimal types (compositions) of welding slags are given in parenthesis): *1* — melting of metal and flux (acid, silicate, fluorine-containing); *2* — arc impact (basic); *3* — turbulent flow of metal (basic); *4* — laminar flow of metal (basic); *5* — immobilized liquid metal (acid, manganese-silicate); *6* — solid-liquid state of the metal (aluminate with formation of acicular ferrite)

If we take into account the connection between the consequences of fluxes application and ambiguity of their functions in individual zones of weld pool, then, hypothetically, an ideal flux, providing the most effective functioning of these zones and high quality of the weld, should at the same composition have the ability to change its characteristics, depending on the position in the weld pool, namely acquire «acid» properties in its cold zones and «basic» in the hot zones. A schematic of weld pool (Figure 1) can give an idea of the nature of variation of the flux properties. In this schematic pool zones are designated, their functional purpose is shown, and slag types (compositions) most suitable for them are given [4].

Even an approximate estimate of all the consequences of flux application in electric arc welding still has not been made. A multitude of diverse physico-chemical processes should be studied and compared, and a considerable scope of research of the concentration and temperature dependencies of the slag properties should be performed.

For systematisation of the factors, contributed by the fluxes and influencing the properties of the weld, such a collective characteristic of fluxes as basicity is also widely used, alongside with flux composition and physico-chemical properties [1]. The significance of the concept of basicity consists in that it permits reducing the diversity of welding fluxes to two groups, namely acid and basic. Basicity value, equal to a unity, is the division line for them.

Application of a concept such as basicity allows systematising the slags in accordance with a certain scale, where the measure of basicity is the basicity index. Such a systematisation allows clarifying to a certain extent the evaluation of the slag properties. It cannot be stated, however, that the connection between the current concept of basicity and slag compositions is of an unambiguous nature. A multitude of slag types, differing both by their components and their proportions may correspond to the same value of basicity. However, serious drawbacks of the current concepts of basicity (ratio of concentrations of the basic and acid oxides, established by elementary determination of slag composition) are absence of a correlation with the actual nature of slag melts, as well as use in calculations of just the concentration dependence of variation of slag basicity without allowing for the influence of temperature. Therefore, a scientifically-grounded selection of welding flux composition requires obtaining information on the basicity of welding fluxes, proceeding from the actual condition of their melts.

Slag properties, including their basicity, depend on their atomic-molecular structure. Over the last years, a procedure for determination of structural basicity of slags has been proposed [9, 10], based on similarity of the structure of crystalline (glass-like) and liquid condition of slags [6], results of radiographic examination of the structure of slag melts [7] and developed theory of close packing of oxygen ions [8], characteristic for the structure of welding fluxes of oxide and salt-oxide type. Individual features of behaviour of ions, affecting the formation of slag structure [11], were taken into account, which were established through analysis of the position of the respective peaks on the curves of radial distribution of atoms, area of these peaks, as well as their shape [9, 10].

In keeping with the geometrical and electrostatic characteristics, the cations in the slags, in terms of structure formation, may be divided into three groups. These primarily are cations, forming complexes, the most striking representative of which in welding slags composition is Si^{4+}. This cation has the strongest acid properties, which determines the respective contribution of silicon oxide to flux basicity. A special feature of this component is its ability to form thermally stable complex structures with oxygen due to directionally-concentrated covalent bonds, thus predetermining the high viscosity and low electric conductivity of silicate slags.

Mg^{2+}, Ca^{2+}, Na^{+}, K^{+} cations are Si^{4+} antipode in the composition of welding fluxes. They act as elements, breaking up the complex structures, formed by Si^{4+} cation and promote an increase of the basicity and improvement of the translational properties of slags, namely viscosity and electric conductivity.

Ions of amphoteric and transition metals, namely aluminium, titanium and zirconium, have a special role in changing the basicity in slag heating in the molten condition. Having a fraction of the covalent bond, essentially smaller than Si–O coordination, these ions are capable of fulfilling dual functions due to the change of cation-anion role, and, adapting to the change of the slag condition, can essentially influence the basicity. Thus, when aluminium has the role of an anion, its oxygen coordination is 4. In this case aluminium acts as silicon analog, substituting it in complex silicon-oxygen anions. At coordinate number of aluminium ion equal to 6, it takes on the basic properties, and is similar to magnesium oxide as to its action in the slags [12].

Therefore, composition is the most important factor, on which the structure of slags and their properties are dependent, respectively. Another factor, influencing the nature of variation of slag properties, is temperature. The difference between the concen-

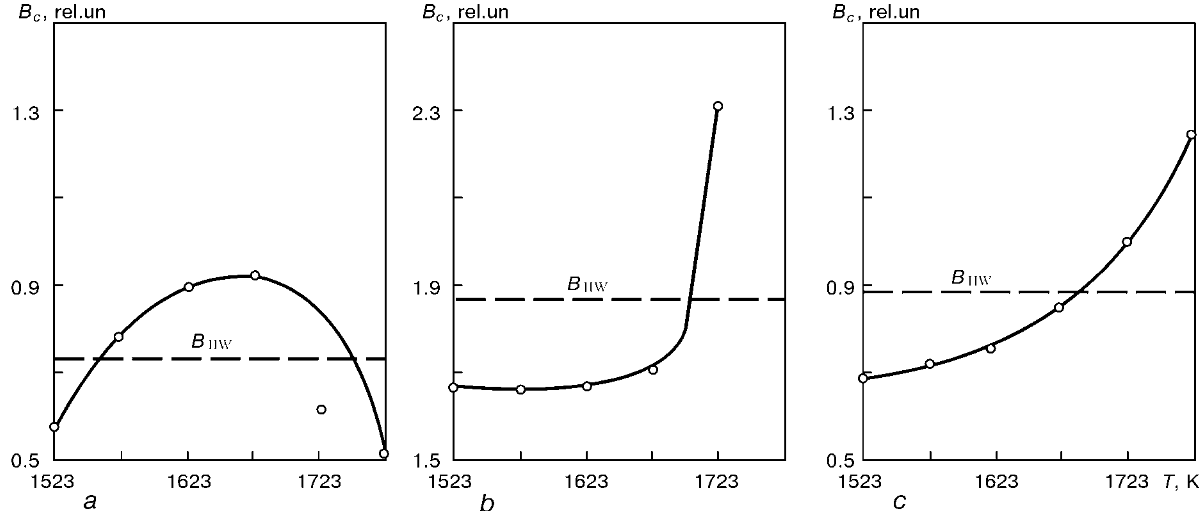

Figure 2. Change of structural basicity B_c of welding slags of different grades, depending on temperature: *a* — AN-348-A; *b* — AN-15-M; *c* — AN-67 (B_{IIW} — basicity by IIW formula)

tration and temperature impact on the slag consists in that while its composition change leads to irreversible changes of the structure and properties, when going back to the initial temperature, also the slag parameters are restored. Many authors [6, 13] note that temperature increase also influences the change of the structure of slag melts in the same way as at addition of basic oxides to their composition. The difference lies only in the mechanism of achieving the result. While at addition of basic oxides coarse formations in slags break up due to weakening of bonds of ionic nature in the point of introduction of the respective cations, temperature increase has a similar effect due to intensifying of the oscillatory motions of the ions. Therefore, it is anticipated that increase of molten slag temperature will lead to an increase of their structural basicity.

In order to verify the above assumptions, we have studied the variation of structural basicity of three essentially different types of fluxes at the temperatures of 1523–1723 K [10, 14]. One flux was acid and in its composition corresponded to AN-348-A grade, the second was of a pronounced basic type (AN-15-M), and in the third neutral flux the prevailing component was aluminium oxide (AN-67). Basicity was determined, proceeding from the structural parameters, established by us during X-ray diffraction analysis. Its dependence on temperature is shown in Figure 2. From the Figure it is seen that the melts of fluxes of the basic and neutral types are strongly affected by the temperature factor: the flux acquires higher basicity after melting. Acid flux of AN-348-A grade shows some unexpected behaviour. After melting it becomes somewhat less acid, the value of its basicity approaching a unity. With further heating in the studied temperature range, this flux becomes even more acid, compared to the initial condition. This is attributable to intravolume redistribution of oxygen, belonging to manganese ion, and the respective increase of the fraction of temperature-stable covalent bond in Si–O coordination [6].

The nature of variation of structural basicity of fluxes of basic and neutral (aluminate) type also has fundamental differences. Unlike AN-15-M flux, the melt of the aluminate flux increases its basicity at heating in a more moderate manner, which is, probably, due to the presence of 14 wt.% SiO_2 and 36 wt.% Al_2O_3 in its composition, as well as the ability of the latter to change the coordination number, depending on the acid-basic characteristics of the environment. Aluminium ion, transforming into a tetracoordination, completes the silicon-oxygen carcass. This limits the increase of the slag basicity, caused by the tendency for decomposition of its structure in heating. Increase of the fraction of six-coordinate aluminium ion leads to breaking up of silicon-oxygen formations. This factor restrains the lowering of basicity of the cooling aluminate slag. Thus, the impact of the temperature and concentration factors causes such structural changes in aluminate slags, which affect their basicity and other properties in wider ranges than it is possible for fluxes of acid and basic types. This creates prerequisites for selection of flux compositions, capable of adapting their properties to the condition of individual zones of the weld pool, which opens up wider possibilities for development of fluxes with high process and metallurgical characteristics.

Let us consider the nature of variation of structural basicity and viscosity of melts of fluxes of acid (silicate), aluminate and basic types, correlated with the thermal cycle, and, therefore, with their position relative to the zone of weld pool (Figure 3). Selection of these particular properties of fluxes is based on their significance in determination of the degree of metal oxidation and quality of weld formation.

Acid high-silicon fluxes are characterised by a high activity of silicon oxides. In the presence of calcium fluoride, especially at the melting stage, silicon oxide intensifies the formation of silicon tetrafluoride SiF_4, which improves the weld pool protection from air and neutralises the adverse influence of hydrogen. Acid high-silicon fluxes form viscous melts on weld pool surface and even in its high-temperature zones. This

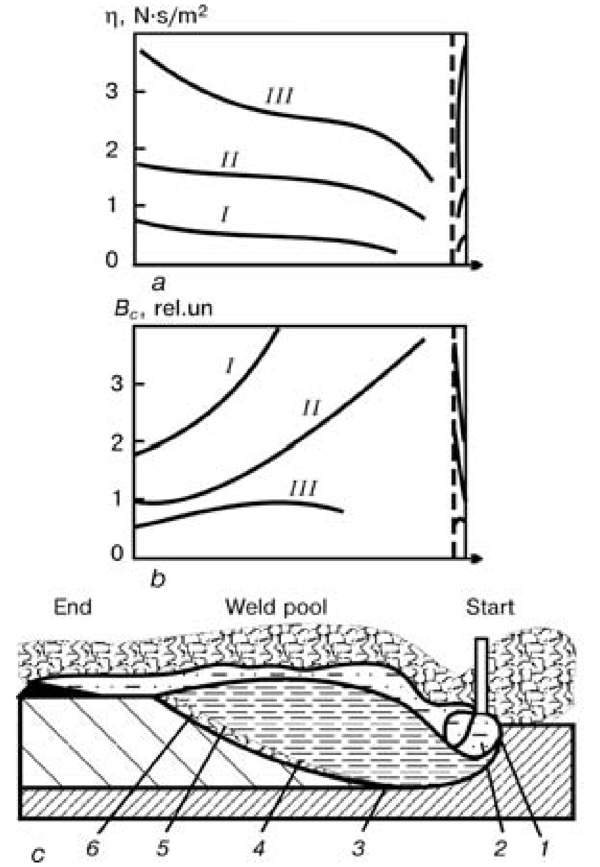

Figure 3. Change of viscosity of slags η (*a*) of different types and basicity B_c (*b*), depending on their position relative to weld pool zones (*c*): *I* — AN-15-M; *II* — AN-6; *III* — AN-348-A (*1–6* — see Figure 1)

provides their high forming ability due to effective suppression of weld pool disturbances [5]. However, their high content of silica and manganese oxides, active in relation to the liquid metal, leads to its saturation with oxygen, particularly in the high-temperature zones of the weld pool [1]. This results in formation in the weld metal of a considerable amount of NMI.

Basic flux melts behave in a reverse manner in the weld pool. In heating the thermally weak ion bonds break up in their structure, as a result of which the initial basicity of such fluxes is even more enhanced and is maintained over the entire surface of weld pool.

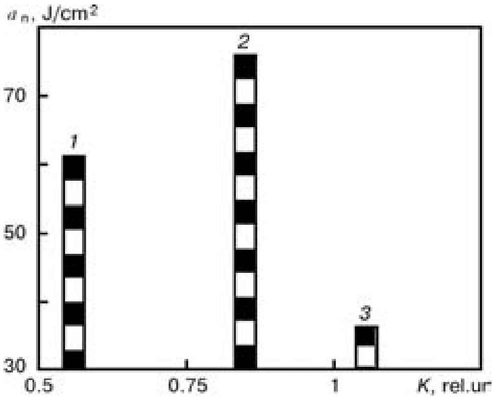

Figure 4. Change of comparative impact toughness a_n of the metal of welds made, using fluxes of different types: *1* — AN-65; *2* — AN-67; *3* — AN-60

The basic flux melts, covering its surface, have a low viscosity, which predetermines their limited forming capabilities. A positive aspect of application of basic fluxes is the absence of silica and manganese oxides in them, thus limiting the level of metal saturation with oxygen and creating favourable conditions for removal of NMI.

Unlike the acid (silicate) and basic melts, those of the fluxes of aluminate type provide the following advantages, due to changing of their structure in the weld pool functional zones, having different temperatures:

- form in zone *1* relatively acid slags, providing effective gas shielding of weld pool;
- increase the slag basicity in zone *2* and limit oxygen transition into the molten metal;
- resist lowering of slag viscosity in zone *3* due to aluminium ion transition from an octa-coordinate state into a tetra-coordinate state, which allows suppressing disturbances on weld pool surface;
- form in zones *3* and *4* basic relatively low-viscous slags at reverse restructuring of the aluminium ion into an octa-coordinate state and, thus, promote removal of NMI from the metal;
- form in zone *5* acid relatively viscous slags, thus limiting the probability of appearance of the respective defects.

Thus, the difference of neutral fluxes of aluminate type from the acid and basic ones is the ability to change their basicity, stay in the acid condition in weld pool low-temperature zones *1* and *5* and become basic in its high-temperature zones *2–4*. This brings them closer to the hypothetical ideal flux, the requirements to which were formulated by us above. As a result of performance of a number of experiments, it was established that the total content of aluminium and silicon oxides in welding fluxes of this type should be 40 to 60 %. In this case, in order to provide enhanced mechanical properties of weld metal, particularly at low temperatures, it is necessary for the aluminium oxide to prevail in the composition of such fluxes.

There have been a lot of publications recently, where the authors correlate the improvement of weld metal mechanical properties, particularly cold resistance, in steel welding, with the presence of a considerable amount of acicular ferrite in its structure. Many researchers attribute its appearance to a quite low (0.02–0.03 %) content of oxygen and presence of nitrides of titanium, aluminium, boron in the weld metal, as nuclei in metal solidification [15–19]. In zone *6* all the changes of weld pool metal, occurring during interaction with the slag in the previous zone, are observed. Therefore, the composition of NMI, formed with the participation of the welding slag, will predetermine the weld metal structure. As confirmed by the results of metallographic analysis [20], such conditions are rather completely satisfied, when using aluminate flux of AN-67 type, also containing titanium, zirconium and boron oxides. This, probably,

Table 1. Content of oxygen, nitrogen and hydrogen in the weld metal, produced in welding 09G2BT steel with Sv-09GNMT wire, using the studied fluxes

Flux grade	*Weight fraction of elements, %*		
	[O]	*[N]*	*[H]*
AN-60	0.049	0.012	0.00014
AN-67	0.030	0.013	0.00009

may account for the higher values of impact toughness of weld metal, produced using flux of the above grade. Figure 4 shows the change of impact toughness of welds, when using fluxes of various types, correlated with the dimensions of NMI via a relative dimensionless parameter K, reflecting the tendency for their refinement [20].

Dependence of physical properties of AN-67 type flux, namely viscosity and electric resistance, on temperature is shown in Figure 5 [21]. The nature of the change of structurally-sensitive properties of the slag is indicative of a delayed tendency to decomposition of its respective structural formations. This is confirmed by the data of the change of electric conductivity R in coordinates $\lg 1/R - 1\cdot10^4/T$ (Figure 6). When fluxes of AN-67 type are used, viscous slags are formed on weld pool surface, which provides a good quality of weld surface in multiarc welding in boost modes.

Structural studies of slag melts and theoretical prerequisites, following from them, were the basis to develop a number of grades of fused welding fluxes for different industries.

Flux of AN-22-M grade is designed for welding medium-alloyed steels with austenitic wire. Its high technological and metallurgical characteristics are provided at a summary content of aluminium and silicon oxides in the range of 38 to 46 wt.% with a certain increase of silica content and flux basicity by IIW formula up to 1.35.

Flux of AN-66 grade became applied in shipbuilding for welding the butt and tee joints of carbon and low-alloyed steels at higher speeds. Its use ensures a good separation of the slag crust. Content of complex-forming oxides in this flux is 37–53 %, its basicity by IIW formula is close to 0.9.

The principle of adaptation of the properties of aluminate slag to the functional problems of weld pool zones was implemented in the most complete manner in development of the flux of AN-67 grade, the basicity of which by IIW formula is 0.75. Total content of complex-forming oxides in this flux is 45–55 wt.%, this allowing welding to be performed at high speeds and producing well-formed welds. Addition of up to 40 % Al_2O_3 and limited amount of manganese and silicon oxides (up to 15 % each) in the welding slag of AN-67 flux results in a significant reduction of metal oxidation in the zone of high temperatures of the weld pool, effective removal of NMI from the post-arc zone and lowering of their content in the weld metal (Tables 1 and 2) [21].

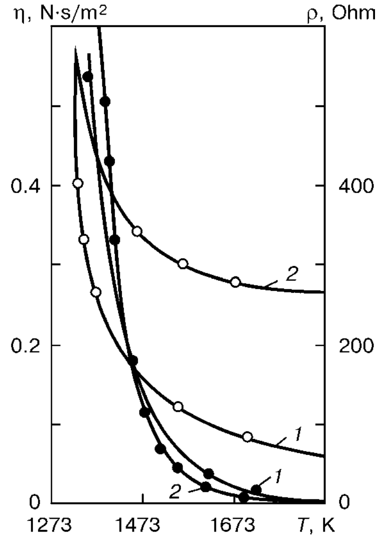

Figure 5. Change of physical properties of fluxes of grades AN-67 (*1*) and AN-60 (*2*), depending on temperature: ○ — viscosity; ● — electrical conductivity

Results of metallographic studies demonstrated that compared to the metal of welds, made using fluxes of AN-60 and AN-67 grades, in the latter a small fraction of iron-manganese-silicate glasses, sulphides and film oxysulphides is found in addition to lowering of the volume fraction of NMI. Round-shaped manganese-alumosilicate inclusions and corundum particles also appeared. In addition to round-shaped sulphide and oxysulphide particles, located along the boundaries of primary austenitic grains, the metal also contains compact inclusions of titanium oxides and irregular-shaped particles of titanium nitride [15].

For more than 15 years now fluxes of AN-67 type have been made in Nikopol Plant of Ferroalloys (Ukraine), Novomoskovsk Pipe-Making Plant and Chelyabinsk Pipe-Rolling Mill (Russia). The above fluxes are used both in Ukraine (Khartsyzsk Pipe-Making Plant) and in Russia (Chelyabinsk Pipe-Rolling Mill, Vyksunsk Metallurgical Works) in welding large-diameter pipes, designed for transportation of

Table 2. Characterisation of NMI in the weld metal, produced in submerged-arc welding with fluxes of AN-60 and AN-67 grades at two-layer deposition [21]

Flux grade	*Layer No.*	*Volume fraction of NMI, %*	*Number of NMI (pcs) of size, mm*				*Total*
			0–0.4	*0.4–1.2*	*1.2–2.0*	*> 2.0*	
AN-60	1st	0.327	70	539	232	119	960
	2nd	0.590	101	841	313	128	1383
AN-67	1st	0.241	64	485	194	50	793
	2nd	0.220	81	615	220	69	981

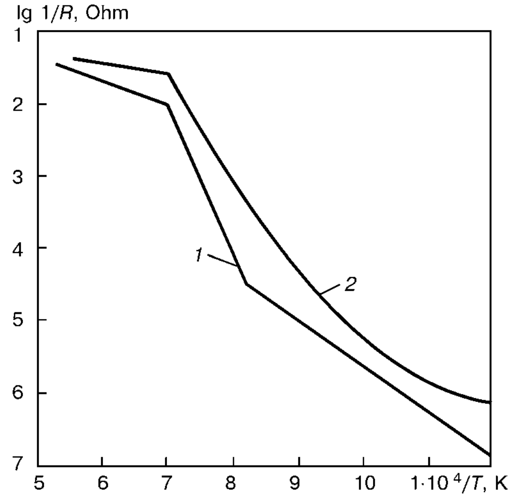

Figure 6. Change of electric conductivity of fluxes of grades AN-67 (*1*) and AN-60 (*2*), depending on temperature in lg $1/R$–$1\cdot10^4/T$ coordinates

gas- and petroleum products, also at low temperatures.

CONCLUSIONS

1. Incompatibility of the requirements of technological and metallurgical nature made of fluxes, used in electric arc welding, as well as mutually exclusive nature of occurrence of physico-chemical processes in the weld pool, due to extreme-asymmetrical thermal cycle of metal heating, limit the possibility of selection of their composition, as being just of acid or basic type.

2. Based on the results of X-ray diffraction analysis and data on valent-structural state of ions (coordination numbers, spacing of ion groups, profile of curves of radial distribution of atoms), the concept of structural basicity was developed, which is used to take into account the influence of both the composition and temperature of flux melts, due to their atomic-molecular nature.

3. At heating up to 1523–1773 K the acid properties of the initially acid flux AN-348-A are enhanced, activity of silicon oxide rises, and the high viscosity of the melt is preserved. In welding this provides good formation of welds without pores. Fluxes of manganese-silicate type intensively oxidise the weld pool metal as a result of reduction of silicon and manganese oxides, thus promoting formation of NMI in the weld metal.

4. Structural basicity of the initially basic flux AN-15-M is significantly enhanced in melting due to breaking up of weak ion bonds in its structure. Basic fluxes in welding form low-viscous slags on the weld pool surface, thus markedly impairing their forming ability. However, the absence in the composition of these fluxes of readily reduced oxides of silicon and manganese limits the processes of oxidation of weld pool metal and formation of NMI in the weld metal.

5. Aluminate fluxes with a certain combination of oxides of complex-forming, modifying and intermediate nature, as a result of transformation of their structures and acid-basic properties may form acid melts in weld pool «cold» zones, and basic ones in the «hot» zones.

6. The ability of aluminate fluxes of neutral type to adapt to the condition of weld pool zones, changing their acid-basic properties, and thus provide both high welding-technological and metallurgical characteristics of the process, is implemented in development of a number of welding flux grades. They are used with success in shipbuilding, in welding large-diameter pipes for critical applications in gas and oil pipelines, as well as in other industries.

1. Rabkin, D.M. (1951) Flux AN-348-A. *Avtomatich. Svarka*, **4**, 32–43.
2. Podgaetsky, V.V., Kuzmenko, V.G. (1988) *Welding slags*. Kyiv: Naukova Dumka.
3. Kuzmenko, V.G., Galinich, V.I., Tokarev, V.S. (1997) On typical zones of welding pool in submerged-arc welding. *Avtomatich. Svarka*, **5**, 24–27.
4. Kuzmenko, V.G. (1998) Evaluation of the role of slags in different zones of submerged-arc weld pool. *Ibid*., **12**, 11–21.
5. Kuzmenko, V.G. (1985) Influence of slag on quality of weld surface formation. *Ibid*., **2**, 34–38.
6. Esin, O.A., Geld, P.V. (1966) *Physical chemistry of pyrometallurgical processes*. Moscow: Metallurgiya.
7. Vatolin, N.A., Pastukhov, E.A. (1980) *Diffraction investigations of high-temperature melt structure*. Moscow: Nauka.
8. Sokolsky, V.E., Kazimirov, V.P., Kuzmenko, V.G. (2000) Model of structure of oxide-fluoride melts on the base of close packing of oxygen atoms. *Problemy Spets. Elektrometallurgii*, **4**, 63–73.
9. Sokolsky, V.E., Galinich, V.I., Kazimirov, V.P. et al. (1991) Basicity of molten fluxes and possibility of its experimental determination. *Avtomatich. Svarka*, **5**, 35–37.
10. Kuzmenko, V.G., Galinich, V.I., Tokarev, V.S. et al. (1999) Study of properties of slag melts as applied to selection of welding fluxes composition. Part 1. Composition. *Ibid*., **11**, 38–48.
11. Sokolsky, V.E., Kazimirov, V.P., Kuzmenko, V.G. et al. (1999) Valence-structure state of ions and properties of welding fluxes. *Izv. Vuzov, Chyorn. Metallurgiya*, **5**, 3–6.
12. Sokolsky, V.E., Galinich, V.I., Kazimirov, V.P. et al. (1993) Peculiarities of structure of high-siliceous and high-alumina slag systems (of welding fluxes). *Rasplavy*, **6**, 18–20.
13. Toporishchev, G.A. (1983) Current concepts of the structure of molten slags. In: *Abstr. of pap. of 5th All-Union Conf. on Structure and Properties of Metallic and Slag Melts*. Part 3. Investigation of slag melts. Sverdlovsk: UNTs AN SSSR.
14. Sokolsky, V.E., Kazimirov, V.P., Shovsky, V.A. et al. (1995) X-ray method for determination of basicity of multicomponent melts of oxide-fluoride systems. *Zhurnal Prikladn. Khimii*, **11**, 1770–1774.
15. Liu, S., Olson, L. (1986) The role of inclusions in controlling HSLA steel weld microstructures. *Welding J*., June, 139–149.
16. Homma, H., Ohkita, S., Matsuda, S. et al. (1987) Improvement of HAZ toughness in HSLA steel by introducing finely dispersed Ti-oxide. *Ibid*., **10**, 301–309.
17. Cole, W., Colvin, P. (1971) Submerged-arc welding of higher tensile steels. *Met. Constr.*, **4**, 131–135.
18. North, T.N., Bell, H.B., Koukabi, A. et al. (1979) Notch toughness of low oxygen content submerged arc deposits. *Ibid*., **12**, 343–354.
19. Podgaetsky, V.V., Parfesso, G.I. (1991) On the problem of acicular ferrite nucleation in welds. *Avtomatich. Svarka*, **10**, 10–13.
20. Tokarev, V.S. (1991) Influence of non-metallic inclusions on microstructure of welds, produced with fluxes AN-60, AN-65 and AN-67-A. *Ibid*., **12**, 31–36.
21. Kuzmenko, V.G. (1992) Determination of temperature range of melting of welding fluxes in conformity with the data of its electrothermal analysis. *Ibid*., **9**, 34–38, 41.

SYSTEM OF DIAGNOSTICS OF ELECTRON BEAM IN INSTALLATIONS FOR ELECTRON BEAM WELDING

K.S. AKOPIANTS, O.K. NAZARENKO, V.V. GUMOVSKY and **V.P. CHERNYAKIN**
The E.O. Paton Electric Welding Institute, NASU, Kyiv, Ukraine

System provides longitudinal image of beam with a distribution of a power density. A focus position with ± 1 mm accuracy, minimum radius, maximum density of current, angle of convergence are determined. Conclusion is given about the gun cathode serviceability. Using this system the current of a magnetic deflecting lens with ± 0.5–0.7 % accuracy, required for beam focusing at a required distance to the workpiece, is determined.

Key words: *electron beam welding, reproducibility of welds, beam diagnostics, focus position, minimum radius of beam, power distribution, method of «plate edge», application in installations, measurement error*

Introduction. In most industrial installations for EBW the reproducibility of welds is provided by control of main parameters of the process, such as beam current, current of a magnetic focusing lens, gun-to-workpiece working distance, accelerating voltage and welding speed. The cathode service life is judged from the total time of its operation. However, space-energy parameters, beam parameters (position of focus relative to workpiece surface, minimum diameter, angle of convergence, maximum density of current and its distribution in beam) are not controlled before welding.

In [1, 2] the application of a wire rotating probe for determining the electron beam geometry is described. Structure of beam, contour and position of focus are set more precisely using a sensor with radially-located slots [3] or, like in a system of beam diagnostics DIABEAM [4], the plates with a hole of a small diameter (0.1 mm). To define the beam shape in a longitudinal direction using these systems it is necessary to move the sensor along the beam axis that makes the work of the welding operator difficult. The allowable power of electron beam examined is limited by several kilowatts due to a thermal failure of the sensors.

At the E.O. Paton Electric Welding Institute a computerized system of diagnostics of an electron beam, designed for furnishing the updated EBW installations with an electron beam power up to 100 kW, has been developed taking into account the demands of industry [5]. The system is equipped with a friendly screen interface which makes its use easier.

Principle of system operation. The device of diagnostics is arranged in a specially-designed place of a welding chamber (at some distance from workpiece being welded). Before the operation beginning the electron beam is moved in the position above the sensor and target (Figure 1, see insert). Diagnostics of the beam is performed using a «plate edge» method [6]. The electron beam is deflected to a target for the most time and only short-timely to the opposite direction. Here, the beam intersects a sensor edge, connected with «earth» via the leakage resistance. A pulsed current is passing in the sensor, where the current density in a transverse section of beam is calculated by the curvature of the pulse increment front. The pulse is normed by a matching amplifier and then transferred to the computer through a quick-response analog-digit converter (ADC).

Measurements are made at current change in a focusing lens. As a result of the computer processing of the obtained data files, a space distribution of power in beam, position of focus, minimum radius and others are calculated. The proper calculations are made at the assumption that the electron beam has an axial symmetry, completely true for welding guns, which use disc or rod cathodes with a circular symmetry. If the cathode, manufactured from wire or strip is used in the electron gun, then the axial symmetry in the beam can be violated and the accuracy in measurements will be decreased.

Procedure of measurements. Let us consider the peculiarities of system operation and procedures of measurements.

To pass from time of a pulse increment to units of length, a procedure of calibration of beam movement velocity relative to the sensor is provided. For this purpose, there is a reference element in the sensor design, having a known size in the direction of beam movement. When the beam intersects this element a current pulse duration is measured. Hence, the beam movement velocity is determined:

$$v = \frac{s}{\tau},$$

where s is the element length; τ is the pulse duration.

Calibration of velocity is realized on two extreme distances of sensor from the gun: minimum and maximum. Later on, at sensor arrangement into another intermediate position with respect to gun the velocity of beam movement relative to the sensor is calculated automatically according to a linear relationship using two calibrating values.

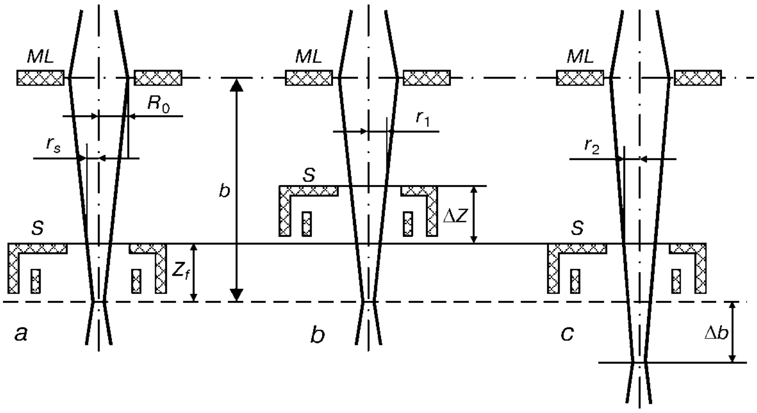

Figure 2. Scheme of obtaining data for construction of the beam profile with a distribution of current density in a longitudinal axial section R, Z: a — initial position of a sensor; b — shifting of sensor for ΔZ in a conventional method of plotting relationship $R(Z)$; c — change in beam focusing by Δb using a suggested method of plotting relationship $R(Z)$ (ML — middle plane of a magnetic focusing lens)

The principle of construction of beam profile in a longitudinal axial section R, Z will be explained using Figure 2. Figure 2, a shows an initial state S of a measuring plate relative to a beam focus, located at the distance b from a middle plane of the focusing lens. To investigate the beam parameters along its axis the sensor is displaced with a pitch ΔZ and the measurements are made on each pitch (Figure 2, b) [1–4]. We have suggested to study beam by a pitch change in beam focusing per value Δb at unchanged initial position of the measuring plate (Figure 2, c).

In initial state (Figure 2, a) the beam has a radius r_s and angle of convergence α in a sensor plate:

$$\alpha = \frac{R_0}{b}; \quad r_s = Z_f\,\alpha = Z_f\,\frac{R_0}{b},$$

where R_0 is the radius of beam in a middle plane of the lens; Z_f is the distance from sensor plane to a focus.

In case of changing sensor position by value ΔZ the beam will have a radius r_1 in this place (Figure 2, b):

$$r_1 = r_s + \Delta Z\alpha = Z_f\,\frac{R_0}{b} + \Delta Z\frac{R_0}{b} = \frac{Z_fR_0 + \Delta ZR_0}{b}. \quad (1)$$

If to change the beam focusing by value Δb, and to remain the sensor previous position (Figure 2, c), then beam radius will be r_2 in the sensor plane; here, the angle of convergence α_2 will change a little:

$$\alpha_2 = \frac{R_o}{b + \Delta b}; \quad r_2 = (Z_f + \Delta b)\alpha_2 = \frac{Z_fR_0 + \Delta bR_0}{b + \Delta b}. \quad (2)$$

Let us compare the expressions (1) and (2). It is evident, that if in denominator of expression (2) $\Delta b << b$, and $\Delta Z = \Delta b$, then $r_1 \approx r_2$ and, instead of varying the sensor position, it is possible to change the beam focusing. Ratio $\Delta b << b$ is completely valid for a case of beam investigation near its focus. To evaluate the accuracy of determination of beam configuration at a large distance from the plane of focus location the expression (2) is taking the logarithm and then differentiated:

$$\ln r = \ln(Z_fR_0 + \Delta bR_0) - \ln(b + \Delta b);$$

$$\Delta r/r \approx -\Delta b/b.$$

It follows from the last formula that if the beam radius is calculated in the area located nearer to the gun than the sensor (in our case this corresponds to the decrease in a degree of beam focusing, i.e. focus is lowered), distance b is increased and here $\Delta b_0 > 0$ (Figure 2, c), then the much lower values of the radius (error $\Delta r < 0$) are obtained. If the radius is calculated for the distances which are larger than those to the sensor (in our scheme of measurements this corresponds to the fact that the focus was lifted, i.e. b was decreased and $\Delta b < 0$), then the values of radius are overestimated ($\Delta r > 0$). To avoid errors in determination of $r(Z)$, the values r should be multiplied by a correction factor, accounting for sign Δb:

$$k = \left(1 + \frac{\Delta b}{b_s}\right),$$

where b_s is the distance from a middle plane of lens to the sensor. This correction is provided in algorithm of the diagnostics system operation.

To find the value Δb at changing the magnetic lens current by ΔI_f two measurements are made. During the first measurement the current of the focusing lens I_{f1}, corresponding to «acute» beam focusing in sensor at its close position z_{s1} relative the gun is determined. During the second measurement the current of lens I_{f2} at the far position Z_{s2} of the sensor is determined in the similar way. Coefficient of the magnetic lens sensitivity is calculated:

$$\frac{\partial b}{\partial I_f} = \frac{Z_{s1} - Z_{s2}}{I_{f1} - I_{f2}}.$$

It should be noted that $\partial b/\partial I_f < 0$, as with decrease in the lens current the distance b is increased.

Value $\partial b/\partial I_f$ is determined, firstly, by the lens properties (number of turns, design of magnetic core and accelerating voltage). The $\partial b/\partial I_f$ does not depend upon the sizes of electron beam, in particular on R_0 (in the first approximation, if not to take into account the aberration).

In next calculations the current coordinate Z is determined by expression

$$Z = Z_s + \frac{\partial b}{\partial I_f}\Delta I_f.$$

Distribution of current density in transverse sections of beam is calculated by numerical methods as follows. All the beam section is divided by N rings. Within each ring the current density J_N is taken constant. System of N linear algebraic equations for finding unknown J_N can be written in a matrix form:

$$\boldsymbol{SJ} = \boldsymbol{A},$$

where

$$\boldsymbol{S} = \begin{pmatrix} S_{11} & S_{12} \ldots S_{1N} \\ S_{21} & S_{22} \ldots S_{2N} \\ \ldots. & \ldots\ldots\ldots\ldots \\ S_{N1} & S_{N2} \ldots S_{NN} \end{pmatrix}$$

is the square matrix of $N \times N$ size, its terms are proportional to the area of regions of rings, to which different values of current density correspond;

$$\boldsymbol{J} = \begin{pmatrix} J_1 \\ J_2 \\ \ldots. \\ J_N \end{pmatrix}$$

is the vector of N-order, its components are the unknown values of current density for each ring;

$$\boldsymbol{A} = \begin{pmatrix} A_1 \\ A_2 \\ \ldots. \\ A_N \end{pmatrix}$$

is also the vector of N-order, its components are the ordinates of the pulse front.

For each separate measurement it is possible to display the image of the pulse front on the screen (Figure 3, *left half*, see insert). From its appearance it is possible to judge preliminary about the beam radius and the measurement process proceeding. Steepness of the pulse front is inversely proportional to the beam radius. Smooth front pulse, without bursts, testify to the absence of disturbances in measurement or breaks in the operation of ADC during the recording of pulses. The pulse duration in time is recalculated into units of length using multiplying by beam movement velocity. The beam center is determined as abscissa of the pulse front at the half of its amplitude.

Using the calculated values J_N a graph of distribution of current density for each transverse section of beam is plotted (Figure 3, *right half*, see insert). Distribution at the highest current density in axis $J = J_{\max}$ corresponds to a sharp focusing of beam in the sensor; value $J_{\max}$ is derived as a characteristic parameter of the beam (Figures 4 and 5, see insert). As is mentioned in [7], the accuracy of calculation of current density distribution depends on the error of measurements of pulse front coordinates. Therefore in calculations the procedure of a static smoothing of data measurements is provided. The width of a smoothing window was selected equal to x_{f}/N, where $x_{\text{f}} = v\tau_{\text{f}}$ (τ_{f} — duration of the pulse front).

For each distribution the averaged effective beam radius R is also calculated on the assumption that the distribution can be approximated by the Gauss law [3]. Within this radius 63 % of all the beam current is passing. It can be stated that this radius is calculated from the pulse front as follows:

$$R = [x(A_1 = 0.8) - x(A_2 = 0.2)]0.84,$$

where $A_1 = 0.8$ and $A_2 = 0.2$ are the ordinates of the pulse front equal to 0.8 and 0.2 of amplitude, respectively.

From all the distributions (for the given series of measurements) the least effective radius of beam $R_{\min}$ is selected which corresponds to a sharp beam focusing in the sensor. This value is also displayed in an information line (Figures 4 and 5, see insert).

The obtained distributions of current density in transverse sections of beam (at different distances Z) are used for construction of the beam profile with a space distribution of the current density in a longitudinal axial section R, Z (Figure 4, see insert). This image of the area in different colors indicates the distribution of current density in the beam: yellow color indicates the region of 75–100 % maximum current density $J_{\max}$, red color corresponds to 50–75 %, white color shows a region of 25–50 %, dark blue color — lower than 10 % and blue color — the beam contour. Grey color in this image indicates the position of workpiece relative to the gun (its transverse section), which is preset by the operator.

Results of measurement. When welding operator is looking at the image, he observes, first of all, how the beam focus, zone of its highest density of power (most «hot» place) at a preset current of the focusing lens are located with respect to the surface and thickness of the workpiece and how to change the focusing to arrange the minimum section of the beam to the required level relative to the workpiece surface.

The following sizes are presented in the beam image: in horizontal axis the distance from the lower edge of electron gun in millimeters is indicated (axis Z), in vertical axis the radius of beam in millimeters is indicated (axis R).

The information lines reflect the values preset by the operator: current beam I_b, current of focusing lens I_f, working distance WD from the gun edge to the workpiece surface and thickness TH. Here, the values are also given which are calculated by the system of beam diagnostics: distance from gun edge to beam focus $Z_{\min}$, effective minimum radius of beam in focus $R_{\min}$, maximum density of current $J_{\max}$, angle of beam convergence (a half). The position of focus $Z_{\min}$ is determined with error ± 1 mm in the area of working distances WD = 100–200 mm.

In the same window there is a graph of relationship $R(Z)$: variation of effective beam radius along the axis for a definite focusing (Figure 4, *lower half*, see insert).

The system of diagnostics provides rather visually any changes in quality of the electron beam. For quantitative imaging of these changes the system of diagnostics makes it possible to compare the results of two measurements, for example, for electron beam in initial state (gun with new cathode) and in some other direction (Figure 5, see insert). In the lower half of Figure 5 the space distribution of current density is given and parameters of beam for cathode operated for long time in the gun are indicated. As compared with reference results (Figure 5, *upper half*) the beam was changed: the minimum effective radius $R_{\min}$ was increased, maximum current density $J_{\max}$ was decreased; there is no zone in the distribution of power density amounting to 75–100 % of initial maximum density.

In each definite industrial installation for EBW the conclusion about preserving the gun serviceability or necessity in the cathode replacement is defined by the technological conditions for EBW of a definite workpiece. The technological chart should include the allowable deviations in position of beam focus $Z_{\min}$, minimum beam radius $R_{\min}$, angle of convergence α, current density $J_{\max}$. In case of a very large deviation of any parameter of the beam, the system of diagnostics issues conclusion about a poor condition of the gun cathode and its replacement.

The estimated error in determination of the current of a magnetic focusing lens required for beam focusing with a half of angle of convergence α at a preset working distance can be written in the following form:

$$\frac{\Delta I_f}{I_{f\,\min}} = \frac{R_{\min}}{\alpha I_f}\frac{\partial I_f}{\partial b}\sqrt{2\left(\frac{\Delta R}{R}\right)},$$

where $\frac{\Delta R}{R} = \frac{\Delta\tau}{\tau} + \frac{\Delta v}{v}$ = 4 % is the error in determination of beam radius; $\Delta\tau/\tau_{\mathrm{f}} = 1/(f_{\mathrm{conv}}\tau_{\mathrm{f}})$ = 2 % (f_{conv} is the frequency of conversion using ADC, which determines the accuracy in pulse duration setting). Calculated and experimentally-obtained value of the required current of the magnetic lens is 0.5–0.7 %.

Technical characteristic of the system

Pulse amplitude of deflection current, A	5
Frequency of deflecting pulses, Hz	3
Duration of deflecting pulse, μs	30–50
Distance of sensor to the axis of deflected beam, mm	20
Averaged distance from the lower edge of gun to sensor, mm	150
Mean rate of beam movement relative to sensor, mm	1000
Frequency of conversion by ADC, MHz	40
Accuracy of conversion, category	8
Range of power of beams examined, kW	1–100
Accuracy of determination of beam focus position, %	0.5–0.7

Thus, the system of diagnostics represents a self-contained software-hardware complex made on the base of industrial or personal computer. It is not difficult to build this system in any computerized welding installation.

1. Sanderson, A. (1968) Electron beam delineation and penetration. *Welding J.*, **10**, 509–523.
2. Nazarenko, O.K., Lokshin, V.E., Akopiants, K.S. (1970) Measuring of parameters of powerful electron beam by rotary probe method. *Elektron. Obrab. Materialov*, **1**, 87–90.
3. Elmer, J.W., Teruya, A.T. (2001) An enhanced Faraday cup for rapid determination of power density distribution in electron beams. *Welding J.*, **12**, 288–295.
4. Dilthey, U., Weiser, J. (1995) Study of the «Tool» electron beam. Part 1. Comparison between the Arata beam test and beam measurement. *Welding and Cutting*, **5**, 82–84.
5. Paton, B.E. (2001) Modern electron beam technologies of the E.O. Paton Electric Welding Institute of the NAS of Ukraine. *The Paton Welding J.*, **2**, 2–7.
6. Zinchenko, N.S. (1961) *Lectures on electron optics*. Kharkiv: KhGU.
7. Lankin, Yu.N. (1984) Accuracy of experimental evaluation of current density distribution in section of electron beam. *Avtomatich. Svarka*, **4**, 69–70.

PROCEDURE AND PARAMETERS OF A-TIG WELDING OF STRUCTURAL STEELS

D.R. BAJIC[1], **G.M. MELNICHUK**[2], **A.F. LUPAN**[2] and **M.M. SAVITSKY**[2]
[1]Technical University, Podgorica, Montenegro
[2]The E.O. Paton Electric Welding Institute, NASU, Kyiv, Ukraine

Relationship between parameters of tungsten-electrode argon-arc welding using activators (A-TIG welding) and weld parameters, electrode life and stability of the process of formation of a welded joint in welding structural steels is considered.

Key words: *argon-arc welding, activating flux, inert gases, welding parameters, tungsten electrode life, weld formation, welded joints*

There are many publications now which describe phenomenon of increase in the penetrating power of the arc in A-TIG welding and suggest several hypotheses for explaining it [1]. As follows from this study, no unified opinion of this matter exists at present and most probably will not exist in the near future. At the same time, manufacturers interested in using the advanced welding method need information about its technical characteristics.

This article contains experimental data on the method of welding using activating fluxes and relationship between welding conditions and weld parameters.

Addition of electrically negative and surface-active elements to the arc causes it to contract. Current density in the anode spot and arc pressure on metal increase more than twice in this case [2]. As a result, diameter of the heating spot decreases almost 2 times and surface tension of liquid metal in the weld pool is reduced [2, 3]. This provides a considerable improvement in the penetrating power of the arc and heat transfer to the solid metal, and leads to an increase of 2–3 times in its penetration.

The effect of increase in the penetrating power of the arc by activating fluxes was used to develop technologies for welding parts of different grades of structural steels, such as martensitic, maraging, bainitic, pearlitic, ferritic and austenitic. Activating fluxes and related welding technologies developed by the E.O. Paton Electric Welding Institute are applied to advantage for the manufacture of pressure vessels, aircraft landing gear components, for welding of aerospace engine bodies, making circumferential position and roll butt welded joints in piping for heat and nuclear power generation, etc.

A-TIG welding can be performed in the atmosphere of argon, helium and other inert gases or their mixtures. For example, helium has a higher ionisation potential (24.5 eV) at the same welding current, which allows the penetrating power of the arc to be increased by approximately 20–25 % (Figure 1). In this case it is possible to weld steel up to 12 mm thick in a single pass without groove preparation. Penetration of steel up to 20 mm thick is done on two sides or with groove preparation. In all the cases the flux is deposited by one of the methods described in [4] in a thin (0.1 mm) uniform layer on the surface of a workpiece near the weld edges in an amount of about 1–2 g per running metre of the weld length. However, with this amount it does not perform a shielding function. The weld pool is shielded using inert gases, while the flux functions here just to intensify oxidation-reduction processes occurring on the surface of the weld pool and periphery of the arc column, which are rather slack in the inert atmosphere. This probably decreases surface tension of liquid metal and increases density of energy of the arc with no increase in its power. Taken together, all these factors lead to a deeper immersion of the arc into metal and formation of narrow welds with deep penetration. As values of electric parameters of the arc between the tungsten cathode and steel anode do not exceed the limits specified for TIG welding, welding of steels using activating fluxes can be performed with the equipment and under conditions applied for TIG welding. However, while selecting parameters for A-TIG welding, one should take into account that the dependence of shape and size of the weld upon the welding current in the said

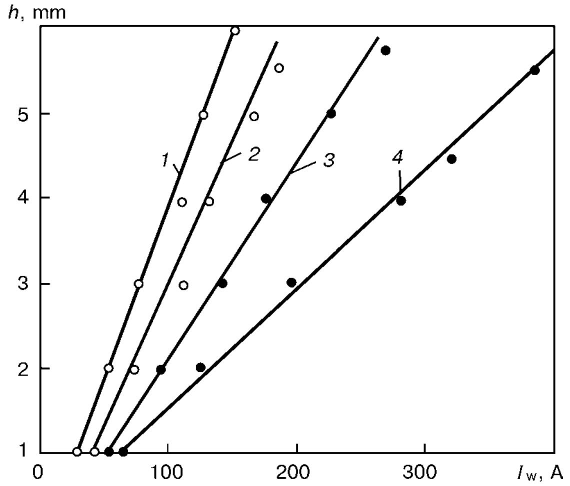

Figure 1. Penetration depth *h* on steel in welding in helium (*1*, *3*) and argon (*2*, *4*) with (*1*, *2*) and without (*3*, *4*) an activating flux

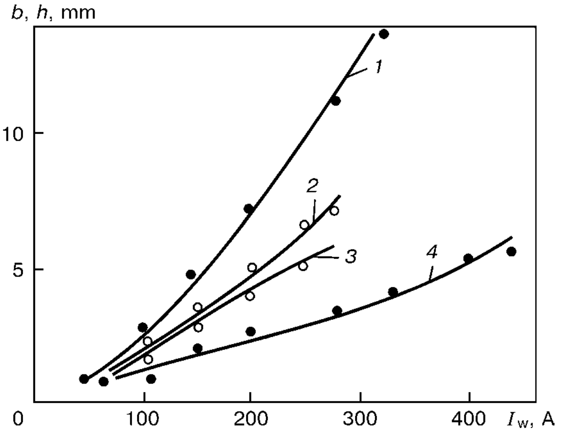

Figure 2. Dependence of weld width b (*1, 2*) and penetration depth h (*3, 4*) upon the current in welding of low-alloy steel with (*2, 3*) and without (*1, 4*) an activating flux

processes is of a different character (Figure 2). Variations in the welding current make this difference especially pronounced. In the first case this causes a more intensive increase in the weld width, and in the second — the penetration depth.

In one-sided welding with complete penetration, performed in flat position, it is very difficult to provide reinforcement on both sides of the weld, as metal is depressed under the effect of the arc pressure and by gravity. A recess the surface of which is located below the surface of the parts joined is formed as a rule on the face of the weld. To eliminate this drawback, it is advisable to make the second pass using filler wire and electrode weaving. In welding steels with low thermal conductivity and high thermal expansion coefficient, to produce the required reinforcement it is permitted to use the self-pressing effect instead of a filler wire. This effect is provided by reheating the weld following a certain thermal cycle. By combining parameters of thermal and deformation cycles, it is possible to increase compressive stresses in the welded joint, thus inducing plastic strains which lead to formation of the weld reinforcement with no use of filler wire.

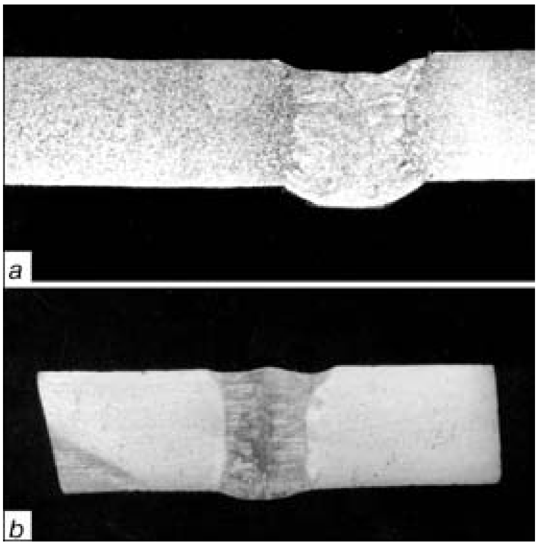

Figure 3. Transverse macrosections of welded joints in low- (*a*) and high-alloy (*b*) steel produced by welding in argon using an activating flux

Thermal-physical properties of steels, and thermal conductivity in particular, which are known to depend upon chemical composition, have a considerable effect on welding conditions. This applies primarily to the welding current. For example, in welding carbon steel 20 with thickness of 6 mm at a speed of 100 mm/min the welding current should be 175 A to ensure complete penetration. In the case of welding high-alloy steel 12Kh18N10T of the same thickness and at the same speed the welding current should be 155 A, i.e. the value of the current should be decreased by 18–20 %. Therefore, the complete penetration being achieved, the volume of metal heated to its melting point is larger in the first case (Figure 3).

Activating fluxes for welding steels are a mechanical mixture of finely dispersed powders (mostly metal oxides or fluorides), as well as components ensuring microalloying and modification of the weld metal. The most common method for application of fluxes is to deposit them on the surface of the weld edges in the form of a paste using a crayon or paint brush. For this the highly volatile solvents are added to the activating flux. Then a homogeneous paste with density and viscosity corresponding to those of a house paint is produced by mixing. In this condition the flux forms a uniform coating on the surface of metal near the weld edges. It melts during welding and interacts with liquid metal to change the composition of vapours penetrating into the inter-electrode gap [3].

The authors developed, made and industrially tested special reusable crayons, with the help of which the flux paste is applied to the surface of steel in a thin uniform layer of a preset width. The PWI developed also special flux pencils made from a mixture of a low-melting point binder and an activating flux by melting or pressing. The flux is deposited with the pencil on the surface which may be rough after sandblasting or preheated by tack welding to 40–50 °C.

In the 1980s, in collaboration with associates of the Tsentroenergomontazh Trust Welding Laboratory (Moscow), the authors developed the composition of the flux and its storage and utilisation technologies using sprayers. They were intended for assembly of power unit pipings at the Kursk and Smolensk nuclear power stations [5]. The experience showed that fluxes could be applied in the form of aerosols only in open air or in large shops with intensive mechanical ventilation. When performed in workshops or welding boxes, this causes dusting of the work space, as a large amount of the flux is sprayed into the atmosphere. If a sprayer is brought closer to the joint, this will cause the flux to penetrate into the gap, and during welding it may lead to formation of slag inclusions and pores in the weld metal.

Different modifications of activating fluxes intended for welding steels contain refractory oxides, which require a certain amount of heat to be supplied to melt them. Therefore, welding parameters may depend upon the thickness of an activating flux layer deposited on the weld edges. To estimate this dependence, the activating flux was deposited on the edges in layers of different thickness, and then welding was carried out. Thickness of such a layer was controlled using special gauges, and during the experiments it was varied by 0.025 mm from 0.05 to 0.5 mm. It was established that in welding at a current of 300 A a change in thickness of the activating flux layer from 0.05 to 0.3 mm hardly has any effect on the steel penetration depth. As thickness of the layer was increased (to more than 0.3 mm), to provide the same penetration depth the welding current had to be increased by 10–15 %, which was associated with growth of heat consumption to melt the excessive flux.

Optimal thickness of the activating flux layer on the edge surfaces is normally not in excess of 0.1–0.2 mm, the layer width being approximately 8–10 mm. In this case the flux consumption is about 1 g per running metre of the weld length.

Consistency of metal penetration and weld formation in welding both with and without the activating fluxes depends upon the life of the tungsten electrode. In the case of fast wear and destruction of its tip the arc features an unstable burning and «wanders» over the surface of the cathode and anode, which leads to lack of penetration, lack of fusion and formation of tungsten inclusions in the weld metal. Therefore, it was important to determine how the flux containing such strong oxidisers as fluorine or oxygen might affect the life of the tungsten cathode in a short welding arc. For this purpose the continuous weld with a length of 3 running metres was made under the following conditions: v_w = 100 mm/min, I_w = 200 A, U_a = 9.8 V and cathode to anode distance — 1 mm. The experiment was conducted on four samples of stainless steel Kh18N10T and steel 20, the steel Kh18N10T samples being welded with and without the activating flux.

Appearances of electrodes before and after welding are shown in Figure 4. As seen from the Figure, there is some difference in the character of wear of the electrode tip in welding steel with and without the activating flux. However, no destruction is seen in the blunted tip, and the penetration stability does not change.

One of the important characteristics of stability of the process of metal melting and quality weld formation is a constant arc voltage at the tungsten cathode. In mechanised welding it is regulated using different devices, whereas in the case of manual welding it is much more difficult to ensure the stable process. Therefore, it was important to determine the permissible limits of fluctuation of the arc voltage within which there would be no substantial change in the weld formation. Relationship between the arc voltage and quality of the weld formation at a constant current, as well as between the current and voltage, was studied by performing a series of experiments. In the first case A-TIG welding was performed in the flat position on an inclined plane and the arc length was changed by 2 mm. Welding was carried out with complete penetration, the current was kept constant (I_w = 120 A) during the experiments, while the arc voltage was 8.2 V at the beginning of welding and 11.4 V at the end of welding.

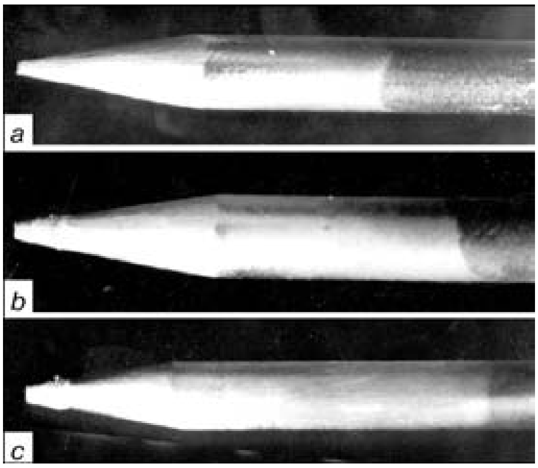

Figure 4. Shape of the tungsten electrode tip after grinding (*a*) and welding in argon with (*b*) and without (*c*) an activating flux

As seen from Figure 5, geometric sizes of the welds changed to some extent with increase in the arc voltage. First of all, this concerned the weld width and value of the back reinforcement, although a sufficient penetration of metal was observed over the entire weld length. It can be concluded that a change (increase) of approximately 2 V in the arc voltage in welding using the activating flux has an insignificant effect on penetration.

However, to ensure the consistent quality formation of the weld over its entire length, in making the first category welds, the arc voltage should be maintained constant automatically using regulators. They should provide a high accuracy of maintaining the arc voltage. Therefore, it was important to know to what extent the activating fluxes might affect their performance.

In this connection, several experiments were conducted to determine dependence of the arc voltage upon the current at different distances between the electrode and base metal in TIG and A-TIG welding.

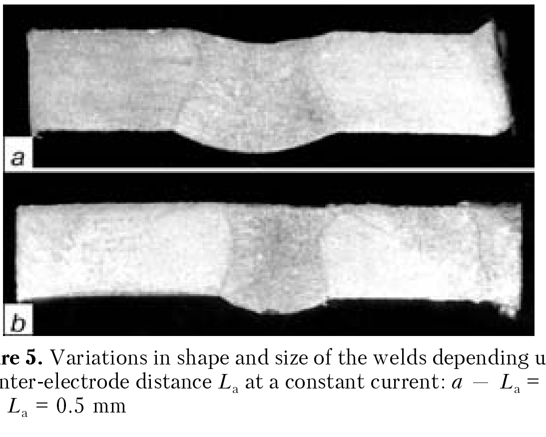

Figure 5. Variations in shape and size of the welds depending upon the inter-electrode distance L_a at a constant current: *a* — L_a = 2.5; *b* — L_a = 0.5 mm

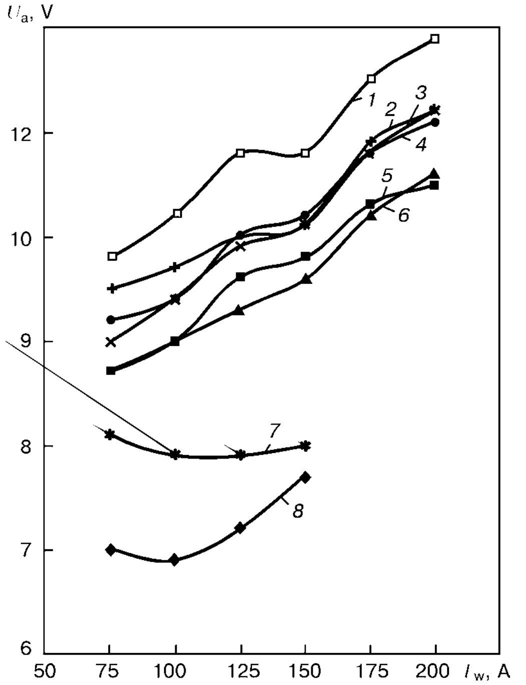

Figure 6. Dependence of the arc voltage upon the current at different inter-electrode distance: L_a = 2.0 (*1, 3*), 1.4 (*2*), 1.0 (*4, 5*), 1.5 (*6*) and 0.5 (*7, 8*) mm

To exclude the effect by the weld pool mass and surface tension on the reverse side, welding was carried out with an incomplete metal penetration. With a set distance of 0.5 mm from the sample surface to the electrode, as the current was increased the arc voltage during the TIG process first decreased and then increased. It is likely that this is related to the rise of liquid metal in the weld pool and absence of a crater. As the current was further increased, the arc pressure on liquid metal also increased to form a crater in the weld pool, which led to some increase in the arc voltage.

In A-TIG welding the crater was formed immediately after the arc reached its working conditions, and the above noted variations in values of the arc voltage were no longer observed. Increase in the inter-electrode distance and use of the same welding current resulted in increase in the arc voltage, growth in its power and pressure on metal both in TIG and A-TIG welding. In the case of A-TIG welding the arc voltage was always 0.25–0.3 V higher than in TIG welding (Figure 6). This is probably caused by contraction of the arc and reduction in conductivity of the peripheral regions of the arc column under the effect of the activating flux. It should be noted that the character of variations in the arc voltage in the cases compared remains unchanged. This allows the existing equipment (especially regulators of welding parameters) to be used with no special redesigning.

Therefore, application of the activating flux for TIG welding allows the penetration of metal up to 12 mm thick in one-sided welding and up to 20 mm thick in two-sided welding to be increased without any change in the welding arc conditions using the existing equipment. In addition, good quality of the weld metal and its strength equal to that of the base metal are provided. The new welding method is widely applied in aircraft and nuclear power engineering, as well as in other industries.

1. Savitsky, M.M., Kushnirenko, B.N., Olejnik, O.I. (1999) Peculiarities of tungsten-arc welding with activating fluxes (A-TIG process). *Avtomatich. Svarka*, **12**, 20–28.
2. Savitsky, M.M., Gvozdetsky, V.S., Skrypnik, V.I. et al. (1979) Current density in anode spot during welding of conventional and refined steels. *Ibid.*, **7**, 17–20.
3. Savitsky, M.M., Leskov, G.I. (1980) Mechanism of influence of electronegative elements on penetrating power of the arc with tungsten cathode. *Ibid.*, **9**, 17–22.
4. Savitsky, M.M., Lupan, A.F., Melnichuk, G.M. et al. (2000) Methods for application of activators in TIG welding of steels. *The Paton Welding J.*, **3**, 52–53.
5. Stankevich, I.Ya., Dmitriev, V.I., Korida, V.L. et al. (1982) Application of activating fluxes in automatic welding of nuclear power plant pipings. *Energetich. Stroitelstvo*, **10**, 19–20.

HYBRID CO_2-LASER AND CO_2 CONSUMABLE-ARC WELDING

V.D. SHELYAGIN, V.Yu. KHASKIN, V.P. GARASHCHUK, A.V. SIORA, A.V. BERNATSKY and **A.V. SAKHARNOV**
The E.O. Paton Electric Welding Institute, NASU, Kyiv, Ukraine

Technological research on laser and consumable-arc hybrid welding at process speeds of 15–300 m/h is described. Application of the hybrid process at fixed power of laser radiation is rational up to a certain thickness of welded metal, above which the penetration depth does not increase, despite lowering of welding speed.

Key words: *hybrid welding, laser, electric arc, stabilisation, penetration depth, weld thickness, welding modes*

Over the last years a lot of works have been published on combining various heat sources for welding metals and alloys. For instance, researchers became interested in the effect of combining the laser radiation with the arc plasma [1] or HF heat source [2]. The advantages of laser-arc hybrid welding are the ability of partial replacement of laser radiation by the power of the arc source with preservation of weld geometry, close to laser welds; transformation of the welding thermal cycle, lowering the susceptibility to formation of hardening structures in weld metal and HAZ, etc. The first of the above advantages is particularly interesting for industrial introduction of laser-arc welding, as it may promote reduction of capital cost for purchase of equipment (considering its comparatively low cost for arc welding).

Technological research of laser hybrid processes was conducted. Combining laser radiation with HF heating source [2] was studied, as well as laser-arc welding, using tungsten-electrode arc. However, as shown by practical work, in order to produce optimal geometry of the welds, it is necessary to use filler materials. Use of regular filler wire in laser welding requires additional consumption of the radiation power for wire melting. Consumable-electrode arc allows avoiding these costs (wire becomes an «active filler»). Experiments on studying the technological features of the hybrid of laser welding and CO_2 consumable-arc welding were conducted by the schematic, shown in Figure 1, using a welding manipulator, providing the welding speed v_w = 15–300 m/h. Processing CO_2-laser LT-104 was used as the radiation source [3]. Radiation power was varied in the range of 0.2 to 2.7 kW. Radiation was focused by a lens of potassium chloride single crystal (F = 300 mm). Samples were both solid plates and butts of steels 09G2S (wt.%: 0.09–0.1C; 1.5Mn; 0.4Si) and 3 (wt.%: 0.14–0.22C; 0.3–0.6Mn; Fe — balance; rimmed) 2 to 10 mm thick. In the case of δ = 2–10 mm, the butts were made with edge preparation (bevel of 15°, root face of 4 and 6 mm). Filler wire Sv-08G2S (d = = 0.8 mm) was fed at the speed of v_f = 200–450 m/h, angle of electrode inclination to the laser beam axis α = 25°, arc length L = 6–8 mm, arc current I = = 75–200 A.

The work consisted in studying the influence of laser radiation on arcing stability, quality of formation of the upper and lower beads of the weld, geometrical dimensions of the cast metal zone. At simultaneous action on the metal (see Figure 1), laser radiation stabilises arcing. The higher the welding

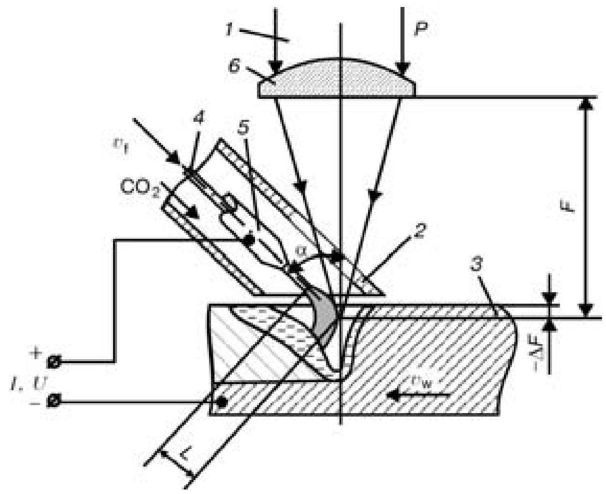

Figure 1. Schematic of conducting experiments on laser-arc hybrid welding: *1* — laser radiation of power P, kW; *2* — protective nozzle; *3* — sample; *4* — filler wire; *5* — copper current-conducting nozzle; *6* — focusing lens with focal distance F, mm; ΔF — focal point depth, mm; α — angle of inclination of the electrode to the laser beam axis, deg; L — arc length, mm

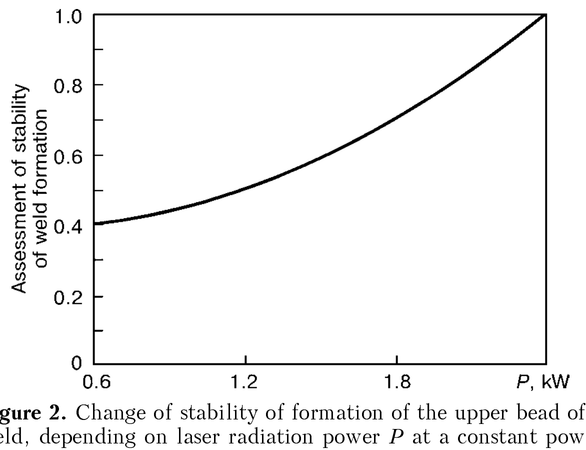

Figure 2. Change of stability of formation of the upper bead of a weld, depending on laser radiation power P at a constant power of the arc of 2.88 kW (v_w = 76 m/h)

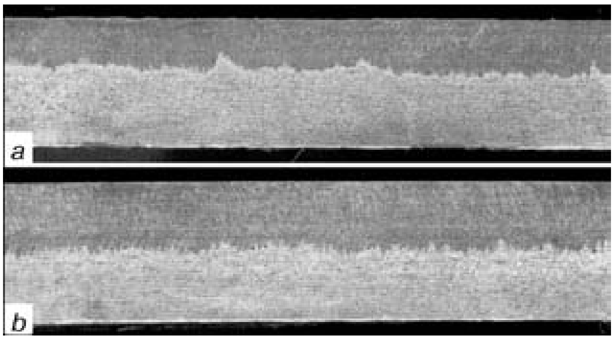

Figure 3. Macrostructures of axial longitudinal section of the deposits, made in a plate of steel 09G2S (δ = 10 mm) by laser (*a*) and hybrid (*b*) process with CO_2 shielding in the following modes: *a* — P = 2.5 kW, F = 300 mm, ΔF = −3 mm, v_w = 40 m/h; *b* — P = 2.5 kW, F = 300 mm, ΔF = −3 mm, v_w = 40 m/h, I = 100 A, U = 17 V, v_f = 260 m/h

speed, the greater should be the radiation power. For instance, at a constant welding speed of 15–50 m/h, a reliable stabilisation is achieved at radiation power of 0.2–0.3 kW, and at 120 m/h and higher at 2.5 kW and more. Arcing stabilisation is accompanied by arc voltage drop in the range of 2–5 V. In this case, the arc proper moves lower into the vapour-gas crater to a depth, commensurate with deepening of focus ΔF.

The studied hybrid process markedly changes the quality of formation of the upper bead, both in surfacing and butt welding. For better presentation, it was evaluated not to GOST 25616–83, but by a point scale, when a unity corresponded to the highest quality, at which weld formation was stable and regular, with a smooth transition to the base metal. The higher the degree of disturbance of the above properties, the less points, expressed as tens fractions, were used to estimate the quality. From Figure 2 it follows, that the quality of formation of the upper bead improves with the increase of laser radiation power at a constant speed of welding and power of electric arc.

Figure 3 shows the longitudinal macrosections of deposits, made by the processes of laser and hybrid welding. In the case of hybrid welding the line of the upper bead is more even, and the depth of the cast metal boundary is more uniform than in laser welding. However, the structure in the weld root in hybrid welding is more clearly defined than that in laser welding, which is indicative of a periodic process in melting. In laser welding the periodicity is less obvious. Measurement of weld microhardness showed, that with base metal hardness of HV 1490–1520 MPa, laser welds have the microhardness of HV 3110–3200, while the hybrid welds HV 2550–2690 MPa. This is indicative of a lower susceptibility to formation of hardening structures in the cast metal in hybrid laser-arc welding.

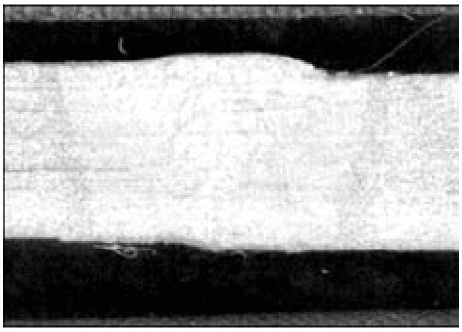

Figure 4. Macrostructure of a butt joint of 09G2S steel sheets (δ = = 6 mm), made by the hybrid laser-arc process (P = 2.5 kW, F = = 300 mm, ΔF = −2 mm, v_w = 40 m/h, I = 90 A, U = 26 V, v_f = = 210 m/h)

Figure 4 shows a transverse macrosection of a butt joint, made by hybrid welding with high-quality formation of the upper and lower beads. In butt welding it was found that compared to the laser welding process with filler wire for steels with $\delta > 5$ mm, 1 kW of power of the electric arc can replace 0.5 kW of laser radiation, while for steels with $\delta < 4$ mm this replacement is just one to one.

Figure 5 shows the dependencies of the total thickness of the weld [4] and penetration depth on welding speed (at constant powers of laser radiation and electric arc) for hybrid and laser welding. Experimental points were derived by averaging 4 to 6 measurements

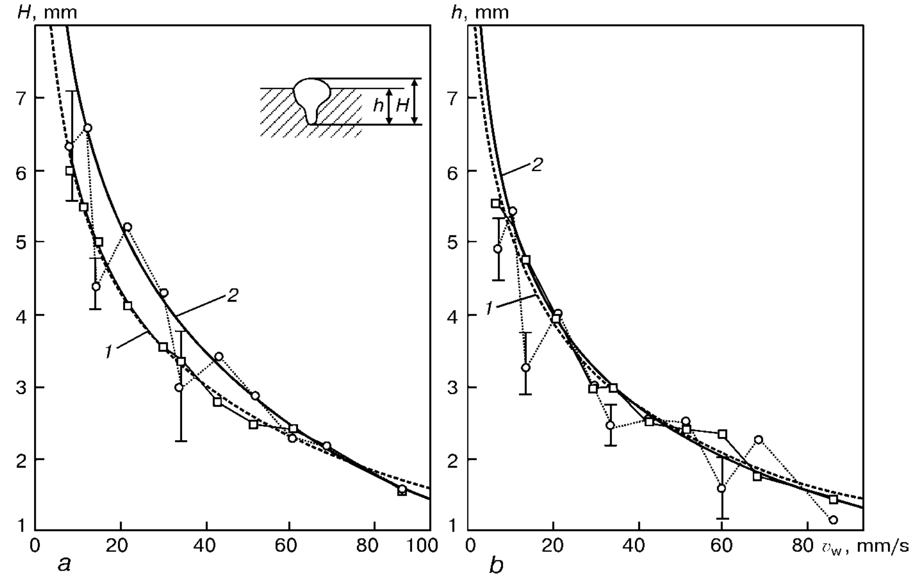

Figure 5. Dependence of the total weld thickness H (*a*) and penetration depth h (*b*) on welding speed v_w: *1* — laser welding; *2* — hybrid welding

in some sections of the weld. Scatter of experimental results is in the range of ±(6–8) %.

In laser welding the total thickness of the weld and penetration depth decrease gradually with the increase of welding speed (Figure 5, curve *1*). Measured experimental dependencies are approximated by analytical dependencies by the least squares method. For the total width of the weld, they are described by the relationship $H_{\mathrm{LW}} = -12.14 + 23.3v_{\mathrm{w}}^{-0.1164}$, for penetration depth $h_{\mathrm{LW}} = -7.93 + 18.95v_{\mathrm{w}}^{-0.1565}$.

In hybrid welding also a decrease of the total weld thickness and penetration depth is found with the increase of welding speed (Figure 5, curve *2*). However, individual experimental points markedly fall out of the monotonic dependence. They were eliminated from the approximation. Their analytical representation is as follows: for the total thickness of the weld $H_{\mathrm{HW}} = -45.49 + 59.02v_{\mathrm{w}}^{-0.0506}$; for penetration depth $h_{\mathrm{HW}} = -5.73 + 18.69v_{\mathrm{w}}^{-0.2153}$.

Both analytical dependencies and curves in Figure 5, *b* indicate, that the differences between the penetration depths in hybrid and laser welding are within measurement accuracy. Therefore, if we ignore the falling out experimental points, the penetrability is not essentially increased.

In order to determine the validity of deviation of experimental points, eliminated from approximation, standard values were calculated for them with confidence probability of 0.9. They are shown in the graphs (see Figure 5), from which it is seen that these deviations are not random, but are the consequence of physical processes in hybrid welding.

The found abrupt lowering of penetrability at certain welding speeds, it attributable to interaction of liquid metal, which under the impact of laser radiation is transported to the rear front of the vapour-gas crater [5] with the liquid metal of the filler wire. Apparently, at some welding speeds, the filler metal fills the crater, formed by laser radiation. Additional power is consumed to oust it from the crater, and, therefore, the penetration depth is reduced. In practice it was impossible to achieve full penetration of the butts of 09G2S steel sheets of thickness $\delta = 10$ mm with a narrow gap (30°) and root face of 6 and 4 mm (Figure 6), unlike the sheets of the thickness, equal to that of the root face (see Figure 4). This may be accounted for by the fact that in square butt welding of sheets, the liquid metal of the filler spreads freely over the surface. In grooved welding the laser radiation stabilizes the arc, thus allowing the liquid metal to penetrate to the very bottom of the groove and fill the spot, where the crater, formed by laser radiation, should be located. Additional laser power is consumed in ousting this metal. In this connection, the penetration depth is reduced, and through penetration is absent.

The considered phenomenon is influenced by a number of factors. It may be assumed that the main of them is the ratio of the frequency of periodic transfer of liquid metal under the impact of laser radiation [5] and frequency of drop transfer in melting of the filler wire by the electric arc [6]. Another argument in favour of this assumption is a periodic falling out of experimental points from the monotonic dependence.

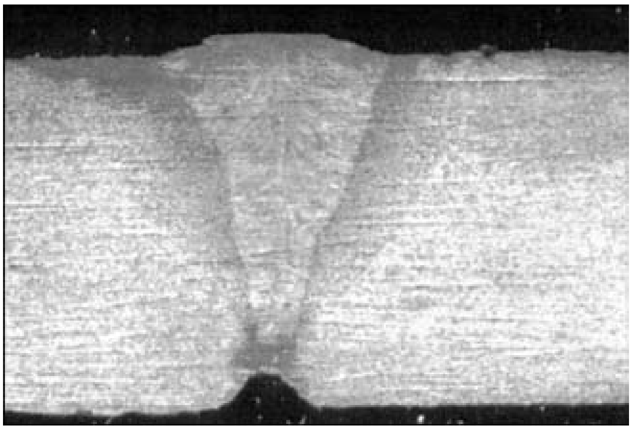

Figure 6. Macrostructure of a butt of 09G2S steel ($\delta = 10$ mm), welded by CO_2 laser-arc process ($P = 2.7$ kW, $\Delta F = -6$ mm, $v_{\mathrm{w}} = 30$ m/h, $v_{\mathrm{f}} = 340$ m/h, $I = 110$ A, $U = 18$ V, shielding gas pressure of 0.05–0.1 MPa)

CONCLUSION

A combined action of laser radiation and the consumable electrode arc in welding steels in CO_2 results in formation of a high-quality upper bead of the weld, this allowing the laser radiation to be decreased, partially replacing it by electric arc power (1 kW of the arc instead of 0.5 kW of laser radiation for $\delta > 5$ mm and one-to-one for $\delta < 4$ mm); the hardness of the produced welds may be reduced, making them more ductile.

Radiation of CO_2-laser stabilizes the electric arc, «ties up» the arc column to the focused beam, coming to the metal, and makes the arc go lower into the vapour-gas channel. The effect of stabilization of the arc is the higher, the greater the power of laser radiation, although at up to 50 m/h speeds just 200–300 W of focused laser radiation is sufficient to stabilize the arc.

In case of hybrid welding at certain values of speed, the penetration depth is drastically decreased, thus disturbing the monotonic nature of dependence $h = f(v_{\mathrm{w}})$. Apparently, this is due to the interaction of the liquid metal, pushed to the crater rear front under the impact of laser radiation, with the liquid metal of the filler wire, molten by the electric arc.

Application of the hybrid process at a fixed power of laser radiation is rational up to a certain thickness, δ, of the metal being welded, above which the penetration depth was not increased, despite lowering of the welding speed.

1. Matsuda, J., Utsumi, A., Katsumura, M. et al. (1988) TIG or MIG arc augmented laser welding of thick mild steel plate. *Joining and Materials*, **1**, 31–34.
2. Khaskin, V.Yu., Shelyagin, V.D., Garashchuk, V.P. et al. (2001) Laser butt welding with high-frequency heating of weld of edges. *The Paton Welding J.*, **11**, 24–27.
3. Garashchuk, V.P., Shelyagin, V.D., Nazarenko, O.K. et al. (1997) Technological CO_2-laser LT-104 of 10 kW power. *Avtomatich. Svarka*, **1**, 36–39.
4. (1974) *Technology of fusion electric arc welding of metals and alloys*. Ed. by B.E. Paton. Moscow: Mashinostroenie.
5. Grigoriants, A.G., Shiganov, I.N. (1988) *Laser technique and technology*. Book 5. Laser welding of metals. Moscow: Vysshaya Shkola.
6. Potapievsky, A.G. (1974) *Shielded-gas consumable-arc welding*. Moscow: Mashinostroenie.

ON WELDING PROPERTIES OF THYRISTOR RECTIFIERS

N.I. POSTOLATY, A.D. GLUSHCHENKO, S.V. DUKH and **L.S. GRITSENKO**
Kakhovka Plant of Electric Welding Equipment, Kakhovka, Ukraine

Features of forming the external static and external dynamic characteristics of thyristorised welding rectifiers are considered and the ability to improve drop transfer in CO_2 welding is shown.

Key words: *CO_2 arc welding, rigid external characteristic of the power source, molten metal transfer, regulator, control law, transfer function*

With the introduction of inverter welding rectifiers the specific weight-dimensional and power characteristics have reached a level, unthinkable of the traditional (diode and thyristor) sources. In addition, increase of transformation frequency enabled active control of molten metal transfer due to practical liquidation of a «unit with pure delay» (minimum one period of pulsations, which for traditional rectifiers is commensurate with the transfer time).

Despite the indubitable advantages of inverter converters, thyristorised and then diode (step-switched) welding power sources still predominate in fitting of the entire equipment fleet for gas-shielded arc welding [1]. Simplicity, cost, reliability, repairability and availability of the welding characteristics, sufficient for a specific technology, will still remain to be the determinant factors in selection of a power source. However, higher requirements, made of the quality of welded joints and equipment efficiency, lead to increased requirements to the welding power sources in fabrication. While no significant breakthrough can be anticipated in terms of the weight-dimensional or power characteristics of the traditional sources, in terms of welding properties there still is some room for improvement.

One of the determinant factors in weld formation is known to be the nature of drop transfer [2, 3], which largely depends on the dynamic properties of the power source. Electrodynamics of thyristor rectifiers is to a certain extent dependent, but is certainly not exhausted by R–L parameters of the transformer and the choke. So far the main focus has been on the choke. The main method for changing its inductance was switching of the number or turns. The control circuit incorporates also the dynamic of controlling the angle of conductivity of the thyristor group. A characteristic feature of the all-purpose power sources (VDU-505, VDU-506, VDU-506S, KIU-301, KIU-501) is an excess of thyristor amplitude voltage for the mode of rigid external characteristics (REC), which results in the rectified voltage oscillogram incorporating ripple, which is much greater than the constant component. Since output voltage signal (U_o) is used as negative feedback (NFB) by the controlled parameter, such a signal has to go through units with the transfer function of the following kind:

$$W(p) = \frac{k}{Tp + 1},$$

where $W(p)$ is the transfer function of the unit; k is the gain factor; T is the time constant of the unit; p is the designation of the operation of differentiation in time.

In the initial control circuit of KIU-501 power source U_o negative feedback loop incorporated two similar units *A1* and *A2* (Figure 1). The schematic in Figure 1 is the design of the simplest proportional voltage regulator (P), typical for all the known thyristorised welding sources. A small I_w current feedback (units *A3, A4*) is used for formation of the required slope of the static external characteristic.

Power source KIU-501 with the control circuit (see Figure 1) was tested in keeping with the require-

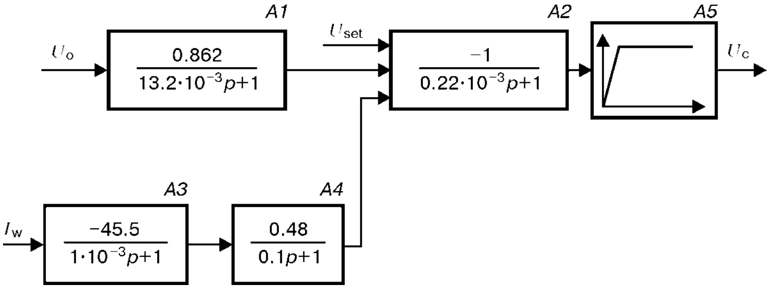

Figure 1. Block diagram (initial) of formation of control voltage U_c by the angle of conductivity of thyristor group: U_o — output voltage of rectifier; U_{set} — setter voltage; I_w — voltage at measuring shunt (welding current signal); *A1* — *RC*-filter; *A2* — summing operating amplifier; *A3* — scaling converter; *A4* — *RC*-filter; *A5* — limiter

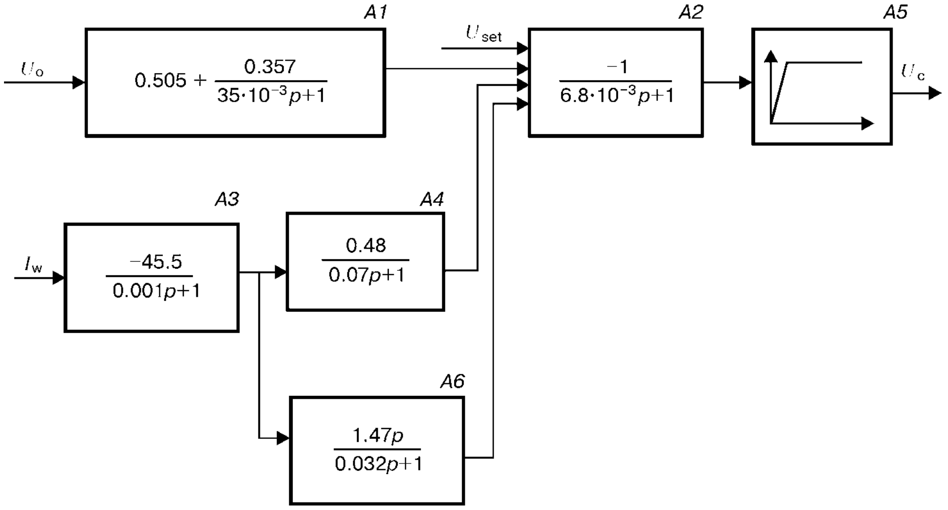

Figure 2. Block-diagram (final) of formation of control voltage by the angle of conductivity of the thyristor group of KIU-501 rectifier in REC mode: *A1* — combined unit with an inertialess proportional and proportional inertia component; *A6* — real differentiating unit

ments of GOST 25616–83 [4] for welding properties and the conclusion was positive. However, testing under the actual conditions of production revealed a number of disadvantages at low currents, namely sluggish arc ignition, unstable arc, higher spatter, unsatisfactory formation of deposited metal, small margin of stability by voltage (small deviations of the setter from the optimal position lead to a marked deterioration of the process, particularly in vertical welding).

Numerous experiments on improvement of the welding properties of the rectifier were limited by selection of the choke parameters and coefficients in the units of the structure in Figure 1. In this case it was assumed (as an axiom) that it is enough to achieve good welding at low currents, to produce an excellent power source in the entire current range. Good welding properties at low currents (70–250 A) were obtained only after, in addition to selection of the regulator time steps, unit *A1* in voltage NFB loop has structurally changed:

$$W(p) = \left(0.505 + \frac{0.375}{35\cdot10^{-3}p + 1}\right).$$

Inertia of unit *A2* was increased by one and a half orders of magnitude ($T_2 = 6.8\cdot10^{-3}$ s), this lowering «fine-drop» fluctuations of U_c and resulting in a «quiet» arc. In this case a considerable portion of NFB signal by the controlled parameter comes in for comparison without dynamic distortions. Such a structure provides high-quality welding process at up to 250 A currents. However, welding in the current range of 250–350 A still remained to be unsatisfactory both in terms of weld formation and spatter, this being attributable to positive current feedback. At currents above 350 A, the process runs in a quite satisfactory manner.

The most cardinal measure on improvement of welding properties is regarded to be limitation of the speed of current rise in the drop [4]. With this purpose it is recommended, in particular, to increase the choke inductiveness up to 1.0–1.4 mH [3]. Experiments with KIU-501 in this respect did not give any significant improvement.

If a welding current derivative d*i*/d*t* (*D*-component) is incorporated into the law of control of the angle of conductivity of the thyristor groups, then the reaction of the real differentiating unit

$$W(p) = \frac{kp}{Tp + 1}$$

on a stepwise action starts immediately.

Practical application of d*i*/d*t* component in the control circuit of KIU-501 rectifier confirmed this possibility (Figure 2). In REC mode the regulator of the angle of conductivity of the thyristor group operates in the linear section of limiter *A5* which, unlike the mode of falling external characteristics (FEC) does not influence the statics and dynamics of the rectifier. After *D*-component has been incorporated into the power source control law, the nature of arcing has drastically changed:

- characteristic crackling, which accompanies the drops breaking up, is absent and soft rustling prevails;
- visually the arc is quiet, sparking is rare, fine and weak;
- process is not sensitive to voltage deviations, greatly exceeding the tolerance ranges to GOST 25616–83;

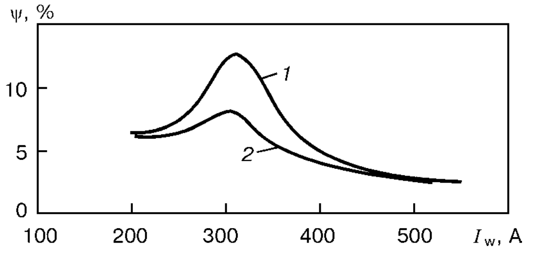

Figure 3. Dependence of metal losses on current in welding with REC (welding wire d = 1.6 mm, CO_2 gas shielding; for designations of curves *1*, *2* see the text)

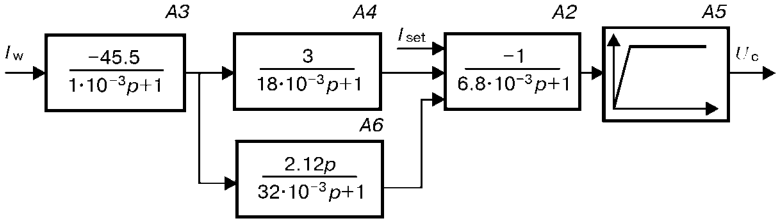

Figure 4. Block diagram of forming of control voltage in FEC mode

- metal deposited in the most unfavourable modes, unlike the previous one, is characterised by fine surface ripple and even edge (absence of undercuts);
- spattering is minimised in the entire range of welding currents.

Metal losses in the most unfavourable modes are reduced (Figure 3). Metal loss in welding, using KIU-50 source with D-component in the control law (curve *2*) is smaller than in welding with the source with the traditional control circuit (curve *1*, [2]).

Block diagram of the KIU-501 control circuit in FEC mode (Figure 4) does not incorporate unit *A1* of voltage NFB, and is characterised by deeper current NFB (unit *A4*). Setter signal I_{set} is the analog of the assigned current.

No noticeable influence of D-component (unit *A6*) on the welding properties of the source in the FEC mode was noted, which is attributable to its relatively weak influence at low current ripple. Influence of unit *A6* was manifested only at static external characteristics at high load currents towards increase of the steepness in the falling section. This is attributable to a pulsed nature of the load and presence of nonlinear loops in the circuit. In case low currents were used, the slope did not change. It is known that a steeply-falling external characteristic in FEC mode promotes stability of the process.

It should be noted that KIU-501 and KIU-301 sources are complete analogs in terms of circuit design. The latter of the above sources differs only by the coefficient of scale transformation ($K_i = -65$) of the welding current signal in unit *A3*. Electronic control boards are unified.

Design of the sources allows applying them in a set with semi-automatic (automatic) machines, incorporating a drive, fed by voltage in the range of 3–36 V, or 24–27 V, or 48 V.

Application of D-component in the power source control law allows obtaining optimal working parameters, providing a good appearance of the weld and process stability.

Power sources with D-component in the control law have been manufactured by Kakhovka Plant of Electric Welding Equipment since January, 2002.

1. Zaruba, I.I., Latansky, V.P., Sidorenko, V.M. (1995) New type of welding rectifier. *Avtomatich. Svarka*, **5**, 53–57.
2. Potapievsky, A.G. (1984) *CO_2 welding*. Leningrad: Mashinostroenie.
3. Voropaj, N.M. (1998) Methods of metal spattering elimination in CO_2 welding. *Svarshchik*, **2**, 7.
4. *GOST 25616–83*. Arc welding power sources. Methods of testing of welding properties.

DEVELOPMENT OF COMPOSITE MATERIALS FOR ZIRCONIUM-BASED ACTIVE ELEMENTS OF PLASMATRON ELECTRODES

A.N. SHAPOVAL
State Engineering Center of Hard Alloys «Svetkermet», Svetlovodsk, Ukraine

An electrode and its manufacturing method are proposed, which envisage formation of a tight contact of the electrode case with the active insert during their joining. A composite material has been developed for the active insert of plasmatron electrode with a barrier layer of zirconium nitride.

Key words: *plasmatrons, electrodes, active elements, cores, zirconium nitride, zirconium, operating life*

Zirconium and hafnium are used in plasma equipment as the active element of thermochemical electrodes. Widening the technological capabilities of plasma processing depends on the operating life of electrodes, exposed to electric and thermal loads [1, 2].

Industrial introduction of the technology of manufacturing composite materials for the active insert of electrodes, developed by us [3, 4], required studying the influence of the electric arc on the structure and composition of the metal of the electrode working zone. With this purpose, in co-operation with V.G. Osintsev and V.M. Romashov in the Institute of Hard Alloys (Russia) and Center «Svetkermet» (Ukraine) [5] we have conducted integrated study of the electrodes, made by the developed technology, with active inserts — core of 2 mm diameter of zirconium alloy 110 (Zr + 1 % Nb); shell of 2.5 mm diameter of zirconium bronze (Br.Zr 0.1).

It is established that the most important index, determining electrode life, is the level of heat and electric conductivity through the contact surface between the core and the shell, which depends on the design and manufacturing technology of the active insert.

Tight metallurgical contact between the core and the shell is provided during deformation of the bimetal insert by the developed technological sequence.

Not less important is provision of a reliable contact between the surfaces of the electrode case and shell of active insert.

In electrode manufacturing the bonding with the case of the active bimetal insert is provided by stamping. We proposed and implemented in industry a method of electrode manufacturing, according to which circular recesses of a parabolic cross-section are formed on the end faces of the holder during active element pressing into the holder.

Figure 1 shows a two-cavity mould, where the casing consists of two parts *7* and *8*, connected by pins *9*. Cavities *10* of the casing accommodate punch *6*, where working end faces *1* are of a parabolic shape, similar to working surface *3* of die *4*. When active insert *2* is pressed into case *5* of the electrode, recesses of a parabolic shape are formed on its surfaces, which allow intensifying the cooling of the case on one side, and on the other (outer) side forming a jet of plasma gas. In addition, a deeper penetration of the plastic deformation zone during stamping improves the tightness of contact of the case and active insert, this improving the thermophysical characteristics of the electrode and extending its life.

An effective technique, extending electrode life, is adding to the electrode design barrier layers between active insert and case.

We developed an electrode, where a layer of zirconium nitride with a pure zirconium bond coat is applied on the core, with the intermediate layer coated by the outer layer of case material. The ratio of the thickness of zirconium nitride layer to core diameter is 0.002–0.010, pure zirconium bond coat has the thickness of 0.5–2.5 μm, while the intermediate layer proper is coated by a layer of case material.

The proposed plasmatron electrode (Figure 2) incorporates active element *1*, located in case *2*, made of a material with a high heat conductivity, for in-

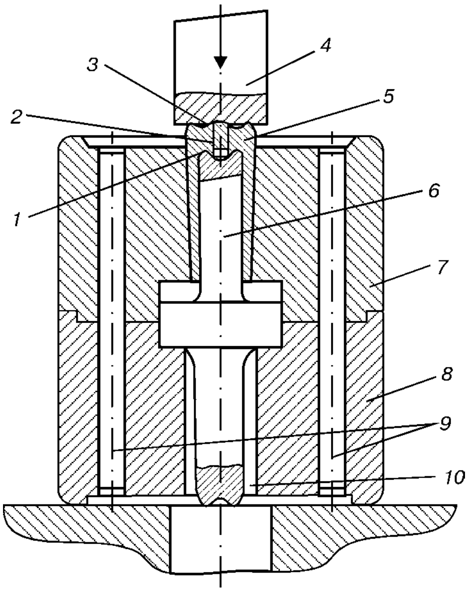

Figure 1. Mould (for designations see the text)

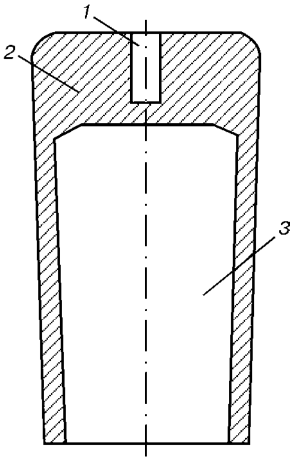

Figure 2. Plasmatron electrode (for designations see the text)

stance, copper, and accommodating cavity *3* for cooling water supply.

Active element (Figure 3) incorporates core *1* of a zirconium alloy, for instance, alloy E110 (Zr — base; 1 wt.% Nb), on which bond coat *2* of pure zirconium, layer *3* of zirconium nitride and outer layer *4* of electrode case material, in this case copper, are applied successively. Active element of the electrode is joined to the case by pressing in.

Use of active element core *1* of a Zr–Nb alloy, manufactured by the developed technology, allowed achieving a high adaptability to fabrication in production of the initial rods and wire, as well as eliminating delamination cracks and discontinuities in the core.

Presence of a thin bond coat *2* of pure zirconium on the surface of a zirconium alloy core promotes a positive gradient (from the centre to the periphery) of thermoemission properties in the active element during arcing, this being positive for its resistance.

Intermediate barrier layer *3* of zirconium nitride prevents diffusion of electrode case material into the active element. This is due to considerable refractoriness of zirconium nitride and its chemical inertness relative to the adjacent components of the electrode.

Outer layer *4* of copper allows improvement of the active element contact with electrode case in pressing in, as it may be applied on the surface of zirconium nitride layer *3* in advance with provision of a tight contact (for instance, by upset forging), and a tight bond between layer *4* and the case is due to chemical affinity of the materials of the case and the layer, as well as their similar physico-mechanical properties.

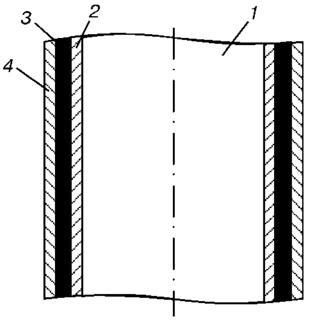

Figure 3. Active element of the electrode (longitudinal section) (for designations see the text)

A feature of the developed electrode design is the fact that the ratio of the thickness of barrier layer of zirconium nitride to core diameter should be 0.002–0.010. At values below 0.002 the absolute thickness of barrier layer on cores of 2–2.5 mm diameter becomes insufficient for performance of barrier functions. Now, if the above ratio is higher than 0.010, case material diffusion into the active element stops, and further increase of the barrier layer thickness is not rational.

Bond coat *2* of pure zirconium has the thickness of 0.5–2.5 μm. During electrode testing, it was found that decrease of the layer thickness below 0.5 μm and its increase above 2.5 μm does not have any significant influence on electrode performance.

Thickness of outer layer *4* of electrode case material is not limited. Plasmatron electrode is manufactured as follows. A material with a high heat conductivity, for instance, copper, is used to produce by turning the case with the drive opening for the active element, which is manufactured by successive physical deposition on the core-substrate (zirconium alloy wire) of the layers of pure zirconium, zirconium nitride and copper.

Zirconium nitride may be deposited by any of the known processes at substrate temperatures below the recrystallization temperature (below 860 °C) of the active element material (zirconium serves as the active material), one of which is the ion-plasma process of vacuum condensation of substances by ion bombardment (CIB), which allows deposition of both pure zirconium and zirconium nitride successively in one cycle.

Practical deposition of a zirconium bond coat and a zirconium nitride layer is performed by CIB process in VU-16 unit. Cores of zirconium alloy E110 of 2 mm diameter and 6 mm height were placed in one layer in the loading device and the unit was pumped down. When a vacuum of 0.4 Pa was achieved, substrate current was set at 2–2.5 A and the voltage at 900–1100 V, plasma-forming arc was struck and a zirconium ion flow was used to clean the surface of the cores with simultaneous deposition of a bond coat of pure zirconium. When the substrate current is decreased below 2 A and the voltage below 900 V, zirconium is not deposited as a solid film. At increase of substrate current above 2.5 A and of voltage above 1100 V, core heating temperature was higher than 860 °C, which is inadmissible, because of the alloy recrystallization.

After preheating of the cores, coated with a layer of pure zirconium, up to 500–600 °C, nitrogen is bled into the chamber and reference voltage of 90–110 V is set at unchanged current of the substrate of 2–2.5 A. Zirconium nitride layer is deposited under these conditions. At substrate current below 2 A and reference voltage below 90 V the cooling process is abruptly slowed down and is not of a stable nature. With increase of current above 2.5 A and of voltage above

110 V macroparticles of pure zirconium appear in zirconium nitride layer, this disturbing the continuity and uniformity of zirconium nitride layer, and being detrimental to its barrier properties.

Investigations of the service durability of the electrodes of the developed design have been conducted, compared to electrodes of the known design. Service durability criterion was taken to be electrode life, namely limit number of arc ignitions with preservation of intactness of the electrode working tip.

Results of tests, conducted in PVR-402UKhL4 unit in plasma cutting of 6 mm steel (cutting current of 400 A, voltage of 180 V, cutting speed of 0.12 m/s, cut length of 16.2 m), are given in the Table. During testing it was found that the life of the developed electrodes is much longer than that indicated in work [2].

As shown by metallographic and X-ray diffraction analysis of the zone of erosion crater, longer electrode life is largely due to barrier properties of zirconium nitride (copper content in the crater was reduced 3–4 times, compared to known electrodes). On the other hand, this design of plasmatron electrode is characterised by a high tightness of contact between the core and the above layer, thus intensifying the heat removal and lowering the transient resistance.

An outer layer of copper on the active element provides tighter contact of the active element and the electrode case, and, hence, a longer life of electrodes.

Increase of electrode life, achieved by adding a barrier layer, allows full use of the capabilities of plasma-arc equipment, developed at the E.O. Paton Electric Welding Institute [1].

CONCLUSIONS

1. Experimental studies of electric erosion and life of electrodes with bimetal active inserts, produced by the developed technology, demonstrated a direct connection between the tightness of metallurgical contact of components and technological characteristic — their life.

2. Plasmatron electrode design and its manufacturing method were developed, proceeding from these studies.

3. It is established that the presence of a refractory barrier layer between the active core and case of plasmatron electrode improves electrode life due to limitation of diffusion of the case material into the core. A composite has been developed for the active element of plasmatron electrode, consisting of a refractory core (Zr and Hf–Zr alloy), produced by the developed technological sequence, the surface of which is successively coated with layers of pure zirconium, zirconium nitride (barrier layer) and case material (copper or zirconium bronze).

4. Performed research confirms the broad technological capabilities of the developed technology of composite manufacturing, in terms of producing high-quality electrodes for plasma-arc equipment.

Life studies of an electrode with a composite barrier layer

Active element			*Electrode life (arc ignition)*
Bond coat thickness, μm	*Interlayer*		
	Thickness, μm	δ	
2.5	2	0.0010	52
2.5	4	0.0020	55
2.5	15	0.0075	63
2.5	20	0.0100	56
2.5	30	0.0150	53
3.5	15	0.0075	60
1.5	15	0.0075	60
0.5	15	0.0075	57
0.2	15	0.0075	55
2.5	15	0.0075	54

Note: 1. Core of active element is made of alloy E110 of 2 mm diameter, its bond coat is of zirconium, intermediate layer — of zirconium nitride, outer layer — of copper 10 μm thick, electrode case — of copper. 2. Here δ denotes the ratio of the thickness of a zirconium nitride layer to core diameter.

1. Esibyan, E.M. (1971) *Plasma-arc equipment*. Kyiv: Tekhnika.
2. Amosov, V.M., Karelin, B.A., Kubyshkin, V.V. (1976) *Electrode materials based on refractory metals*. Moscow: Metallurgiya.
3. Shapoval, A.N. (1999) Production and properties of zirconium composites as an active material for plasma cutting electrodes. In: *Int. Transact. on Advanced Technologies and Systems of Mechanical Engineering*, Issue 7. Donetsk: DonGTU.
4. Shapoval, A.N., Poznansky, V.I., Khokhlov, Yu.G. (1995) Development of technology of manufacturing electrodes for plasma cutting of metals. In: *Proc. of Int. Conf. on Advanced Equipment and Technologies used in Mechanical Engineering*, Donetsk, Ukraine, Sept. 1995. Donetsk: DonGTU.
5. Shapoval, A.N. (1998) State Engineering Center of Hard Alloys «Svetkermet». *Instrument. Svit*, **3**, 28–29.

PECULIARITIES OF DEOXIDATION OF THE WELD POOL METAL IN PLASMA SURFACING WITH COMPOSITE MATERIALS

A.I. BELY, A.P. ZHUDRA and **V.I. DZYKOVICH**
The E.O. Paton Electric Welding Institute, NASU, Kyiv, Ukraine

Experiments on deoxidation of matrix of granular tungsten carbide based composite alloys in plasma surfacing, transfer of aluminium to the deposited metal and its effect on arrangement of reinforcing particles ($WC-W_2C$) in the wear-resistant layer are described.

Key words: *plasma surfacing, filler material, composite alloy matrix, reinforcing particles, deoxidation*

Plasma surfacing with composite alloys [1] operating under conditions of intensive abrasive wear involves the problem of porosity of the deposited layer. Core of a flux-cored strip consists of grains of a hard alloy based on fused tungsten carbides.

This is attributable primarily to the use of a cold-rolled strip of steels 08kp (rimmed) and 08ps (semi-killed), containing 0.03–0.055 % oxygen, as a filler material sheath. It is likely that the increased oxygen content may cause formation of pores in the deposited metal. During surfacing the reinforcing particles (eutectic alloy of tungsten mono- and semi-carbides $WC-W_2C$) are subjected to incomplete dissolution, which leads to saturation of the molten pool with tungsten and carbon. This creates conditions for formation of a large amount of CO in the melt, whereas comparatively high rates of solidification of the alloy prevent its precipitation [2]. Hence, the matrix of the alloy has a high porosity in the bulk of the deposited metal, which causes a substantial decrease in strength of fixation of the reinforcing grains in it and deterioration of performance of the composition as a whole.

To eliminate porosity, the imperative technological operation is the addition of deoxidising elements with a higher affinity for oxygen than iron into the filler material. Basic deoxidisers in gas surfacing with tungsten carbide based composite alloys [3], flux-cored wire arc welding and surfacing [4, 5] and solid wire gas-shielded welding and surfacing [6] are silicon and manganese, which also have a positive effect on formation of the deposited metal. However, the addition of silicon in an amount of 0.2–1.5 % and manganese in an amount of 0.4–2.5 % into the filler material for plasma surfacing with composite alloys failed to provide positive results. So, this stipulated the search for more efficient deoxidisers.

It is well-known that aluminium (having a higher affinity for oxygen), being present in the welds at the molten pool temperature close to the solidification beginning point, increases their ductility. In compounds with nitrogen, aluminium forms nitrides to decrease stability of iron carbide and reduce diffusion

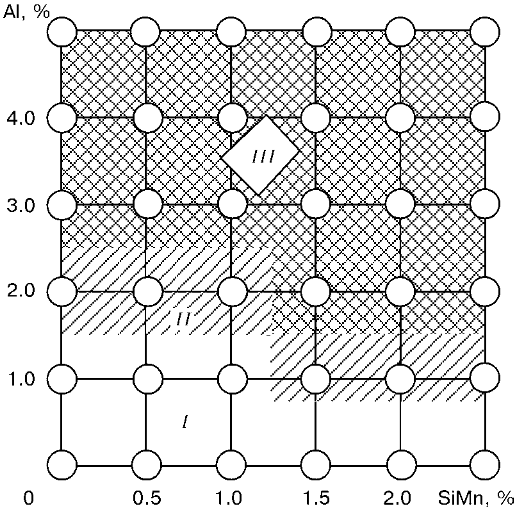

Figure 1. Optimal percentage of aluminium and silicomanganese in the deposited metal for removal of porosity of the composite alloy: *I* — pores; *II* — individual pores; *III* — no pores

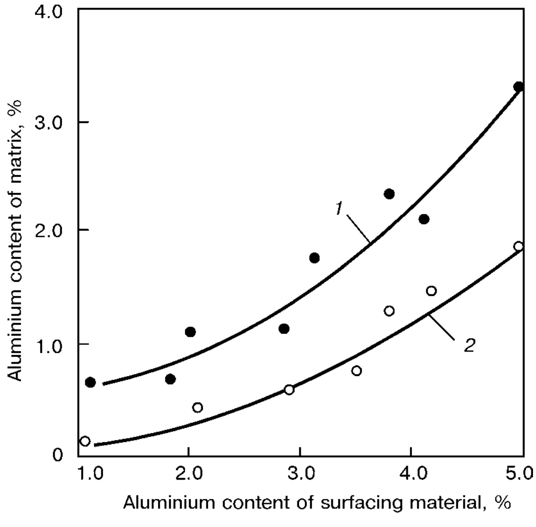

Figure 2. Dependence of the aluminium content of the alloy matrix upon its content of the surfacing material: *1* — aluminium added in the form of all-drawn wire; *2* — aluminium added in the form of powder

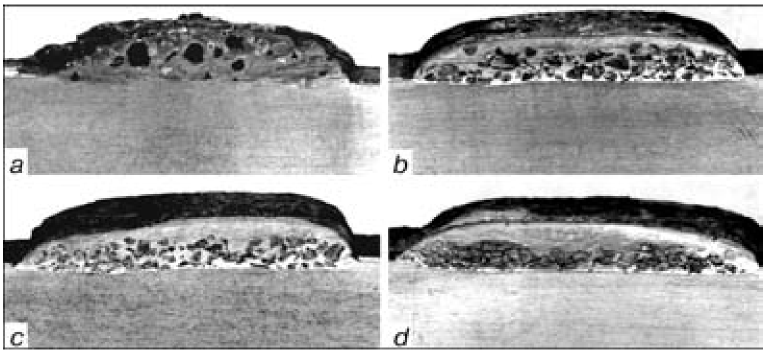

Figure 3. Macrostructure of samples deposited with a tungsten carbide strip with a differing aluminium content (%) of the filler material: *a* — without aluminium; *b* — 1.5–2.0; *c* — 2.5–3.5; *d* — 4.0–5.0

of carbon, thus having a positive effect on formation of the composite alloy matrix [7]. Therefore, a complex deoxidation system comprising silicon, manganese and aluminium was developed to eliminate porosity. The optimal percentage of these elements was found experimentally. Silicon and manganese were added to the core of the filler material in the form of silicomanganese SMn-17, which received wide acceptance as a deoxidising and alloying additive used in production of different-application steels [8]. Its content was varied from 0.5 to 2.5 % by 0.5 %. Aluminium was added into the core of the filler material in the form of an aluminium powder of the PA-3 grade or an all-drawn aluminium wire, and its content was varied from 0.5 to 5.0 % by 1.0 %. Granular tungsten carbide with particles 0.63 to 1.10 mm in size was used as the wear-resistant component, and its content of the material was 60–65 %.

Surfacing was performed on samples of low-carbon steel using the plasma surfacing machine with an electrically neutral system for feeding the filler material to the plasma arc zone. In this case the direction of the filler material feed coincided with the direction of surfacing. The surfacing parameters are given in the Table.

The range of optimal percentage of aluminium and silicomanganese in the surfacing material to eliminate porosity of the composite alloy (Figure 1) was found as a result of the experiments conducted. Silicomanganese exerts an active effect at its content of the filler material equal to 1.4–1.8 %. The aluminium powder content in this case should range from 2.5 to 3.5 % (region *III*). With silicomanganese and aluminium added in amounts less than 1.4 and 1.7 %, respectively, the deposited layer is damaged with pores (region *I*).

The addition of aluminium in the form of the all-drawn wire allows its content of the filler material to be decreased by 30–40 % due to an increased coefficient of its transfer to the composite alloy matrix (Figure 2). In this case approximately 50 % of the deoxidising element is consumed for combining oxygen to form oxides precipitating on the bead surface.

The presence of aluminium in the filler material was found to have a considerable effect on the surfacing process. The metal transfer is of a spray character. The constant contact between the filler material and the molten pool is provided, and formation of the wear-resistant layer is improved. Alloying the matrix melt with aluminium also has an effect on arrangement of the reinforcing particles in the bulk of the deposited layer. The addition of aluminium in the form of the all-drawn wire in an amount of 2.0–2.2 % leads to a marked decrease in the concentration of the hard alloy grains in the upper volumes of the deposited metal, and no such grains are present on the surface of the wear-resistant layer. They are uniformly distributed over the entire volume (Figure 3). With the aluminium content increased up to 5.0 %, the upper layers of the deposited metal become almost absolutely free from the reinforcing particles.

This phenomenon is attributable to the fact that the presence of aluminium in the molten pool leads to decrease in its solidification rate, reduces viscosity of the matrix melt and facilitates immersion of the hard alloy grains.

This effect is especially important for hardening of external surfaces of drill pipe joints operating in casing strings. The reinforcing particles do not participate in the process of fitting the deposited joint to the casing pipe and do not wear it, which allows performance of the drill pipe joints to be substantially improved.

Comparative tests of an experimental batch of the drill pipe joints showed that the rate of wear of the external surfaces of the joints deposited with a material containing silicomanganese and aluminium was 1.2–1.5 times lower than that of the joints hardened

Parameters of surfacing experimental samples

Parameter	*Numerical values*
Surfacing current, A	210–220
Arc voltage, V	36–38
Surfacing speed, m/h	6.8–7.0
Filler material feed speed, m/h	25–26
Plasma torch oscillation amplitude, mm	20
Oscillation frequency, min^{-1}	34
Nozzle exit section to part distance, mm	14–17
Plasma gas flow rate, l/min	3–4
Shielding gas flow rate, l/min	6–8

with a non-oxidised composite alloy, and that their service life was extended by 30–35 %.

1. Bely, A.I. *The process of plasma surfacing using composite alloys*. Author's cert. 1622097, Int. Cl. B 23 K 9/04. Publ. 23.01.91.
2. Vojtovich, R.F., Pugach, E.A. (1975) High-temperature oxidation of carbides of group IV-VI metals. In: *High-temperature carbides*. Kyiv: Naukova Dumka.
3. Zhudra, A.P. (1980) *Study and development of materials designed for surfacing with composite abrasive wear-resistant alloys*. Syn. of Thesis for Cand. of Techn. Sci. Degree. Kyiv.
4. Pokhodnya, I.K., Suptel, A.M., Shlepakov, V.N. (1972) *Flux-cored wire welding*. Kyiv: Naukova Dumka.
5. Yuzvenko, Yu.A., Kirilyuk, G.A. (1973) *Flux-cored wire surfacing*. Kyiv: Naukova Dumka.
6. Potapievsky, A.G. (1974) *Shielded-gas metal-arc welding*. Moscow: Mashinostroenie.
7. Bagryansky, K.V., Dobrotina, Z.A., Khrenov, K.K. (1976) *Theory of welding processes*. Kyiv: Vyshcha Shkola.
8. Gasik, L.N., Ignatiev, V.S., Gasik, M.I. (1975) *Structure and quality of commercial ferroalloys and master alloys*. Kyiv: Tekhnika.

SURFACING WITH NITROGEN ALLOYS

V.N. KALIANOV
Ukrainian Engineering-Pedagogical Academy, Kharkiv, Ukraine

Examples of effective alloying of deposited metal with nitrogen are considered. It is shown experimentally that nitrogen assimilation by deposited metal in arc welding (surfacing) at straight polarity current is higher than that at reverse polarity.

Key words: *surfacing, nitrogen, alloying, resources-saving materials*

The N-containing steels both with equilibrium and also superequilibrium content of nitrogen at a proper alloying have high characteristics of strength, wear and corrosion resistance [1–3].

Results of investigations of properties of alloys 50Kh25N4AG9M4B, 10Kh32N8AM2, 140Kh15N2AT and others [3–5] confirmed the expediency of auxiliary alloying of a wear-resistant layer with nitrogen (0.2–0.4 %).

In bath-slag surfacing using flux ANF-6 (wt.%: 25–31Al_2O_3; up to 8CaO; up to 2.5SiO_2; CaF_2 — balance) the sulphur content in the deposited layer of alloy 50Kh25N4AG9M4B (wt.%: 0.5C; 25.0Cr; 4.0Ni; 9.0Mn; 4.0Mo; up to 1.0Nb; 0.2N) was decreased from 0.018 to 0.008 %, and the content of rest elements remained similar to that of a rod electrode. Structure of the deposited metal was fine-grained, with uniformly distributed dispersed carbides and nitrides. Ultimate strength was increased approximately by 10 %, the impact strength was more than twice increased. Directionality of crystallites, high values of heat resistance, favourable for increase in wear-resistance, promote the increase in life of parts deposited and cast using electroslag process.

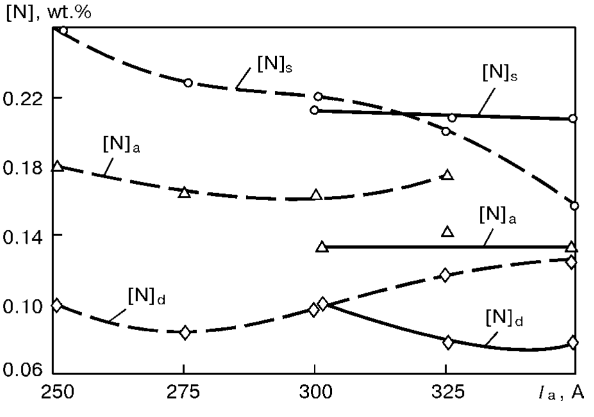

Figure 1. Dependence of nitrogen saturation of drops and metal of a single-layer bead on polarity of current in surfacing (U_a = = 28 V, v_s = 30m/h, nitrogen consumption ≈ 20 l/min, wire Sv-04Kh18N19 of 2 mm diameter) (*dashed curve* — at straight polarity, *solid curve* — at reverse polarity)

The ultimate strength, durability, hardness and impact strength of the deposited metal 45Kh14N14V2M (wt.%: 0.45C; 14.0Cr; 14.0Ni; up to 2.0W; up to 1.0Mo) are much lower than similar values of alloy 50Kh25N4AG9M4B containing 0.39–0.42 wt.% N.

The arc surfacing with solid and flux-cored wires was performed under flux or in nitrogen. The nitrogen

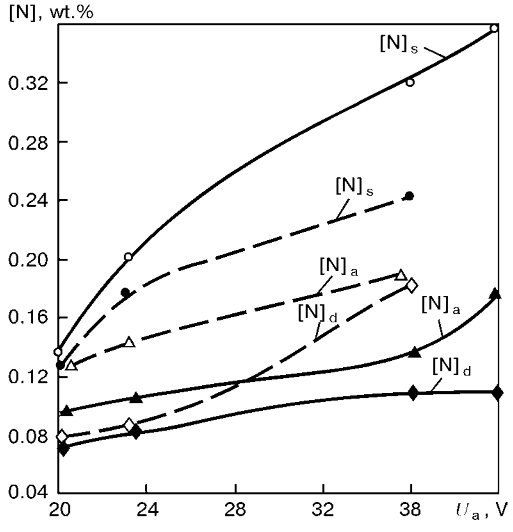

Figure 2. Effect of arc voltage on nitrogen alloying of drops and deposited metal at $I_a \cong 250$ A (rest parameters and conditions of surfacing see in Figure 1)

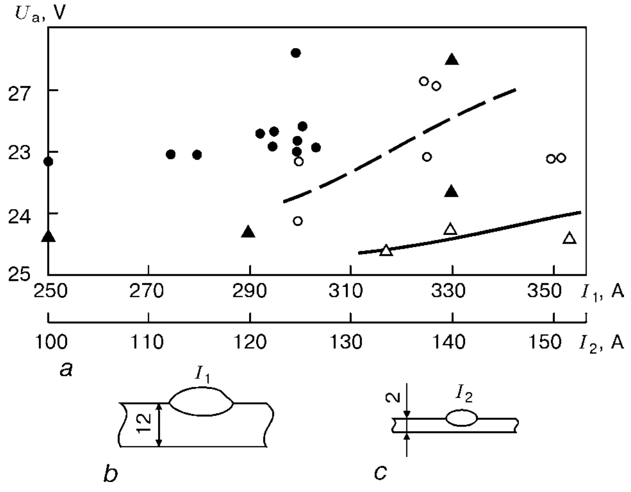

Figure 3. Area of technologically-acceptable values of arc voltage and current (*a*) in surfacing with austenitic steels at DCRP (*b, c*) and consumption of shielding gas $Q_N \cong 20$ l/min, obtained in X-ray unit at transmission condition $U = 110$ kV, $I = 10$ mA, $t = 20$ s: *a* — surfacing of steel 10Kh17AG14 ([N] = 0.39 %, at high current I_1 with $d_{wire} = 2$ mm, $v_s = 20$–30 m/h); *b* — surfacing of steel 20Kh13N4G9 at low current I_2 with $d_{wire} = 1$ mm, $v_s = 40$–50 m/h (●, ▲ — pores; ○, Δ — no pores)

application as a protecting-alloying medium ensures the reduction in a share of participation μ in a parent metal to the values at which the metal of the first layer is close by composition to the surfacing wires. With increase in current from 200 to 350 A at reverse and straight polarity the values of μ are changed, respectively, in the ranges 0.30–0.51 and 0.14–0.19 (at $U_a = 24$–25 V, $v_s = 30$ m/h, $d_{wire} = 1.6$ mm, $l_{stickout} = 25$–26 mm).

Alloying of metal with nitrogen at the stages of drop formation $[N]_d$ after passing through the arc $[N]_a$ and in a single-layer bead $[N]_s$ depends on the condition parameters, current polarity, composition of wires (and parent metal for $[N]_s$). During surfacing at reverse polarity the content of $[N]_d$, and in particular $[N]_a$, is lower as compared with use of current at straight polarity (Figures 1 and 2).

As to the quality the dependence of $[N]_s$ on condition parameters is almost the same in surfacing with austenitic wires, both with solid and flux-cored wires. The dense austenitic deposited metal was produced at content [N] = 0.20–0.27 wt.% (Figure 3). With increase in mass share of $[N]_s$ its hardness and strength is increased (in particular in replacement of Cr–Ni and Cr–Ni–V wires by Cr–Ni–Mn wire). Here, the mass share of a high-temperature ferrite is decreased (Figure 4). In martensitic-bainitic alloys the alloying with nitrogen influences the mechanical properties, reduces the residual stresses [6] due to decrease in temperature interval of the martensitic transformation.

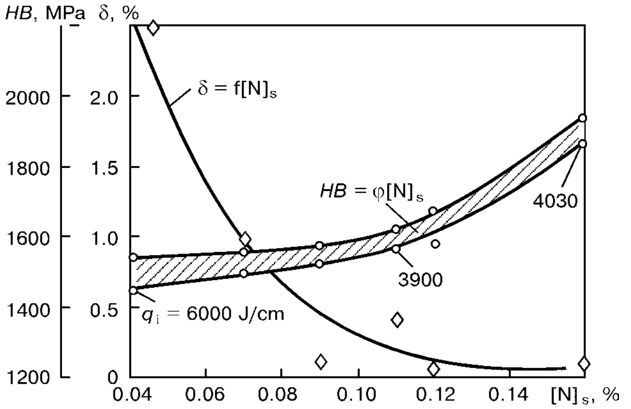

Figure 4. Effect of mass share of nitrogen in deposited metal on hardness of bead metal *HB* and content of δ-phase in it (content of elements in deposited metal, wt.%: $[C]_s = 0.080$–0.009; $[Cr]_s = 17.0$–17.9; $[Ni]_s = 10.13$–10.21; $[Ti]_s = 0.49$–0.56; $[Mn]_s = 1.04$–1.14; $[Si]_s = 0.90$–0.98 (q_i — energy input of surfacing)

The improvement of formation of deposited beads at straight polarity current (especially in wide-layer surfacing) can be attained using a multielectrode surfacing, and also a combination of a cyclic switching of direct arc to indirect arc.

Adding of active nitride-forming components into a charge of flux-cored wires and use of no-current filler wires increase the mass share of nitrogen, and also the mass share of nitrides as a strengthening phase, increase the coefficients of assimilation of alloying elements [7] and, as a whole, the volume of use of high-nitrogen steels of different structural classes (including maraging steels) [1, 2], as sparsely-alloyed surfacing alloys.

1. Paton, B.E., Medovar, B.I., Saenko, V.Ya. (1992) Modern processes of production of high-nitrogen steels and alloys and prospects of application of pressure arc-slag remelting for its production. *Problemy Spets. Elektrometallurgii*, **2**, 5–13.
2. Saenko, V.Ya., Pomarin, Yu.M., Chernets, A.V. (1998) 5th Int. HNS'98 Conf. on High-Nitrogen Steels. *Ibid.*, **3**, 76–82.
3. Grinberg, N.A., Mamaev, A.V. (1983) Surfacing filler materials with carbide and carbide-nitride strengthening of deposited metal. In: *Surfacing of wear-resistant and high-temperature steels and alloys. Surfacing filler materials.* Kyiv: PWI.
4. Kalianov, V.N., Peschansky, I.P. (1980) Mechanical properties of austenitic valve steels produced by electroslag remelting. *Dvigatelestroenie*, **8**, 43–44.
5. Krasavchikov, V.A., Soloviova, L.I. (1984) Influence of nickel and nitrogen on structure, processibility and mechanical properties of high-chromium deposited metal. *Metallovedenie i Termich. Obrab. Metallov*, **10**, 21–23.
6. Zubkov, N.S. (1972) *Research and development of technology for surfacing in nitrogen medium of Fe–Cr-based steels*. Syn. of Thesis for Cand. of Techn. Sci. Degree. Sverdlovsk.
7. Bagrov, V.A., Kalianov, V.N. (1999) Arc surfacing with Fe–C–Cr–Mn–Ti–Si system alloys using auxiliary filler. *Avtomatich. Svarka*, **5**, 62–63.